Development of Jones Matrix Tomography for Functional Ophthalmic Imaging

by

Myeong Jin Ju

M.Sc., GIST (Gwangju Institute of Science and Technology) 2011

A THESIS SUBMITTED IN PARTIAL FULFILLMENT OF

THE REQUIREMENTS FOR THE DEGREE OF

Doctor of Philosophy

in

THE FACULTY OF GRADUATE AND POSTDOCTORAL STUDIES

(Electrical and Computer Engineering)

The University of British Columbia

(Vancouver)

August 2015

Abstract

Optical coherence tomography (OCT) provides the axial profile of back-scattered light from biological tissues and enables non-invasive, three-dimensional structure imaging. Since the introduction of OCT technique, OCT has shown its powerful utility especially in the field of ophthalmology. However its capability is still limited to the structural investigation. Because many eye diseases are tightly associated with tissue functions such as blood circulation and tissue microstructure, development of functional OCT is important. Since the necessity of functional extension of OCT technique got more attention, Doppler OCT and polarization-sensitive OCT (PS-OCT) have been developed for blood flow and birefringence measurements, respectively, and have been widely utilized for ophthalmic imaging for clinical and pathological research purposes. Jones-matrix-based OCT, also named as Jones matrix tomography (JMT), was originally designed as one type of PS-OCTs capable of measuring the polarization properties of biological tissue. In this dissertation, an advance version of JMT system is developed and also novel applications of JMT in ophthalmology is introduced.

New JMT algorithms are developed, which make JMT system being capable of multi-contrast imaging including scattering, localized flow, and polarization contrasts. Novel spectral shift compensation and adaptive averaging methods are

devised for achieving sensitivity-enhanced scattering OCT and polarization property measurements. Especially, by stabilizing the phase of the system, Doppler flow measurement is achieved with a high sensitivity.

As a new clinical application, JMT is utilized for three-dimensional volumetric *in vivo* imaging of human eyelid. With the degree of polarization uniformity contrast (DOPU), one of the polarization contrasts produced by JMT, meibomian glands (MGs) are exclusively segmented from OCT volumetric image. With MG segmentation, its age-dependent morphological characteristics are further investigated.

As another clinical application, JMT is also utilized for investigating corneal collagen cross-linking (CXL) effect on cornea stroma. Fresh bovine corneas are treated by two different CXL protocols (standard and accelerated CXL) and measured *ex vivo*. Morphological changes on the cornea after the two different protocols are cross-examined to evaluate their treatment outcomes in terms of the cross-linking effectiveness and progression.

Through this study, JMT is shown to have great potential to monitor and diagnose many different ocular diseases non-invasively.

Preface

Chapter 3. A version of these materials have been published in the following papers:

- ***M. J. Ju***, Y.-J. Hong, S. Makita, Y. Lim, K. Kurokawa, L. Duan, M. Miura, S. Tang, and Y. Yasuno, "Advanced multi-contrast Jones matrix optical coherence tomography for Doppler and polarization sensitive imaging," Opt. Express **21**, 19412-19436 (2013).

- ***M. J. Ju***, Y.-Joo. Hong, Y. Lim, L. Duan, S. Makita, S. Tang, M. Miura, and Y. Yasuno, "Multi-functional optical coherence tomography for polarization and Doppler investigation of posterior eye," SPIE proc. (Photonics west 2013) 8571-14 (2013).

- ***M. J. Ju***, Y. -J. Hong, S. Makita, M. Masahiro, S. Tang, and Y. Yasuno, "Simultaneous birefringence and flow imaging with Multifunctional Jones matrix optical coherence tomography," Association for Research in Vision and Ophthalmology (ARVO) 1611656 (2013).

I was the lead investigator, responsible for all major areas of concept formation, data collection and analysis, as well as manuscript composition. Y. Lim and Y.-J. Hong were involved in the early stage of system implementation and contributed to data collection and analysis. M. Miura arranged patient experiment and provided

the patient's medical history. Y. Yasuno was the supervisory author on this project and was involved throughout the project in concept formation and manuscript composition.

A version of Chapter 4 has been published in the following papers:

- ***M. J. Ju***, J. G. Shin, S. Hoshi, Y. Yasuno, B. H. Lee, S. Tang, and T. J. Eom, "Three-dimensional volumetric human meibomian gland investigation using polarization-sensitive optical coherence tomography," J. Biomed. Opt. **19**, 030503 (2014).

- ***M. J. Ju***, J. G. Shin, D. K. Kasaragod, S. Hoshi, B. H. Lee, S. Tang, T. J. Eom, and Y. Yasuno, "Volumetric Meibomian glands visualization using Office-based Multifunctional optical coherence tomography," European Conferences on Biomedical Optics (ECBO) 1648552 (2013).

I was the lead investigator, responsible for all major areas of concept formation, data collection and analysis, as well as manuscript composition. S. Hoshi arranged patient experiments and provided the patients' medical history. T. J. Eom was the supervisory author on this project and was involved throughout the project in concept formation and manuscript composition.

The project located in Chapter 5 was conducted in the Biophotonics Laboratory at the University of British Columbia (Vancouver campus), and has been reported in the following papers:

- ***M. J. Ju***, and S. Tang, Usage of polarization-sensitive optical coherence tomography for investigation of collagen cross-linking," J. Biomed. Opt. **20**, 046001 (2015).

- ***M. J. Ju***, and S. Tang, "Investigation of corneal collagen cross-linking using polarization-sensitive optical coherence tomography," SPIE proc. (Photonics west 2015) 9307-18 (2015).

I was the lead investigator, responsible for all major areas of concept formation, data collection and analysis, as well as manuscript composition. S. Tang was the supervisory author on this project and was involved throughout the project in concept formation and manuscript composition.

The works described in Chapter 3 and Chapter 4 were conducted under supervision of S. Tang, Y. Yasuno and T. J. Eom at the University of Tsukuba in Japan. All protocols for the measurement in Chapter 3 and Chapter 4 were approved by the Institution Review Board of University of Tsukuba. The work shown in Chapter 5, was performed under supervision of S. Tang at the University of British Columbia in Canada.

Table of Contents

List of Tables

List of Figures

List of Abbreviations

A-line Axial line of an image.

ACXL Accelerated collagen cross-linking.

AMD Age-related macular degeneration.

ANSI American national standard institute.

AOM Acousto-optic modulator.

AS-OCT Anterior segment optical coherence tomography.

BPD Balanced photo-detector.

BS Non-polarizing beam splitter.

CCD Charge-coupled device.

CH choroid.

CLSM Confocal laser scanning microscopy.

CXL Collagen cross-linking.

DOPU Degree of polarization uniformity.

ELM External limiting membrane.

EOM Electro-optic modulator.

FA Fluorescence angiography.

FAF Fundus auto-fluorescence.

FPN Fixed-pattern noise.

FWHM Full width at half maximum.

GA Geographic atrophy.

GCL ganglion cell layer.

ICGA Indocyanine green angiography.

INL inner nuclear layer.

IPL internal plexiform layer.

IS/OS inner and outer segments of the photoreceptor.

ISO International organization for standardization.

JMT Jones matrix tomography.

LC Lamina cribrosa.

MEMS Microelectromechanical systems.

MG Meibomian gland.

MGD Meibomian gland dysfunction.

NIR Near-infrared.

OCA Optical coherence angiography.

OCE Optical coherence elastography.

OCT Optical coherence tomography.

ODT Optical Doppler tomography.

ONH Optic nerve head.

ONL Outer nuclear layer.

OPL outer plexiform layer.

OPLD Optical path length difference.

PBS Polarization beam splitter.

PD Polarization diversity.

PS-OCT Polarization-sensitive optical coherence tomography.

PT posterior tip of the outer segment.

QWP Quarter wavelength plate.

RNFL retinal nerve fibers layer.

RPE retinal pigment epithelium.

SD Standard deviation.

SD-OCT Spectral-domain optical coherence tomography.

SHG second harmonic generation.

SNR Signal to noise ratio.

SS-OCT Swept-source based optical coherence tomography.

TPEF Two-photon excitation fluorescence.

UV-A Ultraviolet-A : (315 nm – 400 nm wavelength).

Acknowledgements

Four years has passed since I joined Biophotonics group as a graduate student in the University of British Columbia. I would like to thank all of the lab members and ex-members for their help. Especially, Leo Pan, Tom Lai, and Mengzhe Shen help me a lot to get used to living in Vancouver and studying in UBC.

I would like to express my gratitude to Prof. Shuo Tang for guding me to focus on the research. She always trusts me, and at the same time encourages me to learn how to do my own research and become independent. Without her kindness, instruction, and support, I was not able to continue my research. I finally understood that I am lucky to have such a grateful mentor.

I am grateful to Prof. Yoshiaki Yasuno, who is an outstanding engineer, researcher, and leader of Computational Optics Group (COG) in the University of Tsukuba. He gave me a chance to work in his group as visiting scholar for 10 months. During the time, I had learned much more about polarization-sensitive optical coherence tomography and Doppler angiography systems. I also would like to thank every COG members. Dr. Shuichi Makita, Dr. Kazuhiro Kurokawa, and Dr. Youngjoo Hong gave me enormously helpful and practical advices. Without their instructions, it would be very difficult to finalize my research project.

I would like to thank all the committee members and external reviewer, Prof.

Calum MacAulay, Prof. Alireza Nojeh, Prof. Jeff Young and Prof. Jennifer Kehlet Barton (University of Arizona). Thanks to their helpful advices and suggestions, I could successfully finalize my dissertation.

I would like to thank anonymous reviewers and excellent researcher somewhere in the world for having a discussion, question, suggestion, and encouragement. They pointed out very accurately and suggested me a lot of valuable experiments.

I thank my parent and parent-in-low. They encouraged me to go to graduate school, and they gave me emotional support and financial assistance. I also give a special feeling of gratitude to my farther, Il-Chang Ju whose word encourages me to keep pursuing my path as a researcher.

I also dedicate this dissertation to my friends, Myung-Hoo Park and Jung-Mi Kim who have supported our family and helped me to focus on my work. I will always appreciate all they have done to me and my family.

Finally, I would like to give a special thanks to my lovely and beautiful wife, Hyo-Jin Hwang who has never left my side and are very special means to me more than anything in the world.

Myeong Jin Ju

The University of British Columbia

(Vancouver)

August 2015

Dedicated to Lord, Jesus Christ.

Chapter 1

Introduction

1.1 Optical coherence tomography

Optical coherence tomography (OCT) is an interferometric imaging modality that provides tomography of human tissues non-invasively and *in vivo* [1]. OCT is a scanning low-coherence interferometer utilizing coherence gating to resolve the depth structure of a sample.

Figure 1.1 shows a typical OCT system schematic. A low coherence light source is directed to a Michelson interferometer and is then split into reference and sample beams. In the reference arm, the light exiting from the reference port of a beam splitter in the interferometer is reflected from a reference mirror, and redirected into the beam splitter. In the sample arm, the light exiting from the sample port of the beam splitter is focused on the sample after a lateral scanning device and an objective lens. The light backscattered from the sample, $E_{samp}(t)$, is redirected to the beam splitter and combined with the returning reference light, $E_{ref}(t)$, in the beam splitter. The electric field at the output of the interferometer

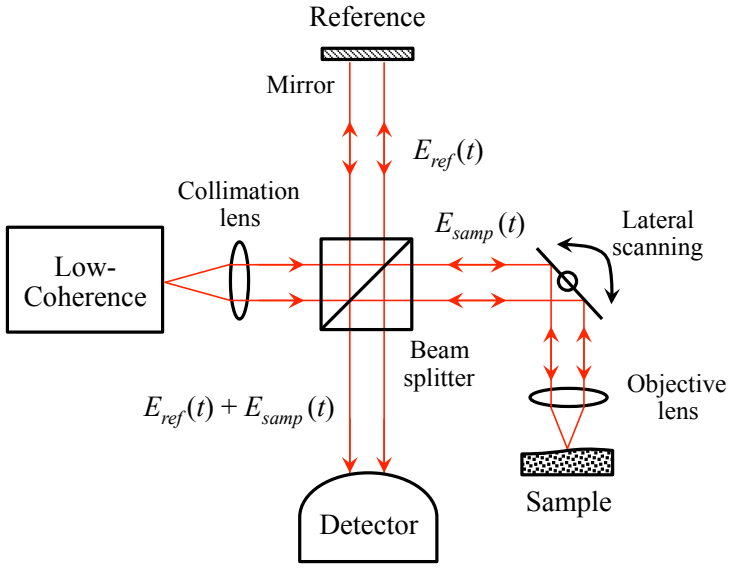

Figure 1.1: Schematic of a typical Michelson interferometer based OCT system.

is the sum of the sample and reference electric fields, $E_{ref}(t) + E_{samp}(t)$ that is detected by a detector. The detector measures the intensity of of the output, which is proportional to the square of the output electric field:

$$I_{out}(t) \propto |E_{ref}(t)|^2 + |E_{samp}(t)|^2 + 2E_{ref}(t)\, E_{samp}(t) \cos(2k\Delta L), \qquad (1.1)$$

where k is a wavenumber and ΔL is the path length difference between the sample and reference arms of the interferometer. In Eq. 1.1, the factor of 2 in the cosine term accounts for the round-trip path length of the sample beam. The electric signals from the detector are then processed into A-scan (or A-line) representing the depth-resolved reflectivity profile of the sample around the focal spot [1].

The depth-resolved cross-sectional structure images are generated by scanning the probe beam transversely and performing multiple axial measurement of echo time delay (axial scans), as shown in Fig. 1.2. In the case of one-dimensional transverse scanning (X), a two-dimensional cross-section image (XZ), which rep-

resents the optical backscattering in a cross-sectional plane through the tissue, is obtained. Three-dimensional, volumetric data sets can be generated by acquiring sequential cross-sectional images by scanning the incident optical beam in a raster pattern (XY).

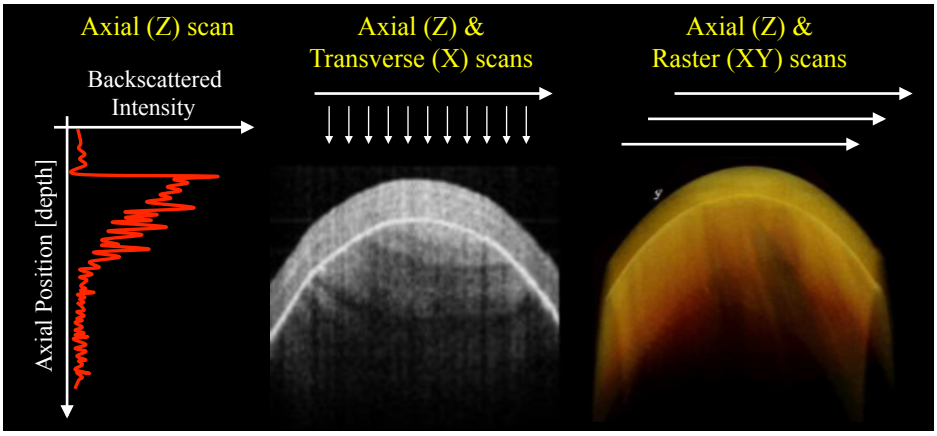

Figure 1.2: OCT signal and image formation process. OCT provides cross-sectional and three-dimensional volumetric images by detecting the backscattered magnitude corresponding echo time delay of light. Axial scans measure the backscattering versus depth. Cross-sectional images are generated by performing a series of axial scans at different transverse positions. Three-dimensional volume image can be acquired from sequential cross-sectional images by raster scanning.

Among different medical tomography modalities, OCT is characterized by the following properties. First, OCT is non-invasive since OCT uses a low power near-infrared (NIR) light as a probe which keeps the sample remaining free of photochemical and photothermal damage. Second, OCT has higher resolution (a micrometer resolution of around 2 to 15 μm) than other clinical tomographic methods such as X-ray computed tomography, magnetic resonance imaging, and ultrasound tomography [2]. Third, the measurement speed of OCT is fast. The first generation of OCT, known as time-domain OCT (TD-OCT), had an imaging speed between several hundreds to several thousands of A-lines per second [2]. A more recent

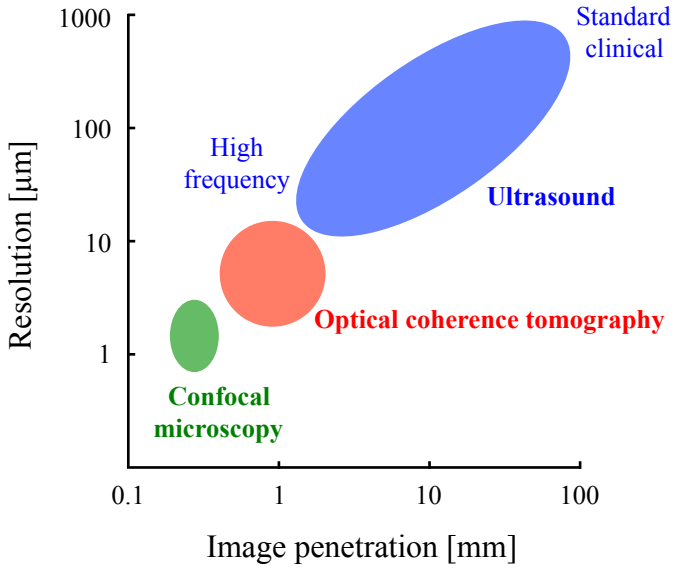

Figure 1.3: Comparison of resolution and imaging depth for OCT and other tomographic modalities.

OCT method, Fourier-domain OCT (FD-OCT) provides an even faster speed of around several hundred-thousand A-lines per second [3, 4]. This high speed enables 3-D investigation of organs *in vivo* within a realistic measurement time. Another characteristic property of OCT is its measurement depth or penetration depth. As mentioned, OCT uses light as probe beam which is relatively highly scattered by the sample to be measured compared to ultrasound and X-ray. This high scattering unfortunately limits the penetration depth of OCT to within a few millimeters. As shown in Fig. 1.3, OCT fills a gap between ultrasound and microscopy in terms of imaging resolution and depth. The resolution of clinical ultrasound imaging is around 0.1 – 1 mm. Since sound waves at the standard wave frequencies (3 – 40 MHz) has relatively low absorption in biological tissue, it is possible to image deep in the body. Although high resolution of 15 – 20 μm has been achieved with high ultrasound frequencies ($\sim$ 100 MHz), these high frequencies have strong attenuation

in the biological tissue so that imaging depths are limited to only a few millimeters. Confocal microscopy, one of the optical microscopic imaging techniques, has extremely high resolution of 1 μm. However, its imaging depth range is limited to a few hundred micrometers. Considering all of these OCT properties, it is clear that OCT is not an all-purpose tomography modality. However, there are some organs that are extremely suitable for OCT such as the eye.

1.2 OCT & ophthalmology

OCT has been utilized in a variety of clinical fields such as ophthalmology [5–10], dermatology [11–18], dentistry [19–22], gastroenterology [23–27], and cardiology [28–33]. Among these clinical fields, ophthalmology is especially suited to OCT. The eye itself is an optical instrument and perfect organ for investigation by optical modalities. Because the eye is an imaging system that images an object onto the retina, it is also convenient to build an optical system that images the retina onto an arbitrary imaging plane using the eye optics.

Another important characteristic of the eye is transparency. As shown in Fig. 1.3, OCT penetration is limited to a few millimeters, mainly because of scattering in tissue. However, the scattering within the optical media of the eye including the cornea, aqueous humor (that fills the anterior eye chamber), crystalline lens, and vitreous is negligible. Hence, several-millimeter penetration of retinal OCT imaging is defined not from the surface of the eye but from the surface of the retina, located around 24 mm under the eye surface. Because the thickness of the retina is about a few hundred micrometers, the limited penetration of OCT is not a serious issue for retinal imaging.

The direction of the tomographic cross-sectional imaging also enhances the

value of OCT. While most other eye imaging modalities such as ophthalmoscope, color fundus photography, and angiographies are *en face* imaging modalities, OCT is the only one that is an *in vivo* modality that provides a depth-oriented cross-sectional imaging of the retina. Because the retina has a fine multi-layered structure and its destruction is highly associated with eye diseases, the *in vivo* cross-sectional tomography provided by OCT is extremely important for ophthalmic diagnosis. Figure 1.4 depicts cross-sectional and volumetric retina OCT images in the fovea region of a healthy human eye as an example.

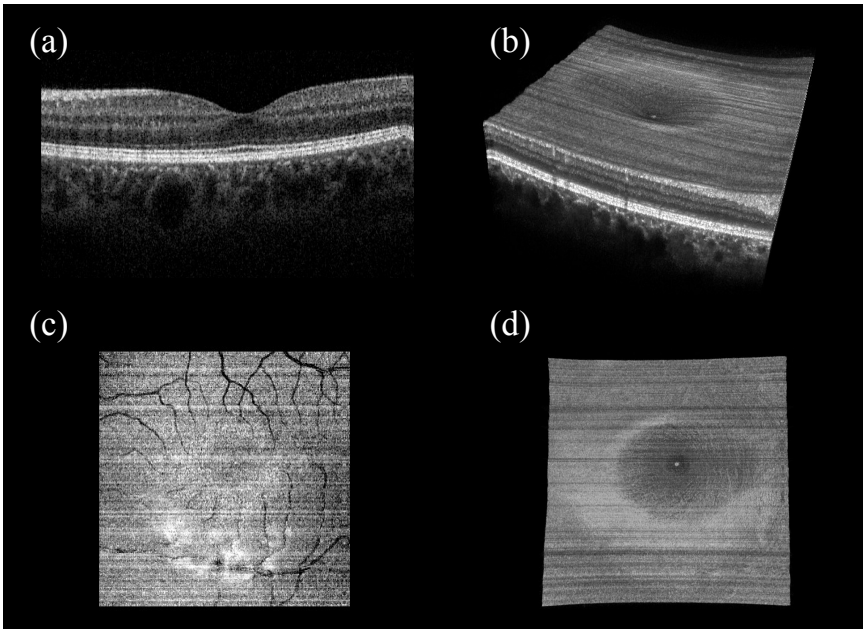

Figure 1.4: *In vivo* retina OCT imaging in the fovea region of healthy human eye with OCT: (a) Cross-sectional tomography image; (b) 3D rendering of the volumetric image; (c) *En face* projection image; (d) OCT fundus tomogram near the center of fovea.

The non-invasiveness of OCT is also particularly important in ophthalmology. This is because the eye is one of a few organs that we cannot biopsy. Since all portions of the retina are associated with visual function, it is impossible to excise

even a small portion of its tissue for diagnosis purposes. Considering these properties of the eye and OCT, it is natural to conclude that the eye is a perfect organ for investigation by OCT. It is also natural that the eye was selected as the first target for OCT.

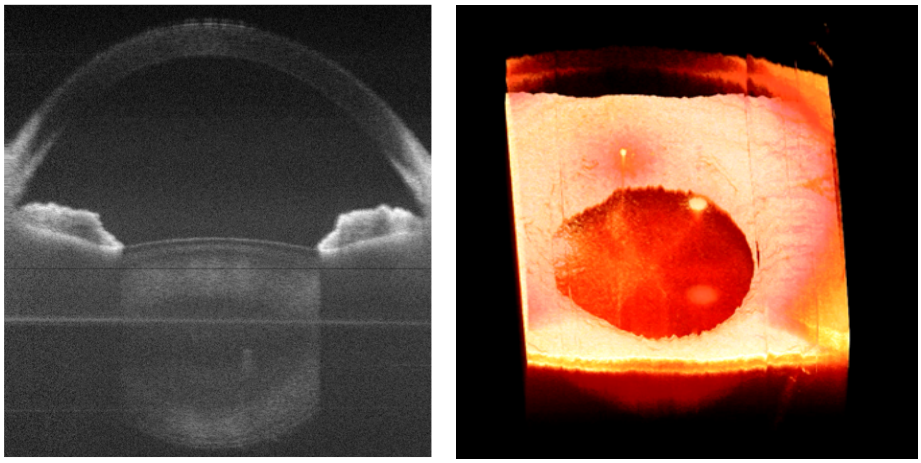

(a) (b)

Figure 1.5: *In vivo* anterior segment OCT image. (a) Cross-sectional tomography image; (b) 3D rendering of the volume image.

It should be noted that the application of OCT in ophthalmology is not limited to retina. OCT can also be used to image the anterior segment that is the front of the eyeball. Figure 1.5 shows an example of the anterior chamber OCT image from which the anterior angle and detailed cross-sectional corneal structure are observed.

1.3 Developments of OCT technology

Measurement speed of OCT is particularly important for *in vivo* eye imaging because of the involuntary eye motion. Therefore, the OCT measurement speed needs to

be fast enough to make eye motion negligible. Another important requirement for ophthalmic OCT is high sensitivity. Because the reflectivity of retina can be as low as 10^{-5} – 10^{-6}, a high system sensitivity and the corresponding high signal-to-noise ratio (SNR) are required. In general, the SNR of OCT is roughly proportional to the measurement time and optical power of the probe beam. Since the OCT measurement time should be short for avoiding the eye motion, it is not an option to increase measurement time for enhancing the SNR. Increasing the probe power is also not a practical solution. Because the eye is a photosensitive organ, it is also very sensitive to photodamage. Even though OCT uses NIR light as the probe beam, the probe beam power for ophthalmic imaging is strictly limited by safety standards such as ANSI [34] and ISO [35]. For example, the maximum allowable probe power for retinal OCT is around 700 μW for a probe wavelength of 840 nm and around 1.2 – 1.7 mW for 1060 nm probe wavelength.

The first generation of OCT, TD-OCT (Fig. 1.6(a)), is a relatively slow imaging modality. In TD-OCT, the optical path-length in reference arm is translated longitudinally in time for depth scanning. Because of the property of low coherence interferometry, interference is only occurred when the path-length difference between the reference and sample arms lies within the coherence length of the light source. Here, the coherence length equivalent to the theoretical axial resolution of OCT is described by

$$l_c = \frac{2\ln(2)}{\pi}\frac{\lambda_c^2}{\Delta\lambda}, \tag{1.2}$$

where λ_c and $\Delta\lambda$ are the center wavelength and wavelength bandwidth of the light source, respectively. As shown in Fig. 1.6(d), the envelope of the modulation caused by the interference changes as the path length difference is varied, in which the peak position of the envelope corresponds to the path-length matching. In practice, the

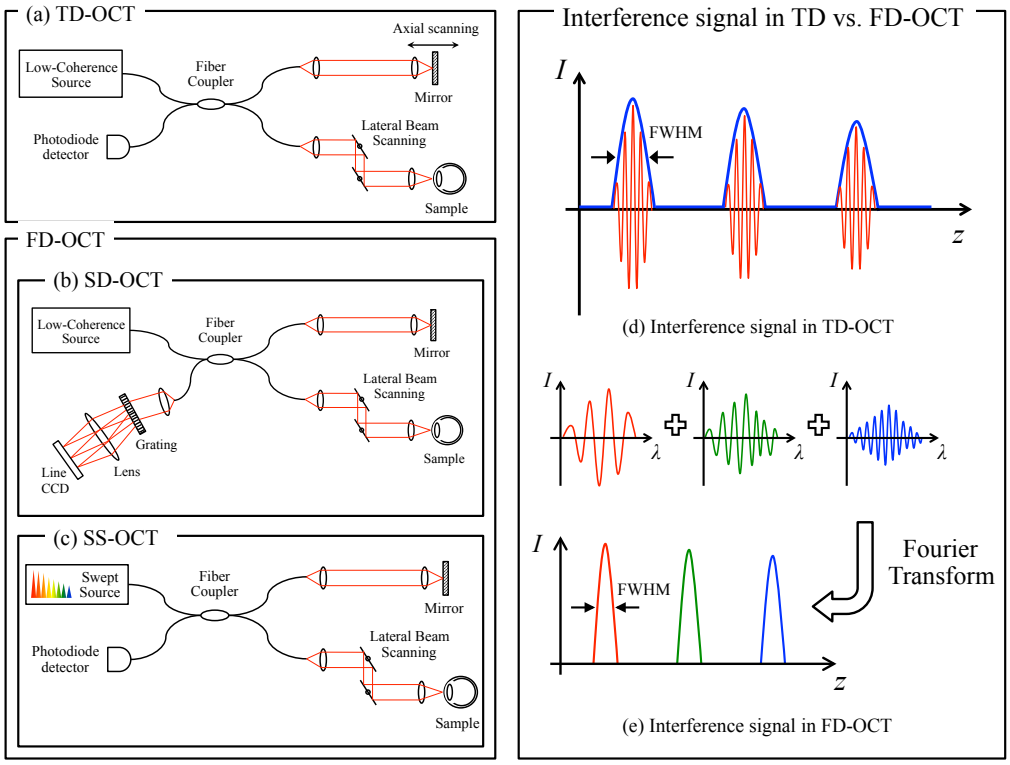

Figure 1.6: Time- and Fourier domain OCT systems and interference signals. (a) TD-OCT; (b) SD-OCT; (c) SS-OCT; (d)–(e) interference signals in TD-OCT and FD-OCT, respectively.

axial resolution of TD-OCT system is defined as the full width at half maximum (FWHM) of the envelope. In the case of TD-OCT, two scannings are required for a single cross-sectional imaging, and a third scanning is necessary for constructing volumetric tomography. This multi-dimensional mechanical scanning limits the measurement speed, and causes poor sensitivity as well.

These limitations have driven researchers to develop a new OCT technology named as FD-OCT. There are two representative FD-OCT techniques: spectral-domain OCT (SD-OCT; Fig. 1.6(b)) and swept-source based OCT (SS-OCT; Fig. 1.6(c)). In SD-OCT, the interference fringe is spectrally decomposed by a diffraction grating and then detected by a charge-coupled device (CCD) array. In SS-OCT, by

means of a wavelength-swept laser source, interference fringe is mapped to the time corresponding to each scanned wavelength and is measured with a photodetector as a function of time. In both SD-OCT and SS-OCT, each data point of the spectral fringe corresponds to a spatial frequency component of the depth profile of the sample. Therefore, the axial profile of an image (A-line) is obtained by performing a discrete Fourier transform of the acquired spectral encoded interference fringe. Similar to TD-OCT, the axial resolution of FD-OCT is also given by measuring the FWHM of the interference peak after the Fourier transform (shown in Fig. 1.6(e)).

FD-OCT first attracted the attention because of its fast measurement speed. Soon it was recognized that it also had a higher sensitivity than TD-OCT [36–38]. This higher sensitivity can be seen as a result of the higher throughput of the probe beam to the image formation. In TD-OCT, the reference and probe beams generate an interference signal only when the optical path length difference (OPLD) is less than the coherence length. Although this is the origin of the depth resolution of TD-OCT, it also means that the probe beam that is outside of the coherence length cannot contribute to image formation. On the other hand, FD-OCT is considered to be a bundle of monochromatic interferometers. As an example, in the case of SD-OCT, the signal output at each wavelength channel of the spectrometer provides monochromatic interference between the reference and probe beams. Hence, the beams generate an interference signal even when the OPLD is several millimeters long. The broadband interference, i.e., low-coherence interference, which provides the depth resolution, is then numerically performed later in a computer. Because of this interference scheme, almost all portions of the probe beam power contribute to image formation.

Because of these two major advantages of FD-OCT, i.e., high speed and high

sensitivity, it has quickly become the standard for tomographic investigation of the eye. Especially, SS-OCT at 1 μm wavelength becomes a common option for posterior eye investigation these days because of the lower absorption of melanin [39], long imaging depth (due to the short instantaneous line-width) [3], and high imaging speed [4, 40, 41].

1.4 Functional extensions of OCT

One of the greatest challenges for extending clinical applications of OCT is to find more contrast mechanisms for providing physiological information beyond the morphological structure obtained by general OCT. Therefore, several functional OCTs have been developed, including Doppler OCT and polarization-sensitive OCT.

1.4.1 Doppler OCT

Doppler OCT which is also denoted as optical Doppler tomography (ODT) is one of the extensions of OCT, and is actively applied for the ophthalmic investigation [42–45]. Doppler OCT has been mainly utilized in blood flow measurement [46, 47]. Doppler OCT combines the Doppler principle with OCT to measure the Doppler shift of probe beam of OCT and to enable depth-resolved cross-sectional flow imaging of eye *in vivo*.

In general, Doppler frequency shift ($\Delta f_{Doppler}$) of a moving scatter is described as

$$\Delta f_{Doppler} = 2v_{axial}/\lambda_c, \tag{1.3}$$

where v_{axial} is the axial velocity of the moving scatters parallel to the direction of the incident light with a center wavelength of λ_c. In order to obtain the Doppler

frequency shift using OCT, several scans of complex OCT signals are obtained at the same region of interest, and the phase-differences among the complex OCT signals are calculated. Since the complex OCT signals are recorded separately at fixed time intervals Δt, the axial velocity of moving scatters for each coherent volume is now described as

$$v_{axial,i} = \frac{\lambda_c}{4n\pi T}\Delta\phi_i, \tag{1.4}$$

where $\Delta\phi_i$ is given by $\Delta\phi_i(z, \Delta t) = \text{Arg}\left[\Gamma_i(z,t)\Gamma^*_{i+1}(z, t+\Delta t)\right]$. Here, $\Gamma_i(z,t)$ is the i-th complex OCT signal given time of t and at a depth of z. The sensitivity of the Doppler flow measurment is mainly limited by the time interval Δt, Doppler angle, and phase noise. Here, the time interval can be altered by modifying the scanning protocols [48–51] or implementing dual-beam scan techniques [52, 53].

Among several variations of Doppler OCT, phase-resolved Fourier domain Doppler OCT [42, 43] has become the most popular Doppler OCT technique because of the recent success of FD-OCT. In terms of the vasculature mapping, OCT-based angiography named as optical coherence angiography (OCA) [54] has been developed as an alternative to the standard ophthalmic angiography such as fluorescein angiography (FA) and indocyanine green angiography (ICGA), and utilized for visualizing retinal and choroidal vasculatures as shown in Fig. 1.7.

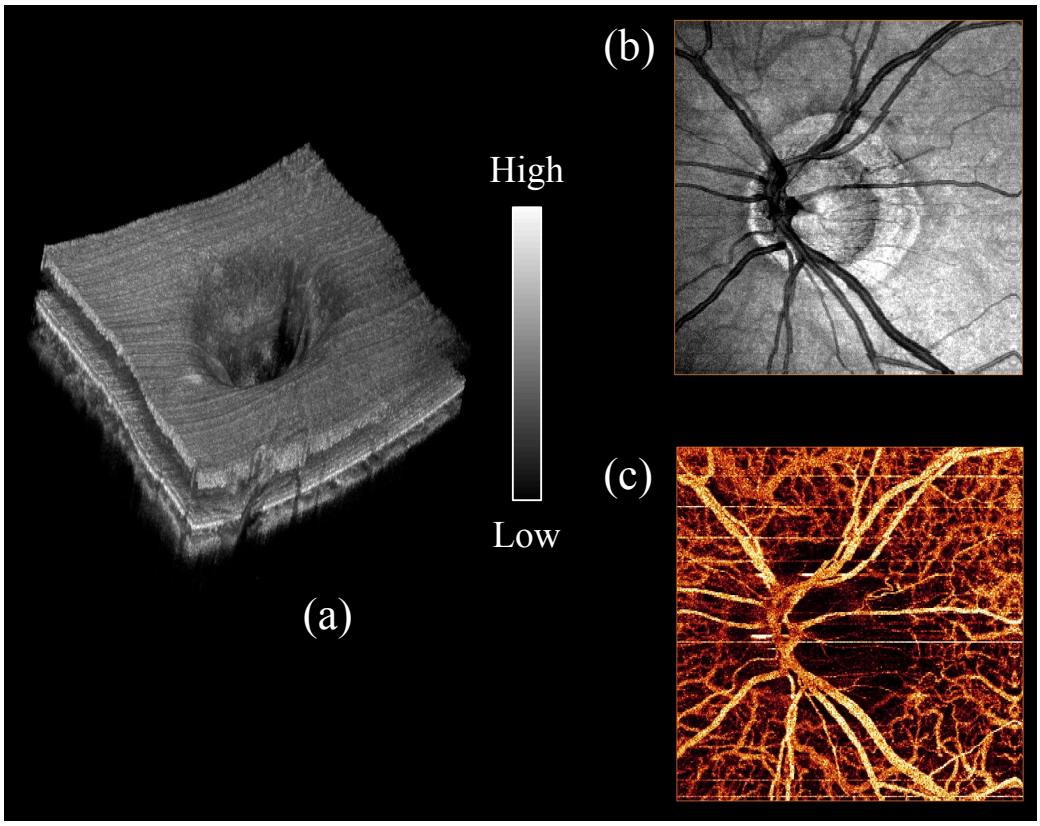

Figure 1.7: 3D volume OCT and OCA images of human optic nerve head (ONH). (a) 3D volume-rendered OCT image; (b) *En face* projection of OCT image of human ONH; (c) *En face* projection of retinal and choroidal vasculature.

1.4.2 Polarization-sensitive OCT

Polarization-sensitive OCT (PS-OCT) is another representative extension of the OCT techniques. PS-OCT is capable of measuring the polarization properties of biological tissues and visualizing their properties with different contrast mechanisms as shown in Fig. 1.8. It is known that several types of biological tissues possess microscopic fibrous structures such as collagen fibers and nerve fibers. Since these microscopic structures are smaller than the resolution of OCT, standard OCT is not capable of assessing them. However, the microscopic structures are known to possess birefringence, and PS-OCT is capable of assessing these microscopic tissue properties by measuring its polarization property. PS-OCT has been also applied to several clinical investigations in ophthalmology such as corneal integrity [55, 56], retinal disorders including macular diseases [57–59], glaucoma surgery [60], quantification of the retinal nerve fiber layer [61,62,64–68] and choroidal thickness [69,70], contrast enhancement of fibrous tissue [58, 60, 71–73] and retinal pigment epithelium (RPE) [57, 74].

PS-OCT systems are classified into several sub-types. One of the most widely utilized methods is the circular-polarization-based method (also known as Hee-Hitzenberger method), which was first demonstrated by Hee *et al.* [75] and later investigated by Hizenberger and his associates [55, 57, 72]. The Hee-Hitzenberger method determines the phase-retardation and the optics-axis orientation of a sample by using a circularly polarized probe beam. Since this method uses only the intensity of OCT and does not use its phase to determine the phase-retardation, this method is robust and stable. On the other hand, since the probe beam should be circularly polarized, the interferometer should be implemented by bulk optics or built with a polarization maintaining fiber. Another property of this method is its

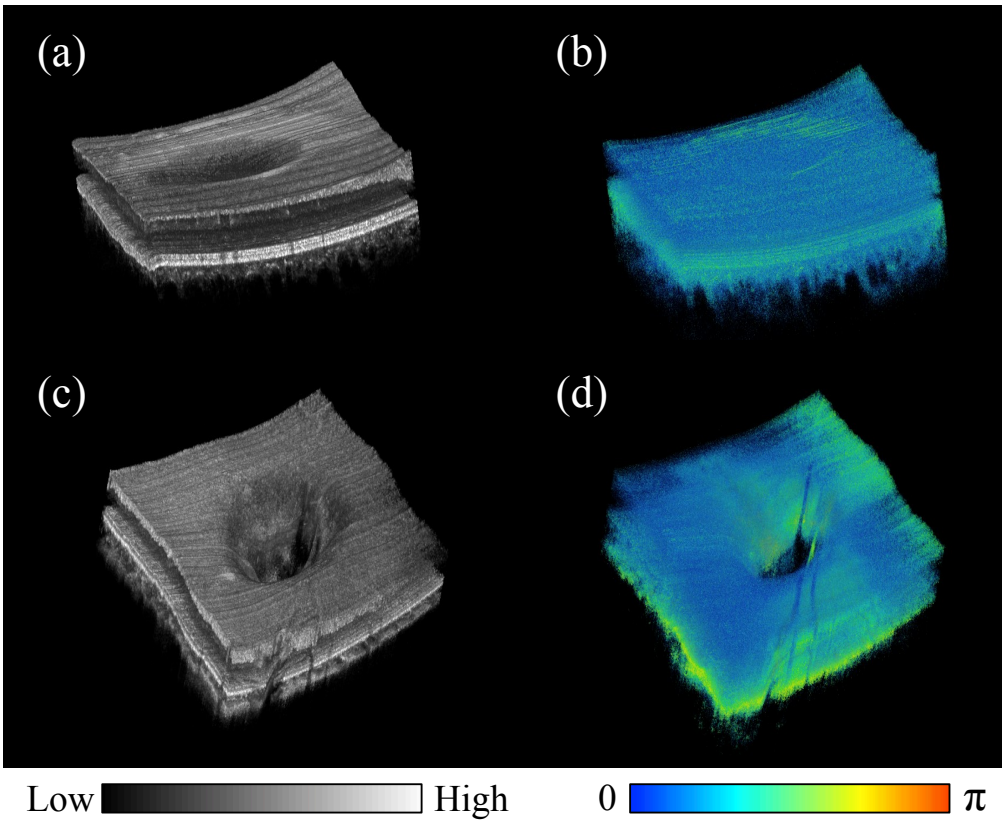

Figure 1.8: Volumetric PS-OCT imaging in the human retina. (a) 3D rendering of the volumetric OCT image of human macular; (b) Volumetric phase retardation image corresponding to (a); (c) 3D rendering of the volumetric OCT image of human optic nerve head; (b) Volumetric phase retardation image corresponding to (c).

insensitivity to diattenuation. Here, diattenuation is the property of a material in which the transmittance depends on the incident polarization states of light.

Stokes parameter-based PS-OCT has also been widely investigated [76]. This method is capable of determining the phase-retardation and optic-axis orientation of a sample. As with the Hee-Hitzenberger method, the Stokes method is also not capable of measuring the diattenuation of the sample. One of the advantages of this method is its ability to be implemented with single-mode fiber, which is widely utilized for OCT [68, 77, 78]. The optic-axis orientation measured by this method is an absolute orientation if the system is implemented with a bulk interferometer or a relative axis orientation if it is implemented with a flexible single-mode fiber. One drawback of this method is its requirement for an active optical device that alters the polarization state of the probe beam, typically an electro-optic modulator.

Mueller matrix-based PS-OCT has been also demonstrated [79, 80]. This method determines the Mueller matrix of a sample, and hence it provides all of the polarization properties of the sample including the phase retardation, axis orientation, and the diattenuation except depolarization. The depolarization cannot be measured because of a fundamental limitation of a coherent imaging modality such as OCT [81]. Mueller matrix PS-OCT uses only the intensity of OCT signal, and hence it could be robust in principle. However this method requires relatively large numbers of measurements, so that the measurement time is relatively long. This long measurement time would deteriorate the accuracy of the polarization properties in an *in vivo* measurement.

Among the several sub-types of PS-OCT, Jones-matrix-based OCT, or Jones matrix tomography (JMT) in short, is a method that determines the polarization properties of a sample by measuring the double-pass Jones matrix of the sample

or its similar matrix [82–85]. This method can be implemented both with a bulk interferometer or a single-mode-fiber based interferometer. With the bulk interferometer, this method can provide a round-trip Jones matrix of the sample, directly. On the other hand, with the single-mode fiber interferometer, a similar matrix of the round-trip Jones matrix of the sample is obtained. From the round-trip Jones matrix or its similar matrix, the phase retardation, the diattenuation, and the relative optic-axis orientation could be obtained.

Table 1.1 shows the summary of different PS-OCT configurations and their characteristics.

Table 1.1: Summary of various PS-OCT system designs

Type	**Incident polarization**	**Measurement protocol**	**Required signals**	**Polarization contrasts**
Hee-Hitzenberger	Single circular polarization	Single measurement	Intensity	Retardation Orientation
Stokes parameter	Single circular polarization	Single measurement	Intensity + Phase	Retardation Orientation
Mueller matrix	Two or more linear polarizations	Multiple measurements	Intensity	Retardation Orientation Diattenuation
Jones matrix	Two linear polarizations	Single measurement	Intensity + Phase	Retardation Orientation Diattenuation

Note: The systems requiring circular polarization incident should be implemented based on either bulk optic or polarization maintaining fiber optic components.

1.5 Objectives & contributions

Recent technology advances of wavelength sweeping laser have led to a significant popularity increase in SS-OCT. As a result, several swept-source based JMT systems have been published and utilized in ophthalmology [82, 83, 85]. In addition, because of the advantages of optical fibers, such as convenient system alignment and handling, many JMT systems have been developed with fiber optics. However, the fiber causes a transformation of the polarization state due to its birefringence, which causes alternation into the input polarization state on the sample. Therefore, two different input polarization states with known relation are typically required. This requirement could be achieved by either sequential probing with two polarization states or multiplexing the two polarization states in one simultaneous axial scan acquisition. The former approach involves two or more sequential measurements, which results in slow acquisition rate and high phase noise. In the multiplexing case, for simultaneous detection of the signal from two incident polarization states, the imaging range is significantly reduced because of the limited detection bandwidth. Since high measurement speed is crucial for clinical usage of OCT in ophthalmology as described in Sect. 1.3, most of the current JMT systems have been built with the multiplexing scheme even with sacrifice of imaging range. The multiplexing of the incident polarization state is usually achieved with an active modulation device such as electro-optic modulator (EOM) or acousto-optic modulator (AOM), where proper encoding of the polarization states is important. Here, these polarization modulators give arise to high cost and complexity in handling the system with sophisticated synchronization controls.

The main objectives of this thesis are to implement a JMT system with high stability, to develop novel JMT algorithms for the enhancement of JMT imaging

capability, and to develop new clinical applications of JMT in the field of ophthalmology. The following contributions have been made in the course of achieving the objectives:

I implemented a JMT system for multi-functional ophthalmic imaging. I also designed a phase compensation unit based on the general characteristic of a polarization optical component, and integrated it with the JMT system. From the phase compensation unit, a static calibration signal was detected and used for estimating the spectral shift caused by jittering of wavelength scanning of the swept source.

I devised a phase stabilization process that is based on the cross-correlation of the calibration signal. A coherent composition algorithm was also developed in order to overcome the inherent sensitivity disadvantage of Jones matrix OCT image compared to conventional scattering OCT image. Based on the relationship between Jones vector and Stokes parameters, the degree of polarization uniformity (DOPU) quantity was extracted from the Jones matrix measurement. I also demonstrated the robustness and the effectiveness of the Jones matrix measurement.

Retinas of healthy and pathological subjects were measured *in vivo* using the JMT system, which demonstrated the functionality and clinical utility of the JMT system for posterior eye imaging. *In vivo* human eyelid imaging was also performed as a novel clinical application of JMT. For the first time, UV-A/riboflavin induced corneal collagen cross-linking (CXL) treatment effect on cornea was also investigated with the JMT system.

1.6 Outline

In Chapter 2, the general principle of Jones matrix measurement and typical implementation approaches of JMT are described.

In Chapter 3, an advance version of JMT system is introduced. This JMT is a combination of Doppler and PS-OCT, and enables simultaneously detection of tissue structure, tissue birefringence properties and flow in the tissue. Especially, this advanced JMT system is capable to measure full Jones matrix of the sample without any active modulation device that is typically applied for polarization modulation [82, 83]. With advanced signal processing, the phase stability of the OCT detection is enhanced, and high-sensitive Doppler imaging is performed. Owing to the high image quality and stability, the system is capable of investigating clinical subject.

In Chapter 4, an application of JMT system is demonstrated, where three-dimensional volumetric meibomian glands (MGs) visualization is presented. From the polarization contrasts provided by JMT such as phase retardation and degree of polarization uniformity (DOPU), distinctive features of the MGs and adjacent tissues are investigated. Segmentation of the conjunctiva layer located above the MGs is achieved with a DOPU threshold. Furthermore, investigation of the MGs variation with advancing age is also demonstrated by *in vivo* measurements of several subjects with different ages. Based on this investigation result, we introduce novel clinical utility of JMT for diagnosis of MG-related dry eye disease.

In Chapter 5, another application of JMT system is introduced, where the clinical outcome of riboflavin/UV-A induced collagen cross-linking treatment (CXL) is evaluated. *Ex vivo* measurement of fresh bovine eye is performed using JMT. From comparative study of the cross-linking effect with control groups, it is revealed that the main cause of corneal thinning followed by CXL is dehydration effect from

riboflavin solution. In addition, the effective cross-linking region is qualitatively differentiated by multi-contrast images created by JMT such as scattering, phase retardation, and DOPU images. Particularly, the effective cross-linking depth is estimated by applying empirical DOPU threshold. Two different CXL protocols (standard and accelerated CXL) are applied and their treatment outcomes are cross-examined in terms of the treatment effectiveness and progression.

Chapter 6 concludes this dissertation.

Chapter 2

Jones matrix tomography

The general principles of Jones matrix measurement and implementation concepts of various conventional JMT systems are provided in this chapter.

The primary objective of Jones matrix tomography (JMT) is to obtain the tomographies of the round-trip phase retardation, diattenuation, relative optic-axis orientation, and back-scattering intensity of a sample. To obtain these polarization parameters, JMT determines the Jones matrix or its similar matrix at each location in the sample. Since a matrix and its similar matrix have the same eigenvalues, the phase retardation, namely the phase difference between two eigenvalues, are derived from the similar matrix. The axis orientation is determined as the direction of the eigenvectors of the round-trip Jones matrix of the sample. Here it is noted that the absolute axis orientation cannot be obtained from the similar matrix because a matrix and its similar matrix do not always possess the identical eigenvectors. However, JMT still provides a relative optic-axis orientation from the similar matrix.

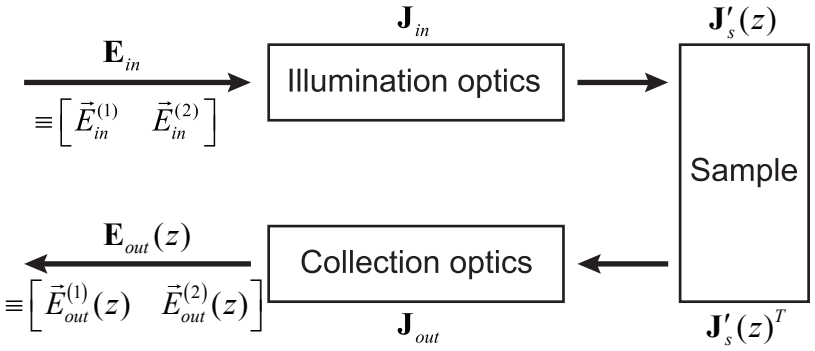

Figure 2.1: A conceptual scheme of polarization properties of Jones matrix tomography.

2.1 Principle of Jones matrix measurement

JMT determines a Jones matrix by measuring Jones vectors of two back-scattered probe beams. More precisely, by employing two incident polarization states and polarization diversity (PD) detection, JMT determines the polarization property of a sample through Jones matrix analysis [85, 86]. To mathematically describe this process, a simplified model of Jones matrix measurement done by JMT is introduced and its schematic is shown in Fig. 2.1.

In Fig. 2.1, $\mathbf{J}_{in}$ and $\mathbf{J}_{out}$ represent Jones matrices of the illumination and collection optics that may include the optical fiber, and $\mathbf{J}'_s(z)$ is a single-trip Jones matrix of a sample. By denoting the Jones vector of one of the incident polarization states as $\vec{E}_{in}^{(1)} = \left[H_{in}^{(1)} \quad V_{in}^{(1)}\right]^T$ (H and V represent horizontal and vertical components of polarization, respectively) and the corresponding OCT signals measured by the two detectors in the PD detection unit as $E_{out\,A}^{(1)}(z)$, $E_{out\,B}^{(1)}(z)$, and $\vec{E}_{out}^{(1)}(z) \equiv \left[E_{out\,A}^{(1)}(z) \quad E_{out\,B}^{(1)}(z)\right]^T$, the relationship between $\vec{E}_{in}^{(1)}$ and $\vec{E}_{out}^{(1)}(z)$ becomes

$$\vec{E}_{out}^{(1)}(z) = \chi \ \mathbf{J}_{all}(z) \ \vec{E}_{in}^{(1)} \tag{2.1}$$

where $\mathbf{J}_{all}(z)$ is the Jones matrix representing the overall polarization property including the Jones matrix of JMT system and the depth-resolved round trip Jones matrix of the sample. Here, χ is a general transform matrix which transforms the horizontal and vertical components of the Jones vector at the PD detection unit to the two arbitrary polarization components detected by the two detectors in the PD detection unit. In short, χ represents the imperfection of the PD detection. This includes the imbalance in the reference power of OCT detection, the gain imbalance of the photo-detectors, and the cross-talk between the two detectors. Similarly, the other incident polarization component and its corresponding OCT signals are related as

$$\vec{E}_{out}^{(2)}(z) = \chi \ \mathbf{J}_{all}(z) \ \vec{E}_{in}^{(2)}. \tag{2.2}$$

Note that, in a polarization multiplexing scheme based JMT, the OCT signals corresponding to $\vec{E}_{in}^{(1)}(z)$ and $\vec{E}_{in}^{(2)}(z)$ appear at two different frequencies and/or depths. Here, to avoid confusion, we define the variable z as the relative depth from each zero-delay point of each incident polarization component. Namely, equal values of z represent the same depth location in the sample.

Equations (2.1) and (2.2) can be combined as

$$\mathbf{E}_{out}(z) = \chi \ \mathbf{J}_{all}(z) \ \mathbf{E}_{in} \tag{2.3}$$

where $\mathbf{E}_{in} \equiv \begin{bmatrix} H_{in}^{(1)} & H_{in}^{(2)}; & V_{in}^{(1)} & V_{in}^{(2)} \end{bmatrix}$ and $\mathbf{E}_{out}(z)$ is a matrix of measured OCT signals

$$\mathbf{E}_{out}(z) = \begin{bmatrix} E^{(1)}_{out\,A}(z) & E^{(2)}_{out\,A}(z) \\ E^{(1)}_{out\,B}(z) & E^{(2)}_{out\,B}(z) \end{bmatrix}. \tag{2.4}$$

Note that, in Eq. (2.3), $\mathbf{E}_{out}(z)$ is a measured value, while $\mathbf{E}_{in}$ is a predefined but not accurately known matrix.

By considering the general configuration of JMT, $\mathbf{J}_{all}(z)$ can be decomposed into three components as

$$\mathbf{J}_{all}(z) = \mathbf{J}_{out}\ \mathbf{J}_s(z)\ \mathbf{J}_{in} \tag{2.5}$$

where $\mathbf{J}_{in}$ is the Jones matrix from the polarization delay unit to the sample surface, $\mathbf{J}_{out}$ is from the sample surface to the PD detection unit, and $\mathbf{J}_s(z) = \mathbf{J}'_s(z)^T\mathbf{J}'_s(z)$ is the round trip Jones matrix of the sample with that of the single trip being $\mathbf{J}'_s(z)$.

The purpose of the Jones matrix measurement is to determine the polarization properties of $\mathbf{J}_s$ through its eigenvalues. To obtain the eigenvalues, a similar matrix of $\mathbf{J}_s$ is obtained by the following protocol. First, the surface of the sample is segmented, and $\mathbf{E}_{out}$ is obtained at the sample surface as $\mathbf{E}_{out}(z_0)$, where z_0 represents the depth position of the surface. Then, a similar matrix of the $\mathbf{J}_s(z)$ at each location in the sample is obtained as

$$\begin{aligned} \mathbf{E}_{out}(z)\ \mathbf{E}_{out}(z_0)^{-1} &= \chi\ \mathbf{J}_{out}\ \mathbf{J}_s(z)\ \mathbf{J}_{in}\ \mathbf{E}_{in}\ \ (\chi\ \mathbf{J}_{out}\ \mathbf{J}_{in}\ \mathbf{E}_{in}\ )^{-1} \\ &= \chi\ \mathbf{J}_{out}\ \mathbf{J}_s(z)\ \mathbf{J}_{in}\ \mathbf{E}_{in}\ \mathbf{E}_{in}^{-1}\ \mathbf{J}_{in}^{-1}\ \mathbf{J}_{out}^{-1}\ \chi^{-1} \\ &= \chi\ \mathbf{J}_{out}\ \mathbf{J}_s(z)\ \mathbf{J}_{out}^{-1}\ \chi^{-1} \end{aligned} \tag{2.6}$$

This equation indicates that using the two measured matrices $\mathbf{E}_{out}(z)$ and $\mathbf{E}_{out}(z_0)$, we can define the similar matrix of the round-trip Jones matrix of the sample and hence its eigenvalues. Here, $\mathbf{E}_{out}(z_0)\,(=\chi\ \mathbf{J}_{out}\ \mathbf{J}_{in}\ \mathbf{E}_{in}\ )$ represents the system-oriented birefringence that can be cancelled after multiplying $\mathbf{E}_{out}(z)$ with the inverse of $\mathbf{E}_{out}(z_0)$. It is noteworthy that JMT provides the similar matrices regardless of the combination of the input polarization states, except when the two states are parallel to each other [86].

2.2 Multiplexing of incident polarization states

In Jones matrix measurement, two polarization states are multiplexed by several means including time-division multiplexing [85], polarization modulation along the transversal scan (mainly for SD-OCT) [82] or along the wavelength scan (only for SS-OCT) [83], frequency shifting [87], and delay-based multiplexing [88, 89].

In the time-division multiplexing scheme [85], two polarization states of the incident beam are sequentially switched for A-line by A-line. This method is the most straightforward implementation of incident polarization multiplexing. Because of the sequential measurements with different polarization states, however, it is not suitable for high-speed measurement.

In the multiplexing scheme based on polarization modulation along the transverse scan, the phase of a polarization component of incident light is modulated by a sinusoidal function along the transversal scanning direction. By this modulation, two incident beams with two polarization states are multiplexed such that one is modulated in phase and the other is not. After OCT detection, these two multiplexed components are demultiplexed by spatial frequency filtering based on a numerical Fourier transform along the transversal direction [82]. The modulation is

typically performed by an electro-optic modulator (EOM) as shown in Fig. 2.2. The EOM is configured to modulate the relative phase of the polarization component of a probe beam that is oriented to one of the axes of the modulator (so denoted as EOM axis) in respect to the phase of the OCT reference beam, while the relative phase of the polarization component oriented to the other axis (non-EOM axis) is not modulated. The frequency of the modulation is defined with respect to the A-line frequency of the OCT detection so that it is several fractions of the A-line frequency. In this transversal modulation scheme, the probe locations on the sample corresponding to the two incident polarizations are slightly displaced to each other because the EOM alters the incident polarization states for each A-line. This small displacement results in a structural decorrelation between the two OCT signals associated with the two incident polarization states and it finally degrades the sensitivity of the Jones matrix measurement. In order to minimize the sensitivity degradation, the A-line can be densely scanned in space so that the separation between the adjacent A-lines is less than a fraction of the transversal optical resolution. As a result, however, the wide-range and high-speed measurement are in contradiction to each other with the transversal modulation scheme.

A variation of the above mentioned multiplexing method is the polarization modulation along the wavelength scan. In particular, this multiplexing scheme is only applicable to SS-OCT. The phase modulation is performed by the EOM with a similar optical scheme to that in Fig. 2.2, but along the wavelength scan. Similar to the modulation along the transversal scan, the two incident polarization states are demultiplexed by frequency filtering but based on a numerical Fourier transform along the wavelength scan [83]. Unlikely to the above mentioned transversal modulation method, in this wavelength scan oriented modulation scheme, the OCT

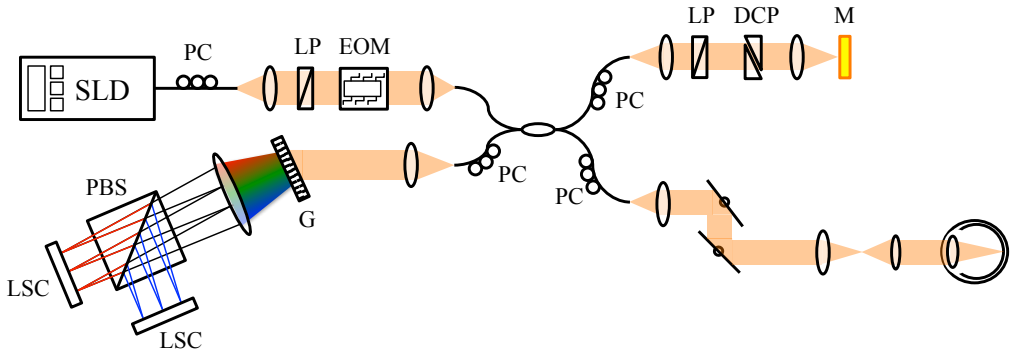

Figure 2.2: Example of the optical scheme for polarization modulation along the transversal scan. SLD is a superluminescent diode light source, PCs are polarization controllers, LPs are linear polarizers, DCP is dispersion compensation prism, ND is neutral density filter, EOM is an electro-optic modulator. This example system is equipped with a polarization diversity spectrometer composed of a grating (G), a polarization beam splitter (PBS), and two line scan CCD cameras.

signals associated with two incident polarization states are obtained at exactly the same time and location. Hence the structural decorrelation does not occur. This property makes the wavelength oriented modulation scheme suitable for high-speed and wide-range measurements.

There is also unique multiplexing method for SS-OCT named as frequency shifting-based multiplexing [87]. In this scheme, the frequencies of the two incident beams with orthogonal polarization states are frequency-shifted by two frequency shifter with different shifting frequencies. Namely, two incident polarization states are multiplexed in its frequency. The multiplexed incident beams would have different carrier frequency after interference with a reference beam, and these beams are demultiplexed by numerical Fourier transform. To avoid unwanted interference, this scheme is equipped with an unpolarizer, which is a polarization dependent delay unit generating a path length difference more than the instantaneous coherence length of the light source between the two polarization states.

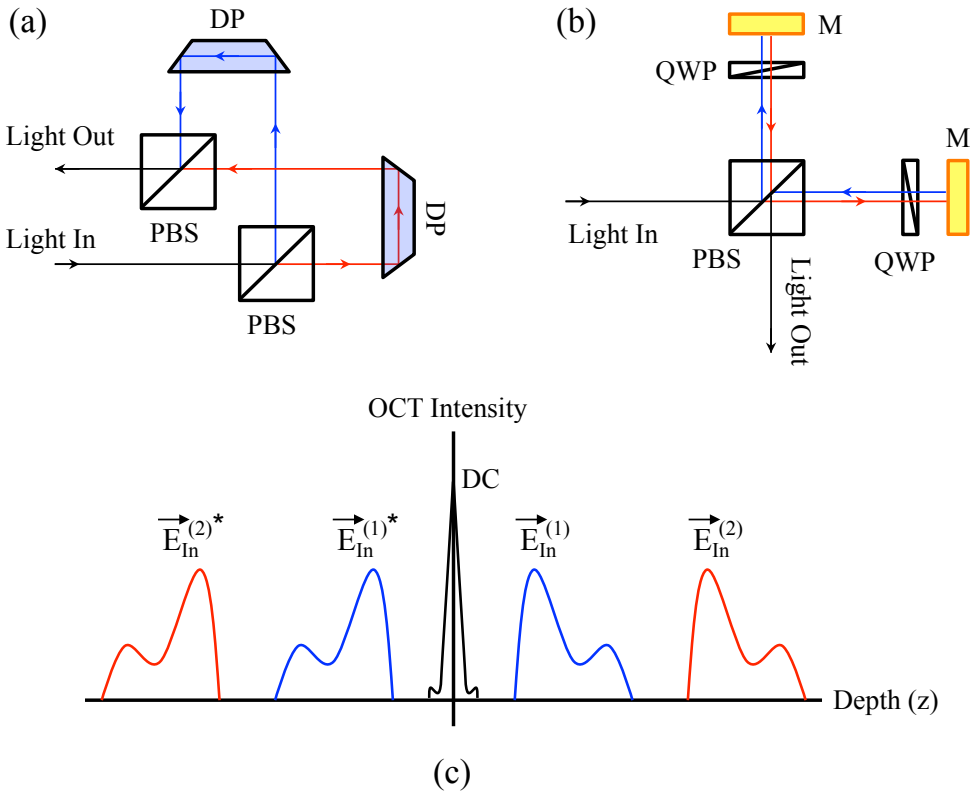

Figure 2.3: Schematics of delay based input polarization multiplexing and demultiplexing. (a) and (b) the optical schemes for delay based input polarization multiplexing. PBSs are polarization beam splitter, DPs are Dove prisms, QWPs are quarter wavelength plates and Ms are mirrors. (c) A schematic figure of demultiplexing two incident polarization components. The OCT images associated with two incident polarization states appear at different depths.

Most recently developed multiplexing scheme is the delay-based incident polarization multiplexing. If the coherence length of the light source in SS-OCT or spectral resolution of the spectrometer in SD-OCT is large and hence the depth measurement range of the OCT is sufficiently long, the two incident polarizations can also be multiplexed at two different depths. This polarization dependent spectral delay can be implemented, for example, by two polarization beam splitters (PBSs) and two Dove prisms as depicted in Fig. 2.3(a) [88] or by the combination of a PBS

and two quarter wave plates (QWPs) as depicted in Fig. 2.3(b) [89]. Since the OCT images associated with the two incident polarization states appear at different depths as depicted in Fig. 2.3(c), it can be easily demultiplexed by cropping the specific portions of the OCT images. Since this scheme does not require any active optical components, such as the EOM, it is stable and the sequential control of this type of JMT would be simpler than those of using polarization modulation schemes.

Table 2.1 shows the summary of different incident polarization multiplexing methods.

Table 2.1: Summary of incident polarization multiplexing methods

Type	**Time division**	**Polarization modulation**	**Frequency shifting**	**Path-length delay**
Multiplexing device	Electro-optic or Acousto-optic modulators	Electro-optic or Acousto-optic modulators	Pair of Frequency shifters	Optical delay unit
Demultiplexing complexity	Simple	Complex	Complex	Simple
Usage of active device	Yes	Yes	Yes	No
Measurement speed (restiction)	Slow (Modulator frequency)	Moderate (Modulator frequency)	Moderate (Shifter frequency)	Fast - CCD camera - sweeping rate
Measurable depth range	Full range	Full range	Half of full range	Half of full range

2.3 Polarization-diversity detection

In JMT, the Jones vector of the back-scattered probe beam after the collection optics, i.e. $\vec{E}^{(1)}_{out}(z)$ and $\vec{E}^{(2)}_{out}(z)$ of Fig. 2.1, is measured by a polarization-diversity (PD) detection unit. In the PD detection unit, two orthogonal polarization components, typically horizontal and vertical, of the probe and reference beams are split by a PBS or a Wollaston prism and detected by two detectors, except for some sophisticated PD detection units that use a single detector.

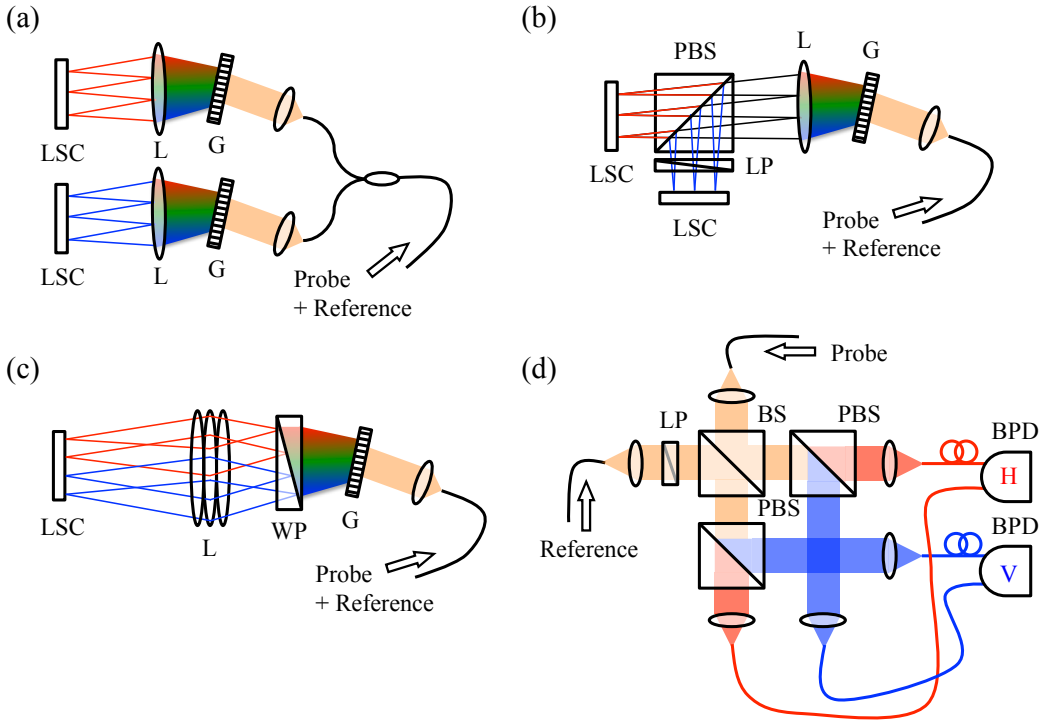

Figure 2.4: Polarization-diversity detection unit. (a)-(c) examples of polarization-diversity spectrometer. (d) polarization-diversity balanced detection unit. L: lenses, G: grating, LS: line sensors grating, PBS: polarization beam splitter, LP: linear polarizer, WP: Wollaston prism, BS: non-polarization beam splitter, and BPD: balanced photo-detector.

A PD spectrometer is a detection unit specifically utilized for SD-OCT. Although there are some variations, all of them split the two orthogonal polarization components after combining the reference and probe beams in an interferometer. Figure 2.4(a) is a straightforward implementation of PD spectrometer, which was originally developed for a Hee-Hitzenberger type PS-OCT [72]. In this scheme, the probe and reference beams are combined in an OCT interferometer and then introduced into the PD spectrometer unit. In this spectrometer unit, the horizontal and vertical polarization components of the probe beams are split by a fiber PBS and detected by two independent spectrometers. This PD spectrometer is a very straightforward implementation and is hence easy to design. On the other hand, it requires two whole spectrometers and thus results in double the implementation cost. In addition, it is sometimes difficult to obtain a fiber PBS with sufficient quality for some wavelength bands.

Figure 2.4(b) is the PD spectrometer using only one diffraction grating [82]. The vertical and horizontal polarization components are resolved into its spectral components by a single diffraction grating, and then split into two polarization components by PBS. The two polarization components are then detected by two line sensors. Since the purity of polarization of a reflected beam by PBS is relatively low, a polarizer after reflection (so-called clean-up polarizer) can be optionally utilized in order to improve the purity and the accuracy of Jones vector measurement. This type of PD spectrometer is relatively easy to design, but it sometimes requires a large PBS to cover the whole area of the line sensors.

Figure 2.4(c) shows one of the sophisticated designs of PD spectrometers using only one line sensor that was originally developed for Stokes parameter-based PS-OCT [68]. In this scheme, the two polarization components are displaced relative

to each other by the Wollaston prism, and two spectra corresponding to the two polarization components illuminate different areas of a single line sensor. This scheme requires fewer optical components than the other schemes and can be compactly implemented in size. On the other hand, it requires more careful optic design to suppress aberrations to obtain high spectral resolution for both of the polarization components.

Figure 2.4(d) shows a balanced PD detection unit for SS-OCT [83]. The probe and reference beams are introduced into this detection unit through two independent fiber ports. The two beams are combined by a non-polarization beam splitter (BS) and then decomposed into its polarization components by two PBSs. Each of the polarization components is then detected by two balanced photo-detectors (BPDs).

Similar to the configuration shown in Fig. 2.4(b), the purity of the polarization can be improved using clean-up polarizer. The polarizer at the input port of the reference beam is to balance the optical powers of the reference beam between the two detection channels.

2.4 Summary

The principle of Jones matrix measurement and conventional implementations of JMT is presented in this chapter. This chapter is organized to provide an introduction and overview of JMT. An advanced version of JMT and more comprehensive explanations about system configuration and Jones matrix algorithm are introduced in Chapter 3

Chapter 3

Advanced Jones matrix tomography*

In this chapter, an advanced version of JMT system and newly developed algorithms are introduced.

3.1 Introduction

Recently, Lim *et al.* [88] and Baumann *et al.* [89] independently developed Jones matrix tomography (JMT) systems using passive optical components for the delay-based incident polarization multiplexing described in Sect. 2.2. These systems realized Jones matrix measurement without any active modulation devices, e.g. electro-optic or acousto-optic modulators. In particular, a fiber-based multi-contrast Jones matrix swept-source OCT [88] was used for simultaneous Doppler and polarization

*This chapter has been mainly adopted from the following publication:
M. J. Ju, Y.-J. Hong, S. Makita, Y. Lim, K. Kurokawa, L. Duan, M. Miura, S. Tang, and Y. Yasuno, "Advanced multi-contrast Jones matrix optical coherence tomography for Doppler and polarization sensitive imaging," Opt. Express **21**, 19412-19436 (2013)

imaging. As measuring both a standard wave plate and a retina of a healthy subject *in vivo*, accuracy of the polarization detection and its functionality was verified. Because of the depth-encoded polarization multiplexing method, however, the measurable depth range was relatively shorter than that of a non-polarization OCT system. Furthermore, its phase instability and relatively low imaging quality limit the system for clinical applications.

In this chapter, an advanced version of JMT is demonstrated. In comparison to previously reported JMT [88, 89], this new JMT is advanced in terms of phase stability, image quality, and imaging depth. In addition, this JMT is based on a new principle in which all of the measurements of scattering OCT, Doppler OCT and PS-OCT are integrated. Distinct features of the system and post-processing algorithms are also concretely described. Furthermore, I show the measurement results of a healthy and clinical case subject in order to demonstrate the clinical utility of the system in ophthalmology.

3.2 Methods

3.2.1 System

3.2.1.1 System configuration

Figure 3.1 shows the schematic of the JMT system. An MEMS-based swept-source (Axsun Technology Inc., MA) with a center wavelength of 1.06 μm, FWHM of 111 nm, and scanning width of 123 nm is used as a light source. The scanning rate of the light source is 100 kHz, and the average output power is 30 mW.

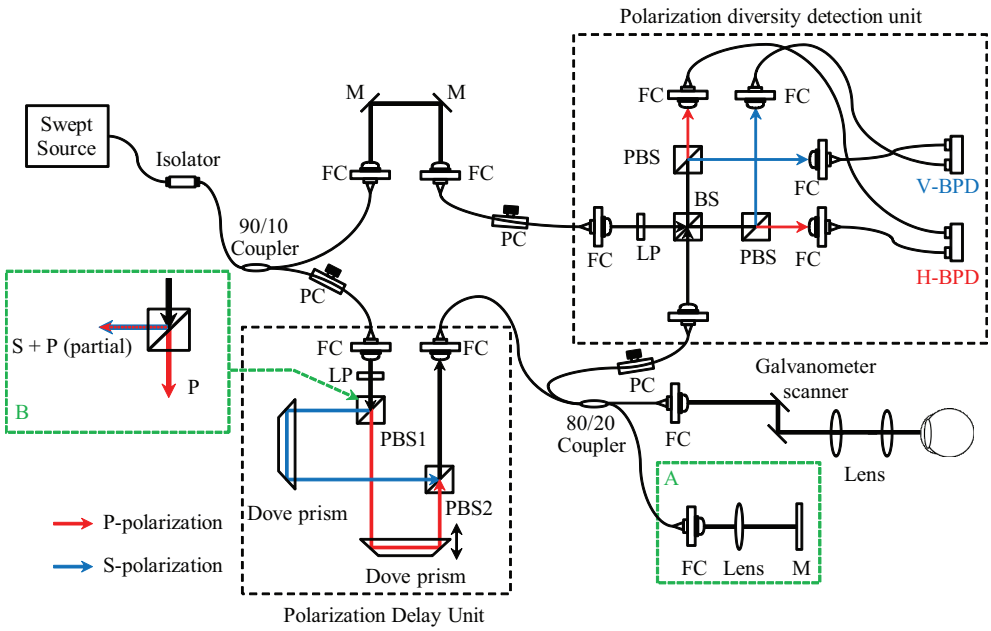

Figure 3.1: Schematic diagram of advanced JMT system. LP: linear polarizer, PC: polarization controller, FC: fiber collimator, M: mirror, PBS: polarizing beam splitter, BS: beam splitter, H- and V-BPD: balanced photo-detector for horizontally and vertically polarized signals, respectively. (Source: **Ju *et al.*** *Advanced multi-contrast Jones matrix optical coherence tomography for Doppler and polarization sensitive imaging* [90])

The interferometer is built with single-mode optical fibers. The light is split by a 90:10 single-mode optical fiber coupler after passing through an isolator used for the protection of the source from back-reflected lights. The 90 % port of the fiber coupler is connected to a probe arm consisting of a polarization controller and a passive polarization delay unit, described in Sect. 3.2.1.2. The 10 % portion of the light from the coupler is coupled to a reference arm.

The light from the polarization delay unit passes through an 80:20 fiber coupler. The 80% portion of the light is directed to a calibration reflector (box-A in Fig. 3.1) composed of a fiber collimator, lens, and mirror, and the remaining 20% portion of the light illuminates the eye after passing through a collimator (F280 APC-C, Thorlabs Inc., NJ), a two-axis galvanometer scanner, an objective lens (f = 60 mm), and an aspheric ophthalmic lens (40D, Volk Optical Inc., OH). The beam diameter ($1/e^2$) incident on the cornea is around 1.4 mm, which provides a theoretical diffraction-limited spot size ($1/e^2$) of 21 μm on the retina. The optical power on the cornea is configured to be around 1.15 mW in order to satisfy the safety standard defined by ANSI [34]. The back-scattered light from the retina is recoupled to the 80:20 coupler, and 80 % of the back-scattered light is directed to a polarization diversity (PD) detection unit.

The PD detection unit consists of a linear polarizer, a non-polarizing beam splitter (BS), two polarizing beam splitters (PBSs), and two 350 MHz balanced photo-detectors (BPDs, PDB430C, Thorlabs Inc.). The reference light coupled through the 90:10 fiber coupler is also directed to the PD detection unit, in which a linear polarizer is embedded for aligning the polarization state of the light to 45-degree angle. In the PD detection unit, the reference and back-scattered light from the eye is combined at the BS, then split into horizontal and vertical polarization

components by the two PBSs, and finally detected by the BPDs. The detected signals from the BPDs are sampled by an ATS9350 digitizer (AlazarTech Inc., Pointe Claire, QC, Canada) with 12-bit resolution and a sampling rate of 500 MHz after passing through a high-pass (1.5 MHz) and low-pass (250 MHz) filter (HP1CH3-0S and LP250Ch3-0S, R&K Co. Ltd., Shizuoka, Japan). Here, the interference signal is sampled with 2560 sampling points for each A-line and the effective wavelength range being sampled is approximately 110 nm. The sampled interference signals are rescaled to the linear frequency domain using pre-defined rescaling parameters determined by a time-frequency calibration method [91]. The rescaling algorithm also cancels the spectral shift among A-lines and stabilizes the phase of the OCT signal as described in Sect. 3.2.2.1. After applying a Gaussian window, the interference signal is Fourier transformed to yield an OCT signal. For the retinal measurement, the chromatic dispersion of the eye as well as the residual dispersion of the interferometer is canceled by a method described in Ref. [92]. The scanning property of the light source, the parameters for the sampling of the spectral interference signal, and the windowing finally define the measured depth-resolution to be 8.5 μm in air, corresponding to 6.2 μm in tissue.

With an average probe power of 1.15 mW, the sensitivity is 91.05 dB and the signal roll-off measured at 0.3 to 2.6-mm depth range is -0.65 dB/mm. According to the literal definition of sensitivity, it is the maximum measurable attenuation of the probe beam represented as a negative value in dB. In this thesis, the negative sign is omitted by following the conventional notation. Because the signal energy is split into the four OCT images, the sensitivity of the system measured for a single image is 6-dB lower than that of standard OCT. This fundamental sensitivity loss is overcome by a method discussed in Sect. 3.2.2.5. By accounting the inherent loss of the 80:20

coupler, the shot-noise-limited sensitivity of a single image becomes 99.4 dB. The departure of the measured sensitivity from the shot-noise-limited sensitivity by -8.4 dB is accounted by the double-pass transmittance of the posterior-eye-scanning unit, which is measured to be -3.8 dB, the fiber-coupling loss at the PD detection unit, which is measured to be -3.7 dB and possible recoupling loss at the fiber-tip in the scanning unit occurred by the misalignment of the mirror target for the sensitivity measurement.

3.2.1.2 Incident polarization multiplexing by polarization delay unit

A passive polarization delay unit is used to multiplex two incident polarization states by applying the optical path lengths difference (OPLD). As shown in Fig. 3.1, the passive polarization delay unit consists of a linear polarizer, two PBSs, and two Dove prisms. In this delay unit, the collimated light passes through a linear polarizer oriented at 45-degree angle and splits into two orthogonal polarization components by the PBS 1. After the internal reflection in the Dove prisms, the two orthogonally polarized lights are combined by the PBS 2, then coupled to an optical fiber connected to the 80:20 fiber coupler.

The two incident polarization states are multiplexed in depth position, and the OPLD is adjusted by moving one of the Dove prisms. In our particular setup, the OPLD is adjusted to $z_d = 3.1$ mm, so the two OCT signals corresponding to the two multiplexed incident polarization states appear with a depth separation of 3.1 mm. With this configuration, the measurable imaging depth range for each signal is determined to be around 2.95 mm, which is large enough for clinical imaging of pathologic posterior eyes.

Since this polarization delay unit is compact in size and consists only of bulk

optical components, the perturbation of the delay caused by temperature fluctuation is negligible. In addition, this polarization delay unit relies only on passive polarization components. This results in high stability and easy operation of the JMT system.

3.2.1.3 Polarization diversity detection

Like the other JMT systems, this JMT also relies on PD detection, by which two interference signals corresponding to different polarization states are independently detected. It should be noted that the two polarization states are not necessarily identical to those of the polarization delay unit. By this detection scheme, two interference signals of different polarization states are simultaneously detected by two balanced photo-detectors. Each interference signal generates two OCT images at different depth positions, which correspond to the two incident polarization states multiplexed by the polarization delay unit. Finally, owing to the PD detection and the incident polarization multiplexing, four OCT images are simultaneously acquired as schematically shown in Fig. 3.2.

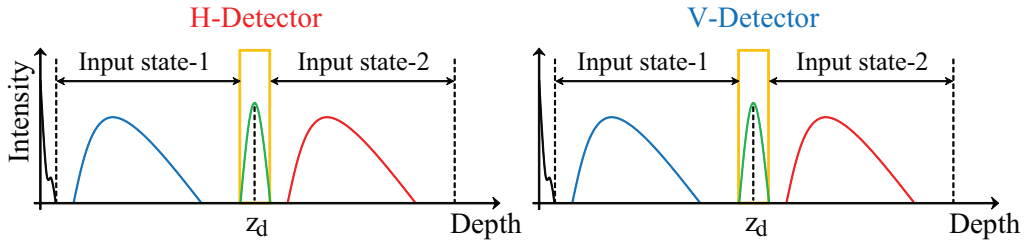

Figure 3.2: Diagram of the Fourier transformed interference signals from horizontal (H) and vertical (V) detection channels. (Source: **Ju *et al.*** *Advanced multi-contrast Jones matrix optical coherence tomography for Doppler and polarization sensitive imaging* [90])

3.2.1.4 Phase calibration reflector

In this JMT system, the fluctuations in spectral sampling timing among OCT A-lines are monitored and canceled using a stable spectral interference fringe denoted as a calibration signal. The generation of a calibration signal relies on the imperfection of the PBSs in the polarization delay unit. Ideally, the PBS separates S- and P-polarization components by reflecting only the S-polarization component and transmitting only the P-polarization component. However, with an off-the-shelf PBS, some portion of the P-polarization component is reflected and mixed with the S-polarization component. At the 1.06-μm wavelength, according to the manufacturer's specifications, the reflected beam of the PBS employed in the passive polarization delay unit (NT49-870, Edmund Optics Inc., NJ, US) includes 4.4% of P-polarization.

Owing to this imperfection of the PBS, the polarization delay unit behaves as a Mach-Zehnder interferometer with an OPLD of z_d for the P-polarization component and generates the calibration signal. The calibration signal is directed to the BPDs in the PD detection unit through the 80:20 fiber coupler and a calibration reflector (box-A in Fig. 3.1). Note that the calibration signal generated by the polarization delay unit is a common-mode signal for the BPDs. However, the optical power of the calibration signal is significantly larger than that of OCT signal, and hence it can be detected even with the common-mode-rejection property of the BPD.

As shown in the orange squares in Fig. 3.2, the calibration signal appears at the depth location of z_d that is exactly the axial displacement between the two depth-multiplexed signals. This calibration signal is used to correct the fluctuation of spectral sampling as described in Sect. 3.2.2.1.

It is noteworthy that the imperfection of PBS does not disturb the polarization sensitive measurement because of the inherent robustness of JMT, which is more precisely discussed in Sect. 3.4.4.

3.2.2 Post-processing

3.2.2.1 Monitoring and correction of spectral shift

Fluctuations in the synchronization between the wavelength sweeping of the light source and the digitizer cause random shifts of the digitized spectrum among the A-lines, which result in phase instability. The phase instability could impose errors on the phase measurements and degrades the sensitivity of Doppler OCT measurements. In addition, phase instability results in reduced performance of numerical cancellation of fixed pattern noise. Hence, the spectral shift needs to be correctly estimated and canceled. In previous systems, the spectral shift was corrected by several means [45,50,83,93,94]. In the current JMT, I utilize a new method specialized for the JMT which is simple in its hardware configuration.

To obtain phase-stabilized OCT, the spectral shift is estimated and canceled using the calibration signal described in Sect. 3.2.1.4. Since the same amount of spectral shift occurs in both detection channels of the PD detection, the calibration signal with the higher signal-to-noise ratio is used to estimate the spectral shifts of both channels.

The details of the estimation of the spectral shift are as follows. In this estimation, the relative shift between the two spectra are obtained. One of the two spectra is denoted as a reference spectrum, and is typically the first A-line of a B-scan. The other spectrum is the spectrum under shift correction and its shift is corrected with respect to the reference spectrum. For the estimation, two

of the digitized spectra are first Fourier transformed without rescaling. After this Fourier transform, the calibration signals appear between the two OCT signals of the two incident polarization components as shown in Fig. 3.2 (green signals) and are selected by a binary window function.

For an intuitive understanding of the method, I consider the inversely Fourier transformed spectra of the windowed calibrated signals of the reference spectrum ($I_r(j)$) and the spectrum under shift-correction ($I_c(j)$). These spectra are described as

$$I_r(j) = |E_r(j) + E_t(j)|^2 \tag{3.1}$$

$$I_c(j) = |E_r(j - \beta_j) + E_t(j - \beta_j)|^2 = I_r(j) * \delta(j - \beta_j) \tag{3.2}$$

where $E_r(j)$ and $E_t(j)$ are the sampled spectra of the reflected and transmitted beams of the polarization delay unit with a spectral sampling index of j. The $*$ denotes the convolution operation, and β_j indicates the relative shift of the spectrum in number of sampling points.

In the spectral shift estimation process, the numerically Fourier transformed calibration signal of the reference A-line is multiplied with the complex conjugate of the Fourier transformed calibration signal of the A-line under correction as

$$\mathcal{F}[I_r(j)]\,\mathcal{F}[I_c(j)]^* = \mathcal{F}[I_r(j)]\,\mathcal{F}[I_r^*(-j)]\,\mathcal{F}[\delta(-j - \beta_j)] \tag{3.3}$$

where $\mathcal{F}[\ ]$ represents the Fourier transform and the superscript of $*$ represents the complex conjugate.

The numerical inverse Fourier transform of the signal represented by Eq. (3.3) yields

$$\begin{aligned}\mathcal{F}^{-1}\left[\mathcal{F}\left[I_r(j)\right]\mathcal{F}\left[I_c(j)\right]^*\right] &= I_r(j) * I_r^*(-j) * \delta(-j-\beta_j) \\ &= \{I_r(j) \otimes I_r(j)\} * \delta(-j-\beta_j)\end{aligned} \tag{3.4}$$

where $\otimes$ represents the correlation operation. $I_r(j) \otimes I_r(j)$ is the auto-correlation of $I_r(j)$. It would have a maximum at $j = 0$, so the signal represented by Eq. (3.4) has its maximum at $j = -\beta_j$. Finally, the amount of spectral shift β_j is determined by detecting the peak of this signal. It is noteworthy that the accuracy of the spectral shift estimation can be enhanced by zero-padding the signal of Eq. (3.3). In our particular case the sampling number of the spectrum is zero-padded to yield a sampling number 16-times larger than the original, thus the spectral shift is determined with an accuracy of 1/16 of the original spectral sampling period.

The estimated β_j is then added to the predetermined rescaling table, which is a vector of sub-fractional indexes of spectral sampling points for each rescaled sampling point. The A-line under correction is then rescaled using this modified rescaling table and a shift-corrected and rescaled spectrum is obtained.

In the spectral estimation method described in this section, the sampled spectra are Fourier transformed without being rescaled into the linear frequency domain. And hence the calibration signal have a broad width after the Fourier transformation, which is typically around 70 pixels width, and sometimes overlaps with an interference signal originated from the sample. However, due to the significantly higher SNR of the calibration signal with respect to those of the sample signal, the calibration signal still overwhelmingly dominates the spectral shift estimation. As a result, this estimation method shows remarkable performance as discussed in Sect. 3.4.1.

3.2.2.2 Phase retardation and relative attenuation calculation

The round-trip phase retardation of the sample is obtained from the similar matrix obtained through Eq. (2.6). The eigenvalues of the round-trip sample Jones matrix can be obtained through matrix diagonalization [82] or the following equation [95]

$$\lambda_{1,2} = T/2 \pm \sqrt{T^2/4 - D} \tag{3.5}$$

where T and D are the trace and determinant of the similar matrix, and $\lambda_{1,2}$ indicates the two eigenvalues of the matrix. Here I have utilized the fact that the eigenvalues of the similar matrix are identical to those of the round-trip Jones matrix of the sample.

The phase retardation $\delta(z)$ is then obtained as the phase difference between the two eigenvalues as

$$\delta(z) = \begin{cases} \mathrm{Arg}\left[\lambda_1 \lambda_2^*\right] & : \quad 0 \leq \mathrm{Arg}\left[\lambda_1 \lambda_2^*\right] \leq \pi \\ \mathrm{Arg}\left[\lambda_1^* \lambda_2\right] & : \quad \text{otherwise} \end{cases} . \tag{3.6}$$

Note that $\delta(z)$ is defined to be aliased into the range of $[0, \pi]$ because the assignment of λ_1 and λ_2 is unspecified.

In addition to the phase retardation, the relative attenuation between the two characteristic polarization states $\epsilon(z)$ is obtained as

$$\epsilon(z) = \left| \ln \frac{|\lambda_1|}{|\lambda_2|} \right| \tag{3.7}$$

3.2.2.3 Adaptive Jones matrix averaging

To obtain a high quality phase retardation image, adaptive Jones matrix averaging can optionally be applied to the similar Jones matrices. Note that the basic con-

cept of adaptive Jones matrix averaging was firstly described in Ref. [56] and was previously called as complex Jones averaging.

This method relies on a weighted least-square estimation of the relative global phase of a Jones matrix in respect to an arbitrary reference Jones matrix. Consider several Jones matrices $\mathbf{M}^{(j)}$ (or similarly several of $\mathbf{E}_{out}$) obtained in a single homogeneous birefringence domain of a sample but not within a coherence volume, i.e. the resolution of OCT. Under this condition, it would be rational to assume the following relationship: $\mathbf{M}^{(0)} \simeq \exp\left(i\,\Delta\varphi^{(0,j)}\right)\mathbf{M}^{(j)}$. Here $\Delta\varphi^{(0,j)}$ is the relative global phase between $\mathbf{M}^{(0)}$ and $\mathbf{M}^{(j)}$. The basic concept of adaptive Jones matrix averaging is averaging $\mathbf{M}^{(j)}$ after canceling the global phase.

In the adaptive Jones matrix averaging method, the global phase between two Jones matrices is estimated as

$$\Delta\varphi^{(0,j)} \equiv \mathrm{Arg}\left[\sum_{l=1}^{4} \frac{\exp i\left(\mathrm{Arg}\left[M_l^{(j)}/M_l^{(0)}\right]\right)}{\left|M_l^{(0)}\right|^{-1} + \left|M_l^{(j)}\right|^{-1}}\right], \tag{3.8}$$

where $M_l^{(j)}$ is the l-th entry of the j-th matrix under averaging.

After determining the global phase, the averaged matrix is defined as

$$\overline{\mathbf{M}} \equiv \sum_j \exp\left(-i\,\Delta\varphi^{(0,j)}\right)\mathbf{M}^{(j)}. \tag{3.9}$$

Note that $\mathbf{M}^{(0)}$ is a reference matrix for the determination of the global phase. Hence the phase noise of this matrix should be small. In practical processing, the Jones matrix possessing the highest total signal energy among the matrices being averaged is utilized as $\mathbf{M}^{(0)}$.

In practical JMT measurement, this adaptive Jones matrix averaging is optionally applied to the similar matrices ($\mathbf{E}_{out}(z)\mathbf{E}_{out}(z_0)^{-1}$ in Eq. (2.6)) with an

averaging kernel smaller than the birefringence domain of the sample prior to calculating the eigenvalues.

3.2.2.4 Degree of polarization uniformity calculation

Degree of polarization uniformity (DOPU) is a parameter originally introduced by Götzinger *et al.* [74] for representing the spatial uniformity of polarization. Since some important tissues such as retinal pigment epithelium (RPE) are selectively visualized by DOPU contrast, DOPU imaging by JMT is of great interest.

DOPU was first defined by using the Hee-Hitzenberger type PS-OCT [75] and recently applied for JMT [89]. In our JMT, DOPU is obtained directly from $\mathbf{E}_{out}(z)$ (in Eq. (2.4)) by the following method.

Since DOPU is defined based on the Stokes parameters of back-scattered light, a virtual incident beam with an arbitrary state of polarization is defined. To simplify computation, a virtual incident polarization state of $\mathbf{E}_{out}(z_0)[1 \quad 0]^T$ from Eq. (2.6) is assumed. When this virtual incident light illuminates the similar matrix of the round-trip Jones matrix, $\mathbf{E}_{out}(z)\mathbf{E}_{out}(z_0)^{-1}$ in Eq. (2.6), the Jones vector of the output light becomes $\mathbf{E}_{out}(z)[1 \quad 0]^T = \left[E^{(1)}_{out\,A}(z) \quad E^{(1)}_{out\,B}(z)\right]^T$. The corresponding Stokes parameters are then defined as

$$\mathbf{S} = \begin{bmatrix} I \\ Q \\ U \\ V \end{bmatrix} = \begin{bmatrix} \left|E^{(1)}_{out\,A}(z)\right|^2 + \left|E^{(1)}_{out\,B}(z)\right|^2 \\ \left|E^{(1)}_{out\,A}(z)\right|^2 - \left|E^{(1)}_{out\,B}(z)\right|^2 \\ E^{(1)}_{out\,A}(z)E^{(1)}_{out\,B}(z)^* + E^{(1)}_{out\,A}(z)^*E^{(1)}_{out\,B}(z) \\ i\left(E^{(1)}_{out\,A}(z)E^{(1)}_{out\,B}(z)^* - E^{(1)}_{out\,A}(z)^*E^{(1)}_{out\,B}(z)\right). \end{bmatrix} \tag{3.10}$$

Note that these Stokes parameters are only calculated from two OCT signals obtained from the PD detection unit.

DOPU is then defined as

$$\text{DOPU} = \sqrt{\overline{Q}^2 + \overline{U}^2 + \overline{V}^2} \tag{3.11}$$

with

$$(\overline{Q}, \overline{U}, \overline{V}) = \left(\sum_i \frac{Q_i}{I_i}, \sum_i \frac{U_i}{I_i}, \sum_i \frac{V_i}{I_i} \right) \tag{3.12}$$

where i indicates the i-th pixel within a spatial kernel by which DOPU is defined. It should be noted that this DOPU is not directly determined from the polarization property of the sample $\mathbf{J}_s(z)$, but from $\mathbf{E}_{out}(z) = \chi \, \mathbf{J}_{out} \, \mathbf{J}_s(z) \, \mathbf{J}_{in} \, \mathbf{E}_{in}$. However, it would provide a reasonable measure of the sample's DOPU, because χ, $\mathbf{J}_{out}$, $\mathbf{J}_{in}$, and $\mathbf{E}_{in}$ can be regarded as constant in space and time.

In our particular implementation, the kernel size of 8 pixels (horizontal) $\times$ 3 pixels (vertical) (70 μm $\times$ 12 μm) is used, which is experimentally determined to provide best result in RPE segmentation [74].

3.2.2.5 Coherent composition of matrix entries

In previous multi-contrast OCT based on JMT, a scattering OCT image was obtained by averaging the four entries of a Jones matrix in squared intensity. Similarly, Doppler tomography was obtained by averaging the squared power of the four Doppler phase shift signals of the four entries of the Jones matrix [88]. Although this method provided satisfactory image quality, it still suffered fundamental sensitivity degradation of JMT, caused by splitting a probe beam power into four OCT images, i.e. the four entries of the Jones matrices.

To overcome this issue, I introduce a new advanced signal processing method by which the four entries of a matrix are coherently combined. In the current JMT, a sensitivity-enhanced scattering OCT and Doppler OCT are obtained from a coherent composite of the four entries.

The coherent composition of the matrix entries is based on the following mathematical model of the depth resolved OCT matrix $\mathbf{E}_{out}(z)$.

$$\mathbf{E}_{out}(z) = \begin{bmatrix} E^{(1)}_{out\,A}(z) & E^{(2)}_{out\,A}(z) \\ \\ E^{(1)}_{out\,B}(z) & E^{(2)}_{out\,B}(z) \end{bmatrix} \simeq \begin{bmatrix} E^{(1)}_{out\,A}(z) & e^{i\theta_1} E^{(1)}_{out\,A}(z) \\ \\ e^{i\theta_2} E^{(1)}_{out\,A}(z) & e^{i\theta_3} E^{(1)}_{out\,A}(z) \end{bmatrix} \tag{3.13}$$

where $\theta_{1,2,3}$ are depth-independent relative phase offsets with respect to the first entry, which account for spatial frequency difference, separate detection, and both of the frequency difference and separate detection, respectively. In addition to the relative phase offset, there are still depth-dependent phase differences among the matrix entries caused by the birefringence of the sample. However, the amount of the phase differences are so small compared to the relative phase offsets that I have assumed that the birefringence of the sample is negligible, as is assumed in conventional non-polarization sensitive OCT.

In our coherent composition method, $\theta_{1,2,3}$ are estimated as

$$\theta_1 \equiv \mathrm{Arg}\left[\sum_z E^{(2)}_{out\,A}(z)\; E^{(1)}_{out\,A}(z)^*\right] \tag{3.14}$$

$$\theta_2 \equiv \mathrm{Arg}\left[\sum_z E^{(1)}_{out\,B}(z)\; E^{(1)}_{out\,A}(z)^*\right] \tag{3.15}$$

$$\theta_3 \equiv \mathrm{Arg}\left[\sum_z E^{(2)}_{out\,B}(z)\; E^{(1)}_{out\,A}(z)^*\right] \tag{3.16}$$

where $\sum_z$ represents a summation of all pixels along the depth.

Using $\theta_{1,2,3}$, the coherent composition is defined as

$$\overline{E_{out}}(z) = \frac{1}{4}\left[E^{(1)}_{out\,A}(z) + e^{-i\theta_1} E^{(2)}_{out\,A}(z) + e^{-i\theta_2} E^{(1)}_{out\,B}(z) + e^{-i\theta_3} E^{(2)}_{out\,B}(z)\right]. \tag{3.17}$$

Since this composite signal is a coherent summation of four OCT signals, this method provides enhanced sensitivity and higher accuracy for Doppler phase shift measurement.

3.2.2.6 Doppler phase shift calculation

In our measurement protocol, the Doppler phase shift is defined as the phase difference between B-scans [54, 96], and for this purpose, a single location of a sample is scanned multiple times.

In general, a raw Doppler phase shift obtained from a living sample is expressed as

$$\Delta\phi(z) = \frac{4\pi\tau}{\lambda_c} n\nu_z(z) + \phi_b \tag{3.18}$$

where λ_c is the center wavelength, n is the refractive index of the sample, ν_z is the axial velocity of the flow of interest, and ϕ_b is a constant phase offset incurred by the bulk motion of the sample. τ is the time interval between two scans under Doppler calculation, and, in our protocol, is equivalent to the time interval of B-scans.

In the current JMT, the raw Doppler phase shift $\Delta\phi(j)$ is, in principle, defined using the coherently composite signals as

$$\Delta\phi(z, j) = \text{Arg}\left[\overline{E_{out}}(z, j+1)\overline{E_{out}}(z, j)^*\right] \tag{3.19}$$

where $\Delta\phi(j)$ is the Doppler phase shift of an A-line in the j-th B-scan against the corresponding A-line in the $(j+1)$-th B-scan. The bulk phase offset $\phi_b(j)$ is obtained by averaging the complex part of Eq. (3.19) as [97]

$$\phi_b(j) = \mathrm{Arg}\left[\sum_z \overline{E_{out}}(z, j+1)\overline{E_{out}}(z, j)^*\right] \tag{3.20}$$

where j denotes the index of the B-scan.

In the current measurement protocol, multiple (m) B-scans are obtained at the same location of a sample. Using these m B-scans and their bulk phase offsets, a sensitivity-enhanced Doppler signal is obtained as

$$\overline{\Delta\phi}(z, j) = \mathrm{Arg}\left[\sum_{j=m_0}^{m_0+m-2} \overline{E_{out}}(z, j+1)\overline{E_{out}}(z, j)^* \exp\left(-i\phi_b(j)\right) W(z, j)\right] \tag{3.21}$$

where m_0 is the starting B-scan index of the multiple B-scans, $W(z, j)$ is an intensity mask defined as

$$W(z, j) = \begin{cases} 1 & : \quad \overline{E_{out}}(z, j+1)\overline{E_{out}}(z, j)^* > \epsilon^2 \\ 0 & : \quad otherwise \end{cases} \tag{3.22}$$

and ϵ^2 is the intensity of the noise floor of an OCT image.

For the particular case of $m = 1$ in which only single B-scan is performed, the bulk-phase-offset-free Doppler phase shift can be defined as

$$\overline{\Delta\phi}(z, j) = \mathrm{Arg}\left[\overline{E_{out}}(z, j+1)\overline{E_{out}}(z, j)^* \exp\left(-i\phi_b(j)\right) W(z, j)\right]. \tag{3.23}$$

For displaying optical coherence angiography, the squared intensity of the Doppler phase shift $\left|\overline{\Delta\phi}(z, j)\right|^2$ is used, and this image is denoted as a power-of-Doppler-shift image.

3.2.2.7 Sensitivity-enhanced scattering OCT

A sensitivity-enhanced scattering OCT can be defined using the coherent composition of the matrix entries as $I(z,j) = \left|\overline{E_{out}}(z,j)\right|^2$.

Furthermore, with our particular measurement protocol, high-quality scattering OCT is obtained by complex-averaging m B-scans obtained at the same location on the sample as

$$\overline{I}\,(z,j) = \left| \sum_{j=m_0}^{m_0+m-1} \overline{E_{out}}(z,j) \exp\left(-i\Delta\varphi(z)^{(m_0,j)}\right) \right|^2 \tag{3.24}$$

where m_0 is the starting B-scan index of the multiple B-scans and $\Delta\varphi(z)^{(m_0,j)}$ is the global phase offset between matrices defined by Eq. (3.8) with substitutions of $\mathbf{M}^{(0)}$ by $\mathbf{E}_{out}\,(z,m_0)$ and $\mathbf{M}^{(j)}$ by $\mathbf{E}_{out}\,(z,j)$. I denote the high-quality scattering OCT obtained by Eq. (3.24) as global-phase-corrected sensitivity-enhanced scattering OCT.

Yet another type of sensitivity-enhanced scattering OCT is defined as

$$\overline{I}\,'(z,j) = \left| \sum_{j=m_0}^{m_0+m-1} \overline{E_{out}}(z,j) \exp\left(-i\phi_b'\,(m_0,j)\right) \right|^2 \tag{3.25}$$

where $\phi_b'\,(m_0,j)$ is the bulk phase offset between $\overline{E_{out}}(z,m_0)$ and $\overline{E_{out}}(z,j)$ defined as

$$\phi_b'(m_0,j) = \mathrm{Arg}\left[\sum_z \overline{E_{out}}(z,j)\overline{E_{out}}(z,m_0)^*\right]. \tag{3.26}$$

I denote this type of high-quality scattering OCT as bulk-phase-corrected sensitivity-enhanced scattering OCT.

As discussed later in Sect. 3.4.3, the global-phase-corrected and bulk-phase-corrected sensitivity-enhanced scattering OCTs provide different scattering contrast.

For cases shown in Sect. 3.3, global-phase-corrected sensitivity-enhanced scattering OCT is utilized.

3.3 Results

Table 3.1 shows specification summary of the current JMT system.

Table 3.1: Summary of advanced JMT specification.

Center wavelength	**Wavelength band width**	**Wavelength sweeping speed**	**Sample probing power**
1.06 μm	111 nm	100 kHz	1.15 mW
System sensitivity	**Sensitivity roll-off**	**Measurable depth-range**	**Depth resolution (in air)**
91.05 dB	-0.65 dB/mm	2.95 mm	8.5 μm

To demonstrate the clinical potential of the JMT, a posterior eye of a healthy subject and a geographic atrophy patient are measured. A transversal area of 4.5 mm (horizontal) $\times$ 4.5 mm (vertical) is scanned with 512 $\times$ 1024 A-scans in 6.6 seconds. In this measurement protocol, 4 B-scans are taken at a single location and used to create a sensitivity-enhanced Doppler signal (Eq. (3.21)) and global-phase-corrected sensitivity-enhanced scattering OCT (Eq. 3.24), where the Doppler time separation is 6.4 ms. Hence, the final number of B-scans after processing is 256.

For retardation imaging, the 4 B-scans are averaged by the adaptive Jones matrix averaging method described in Sect. 3.2.2.3 prior to calculating the eigenvalues. DOPU is also obtained from the averaged Jones matrix.

All protocols for measurement were approved by the Institution Review Board of University of Tsukuba. Written, informed consent was obtained prior

to measurement.

3.3.1 Jones matrix imaging of normal retina

The macular and optic nerve head (ONH) of the right eye of the healthy subject are scanned by the JMT. Figure 3.3(a) shows the OCT images taken by the two BPDs in the PD detection unit. An OCT signal obtained by a single BPD contains two OCT images at different depths, which corresponds to the two incident polarization states. The calibration signal exists at approximately the center of the depth field.

Figures 3.3(b)–3.3(e) represent the global-phase-corrected sensitivity-enhanced scattering OCT (b), phase retardation (c), DOPU images (d), and squared power of the Doppler phase shift (e). In the sensitivity-enhanced scattering OCT (Fig. 3.3(b)), retinal layers including the retinal nerve fibers layer (RNFL), ganglion cell layer (GCL), internal plexiform layer (IPL), inner nuclear layer (INL), outer plexiform layer (OPL), outer nuclear layer (ONL), external limiting membrane (ELM), junction of the inner and outer segments of the photoreceptor (IS/OS) and posterior tip of the outer segment (PT), retinal pigment epithelium (RPE), and choroid (CH) are visualized despite the relatively low sensitivity of the raw OCT image at 91.05 dB.

Among the layers, the ELM, IS/OS and PT layers exhibit hyper-scattering lines in the scattering OCT, while they show constant phase retardation in the retardation image (Fig. 3.3(c)). In the DOPU image (Fig. 3.3(d)), the RPE appears as a low DOPU band. In the power-of-Doppler-phase-shift image (Fig. 3.3(e)), a retinal vessel is clearly visible. The choroid vascular layer below the RPE is also densely visualized as exhibiting random phase shift signals.

Similar aspects also appear in the images of ONH as shown in Fig. 3.4. From

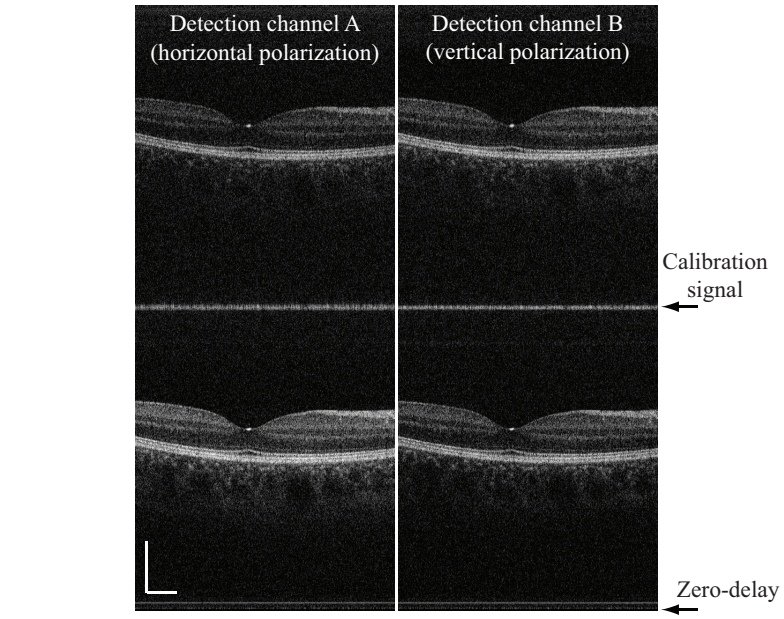

Figure 3.3: Jones matrix cross-sectional images of a normal macular. (a) Raw OCT intensity images detected by detection channels of A (horizontal polarization) and B (vertical polarization) of the PD detection unit. The lower and upper images correspond to the first and second polarization state, respectively. (b) Global-phase-corrected sensitivity-enhanced scattering OCT obtained by coherent composition. (c) A phase retardation image, (d) A DOPU image, (e) power-of-Doppler-phase-shift image (e). The scale bar represents 500 μm $\times$ 500 μm. (Source: **Ju *et al.*** *Advanced multi-contrast Jones matrix optical coherence tomography for Doppler and polarization sensitive imaging* [90])

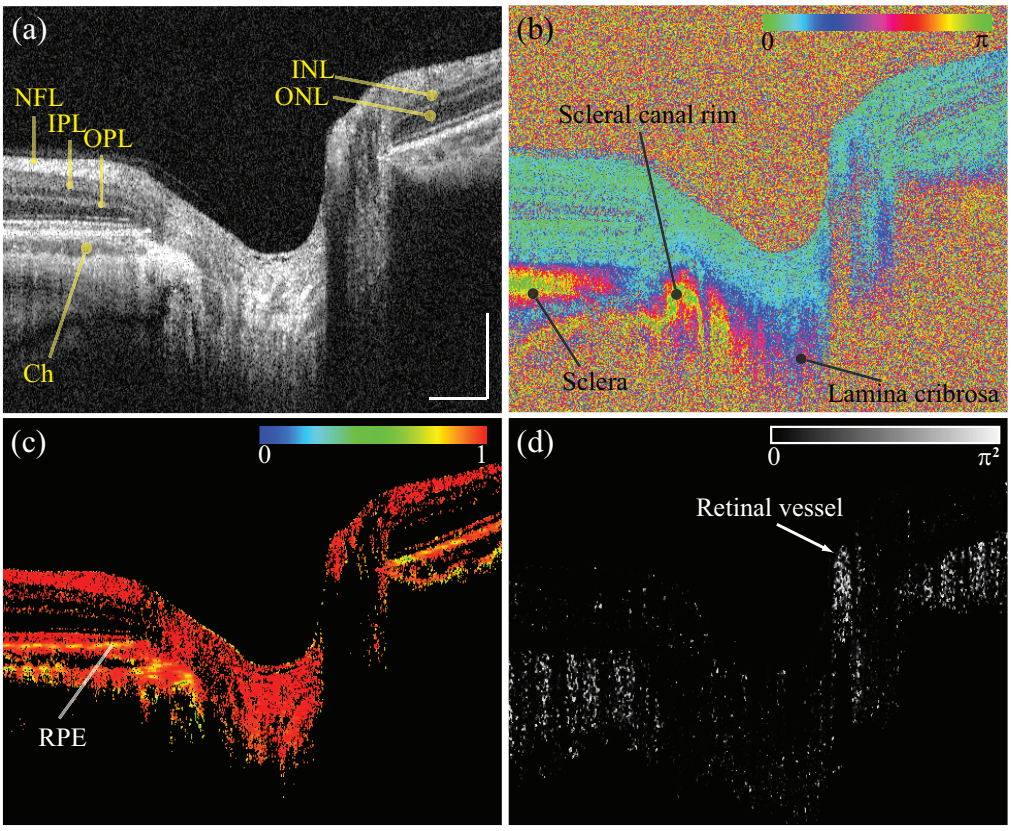

Figure 3.4: Jones matrix cross-sections of a normal ONH. (a) a global-phase-corrected sensitivity-enhanced scattering OCT, (b) phase retardation, (c) DOPU, and (d) power of Doppler phase shift. The scale bar represents 500 μm $\times$ 500 μm. (Source: **Ju *et al.*** *Advanced multi-contrast Jones matrix optical coherence tomography for Doppler and polarization sensitive imaging* [90])

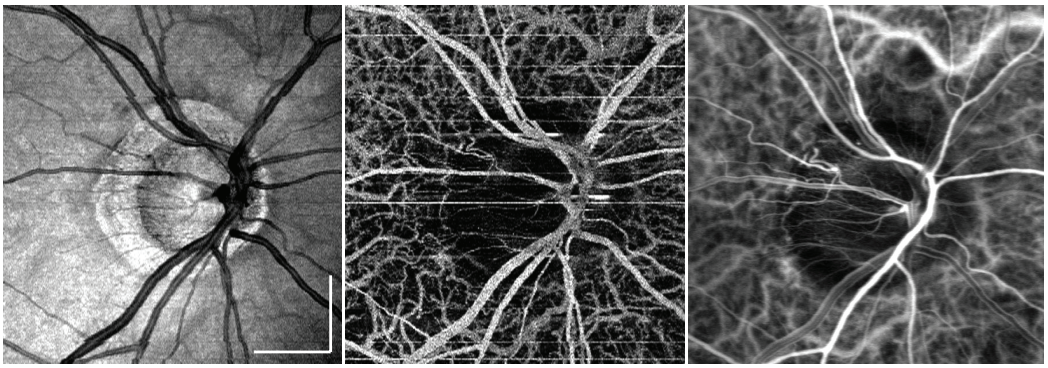

Figure 3.5: *En face* projection images of an ONH. (a) global-phase-corrected sensitivity-enhanced scattering OCT, (b) power of Doppler shift and (c) ICGA. The scale bar represents 1 mm × 1 mm. (Source: **Ju *et al.*** *Advanced multi-contrast Jones matrix optical coherence tomography for Doppler and polarization sensitive imaging* [90])

the phase retardation image of the ONH (Fig. 3.4(b)), the birefringence of lamina cribrosa and sclera are clearly visualized with rapidly varying phase retardation along the depth while they are not identified in the scattering OCT or the DOPU images. In particular, the scleral canal rim at the edge of the ONH exhibits strong birefringence.

In addition to the multi-contrast images, the *en face* projection of scattering OCT and the power of Doppler phase shift are shown in Fig. 3.5. From the *en face* scattering OCT (Fig. 3.5(a)), general posterior eye structures such as a myopic conus and retinal vessels are visualized. The choroidal vessels which are located deeper than the retinal vessels are not clearly visible. Conversely, the choroidal vessels are observed with enhanced contrast in the *en face* projection of the power of Doppler phase shift (Fig. 3.5(b)). The detail of blood vessels shown in the power-of-Doppler-phase-shift image is consistent with that of indocyanine green angiography (ICGA) shown in Fig. 3.5(c).

3.3.2 Geographic atrophy

As a pathological subject study, an eye of a geographic atrophy (GA) patient (72-year-old Japanese male) is also examined to evaluate the clinical performance of the JMT system.

GA is an advanced form of dry age-related macular degeneration (AMD), and here atrophy refers to the degeneration of the RPE cells. GA is usually defined by a sharply circumscribed area of pigment epithelial atrophy through which choroidal vessels can be seen [98, 99]. The continent-shaped area appears different from the surrounding retina because of the loss of the pigmented RPE in the color fundus and fundus auto-fluorescence (FAF) images as shown in Figs. 3.6(a) and 3.6(b). The area of GA looks whiter than the surrounding area in the color fundus and appears dark in the FAF image. The enhanced visibility of the choroidal vasculature in the GA region is found in the scattering OCT as shown in Fig. 3.6(c), while the choroidal vasculature in this region is more clearly visible in the power-of-Doppler-shift image as shown in Fig. 3.6(d).

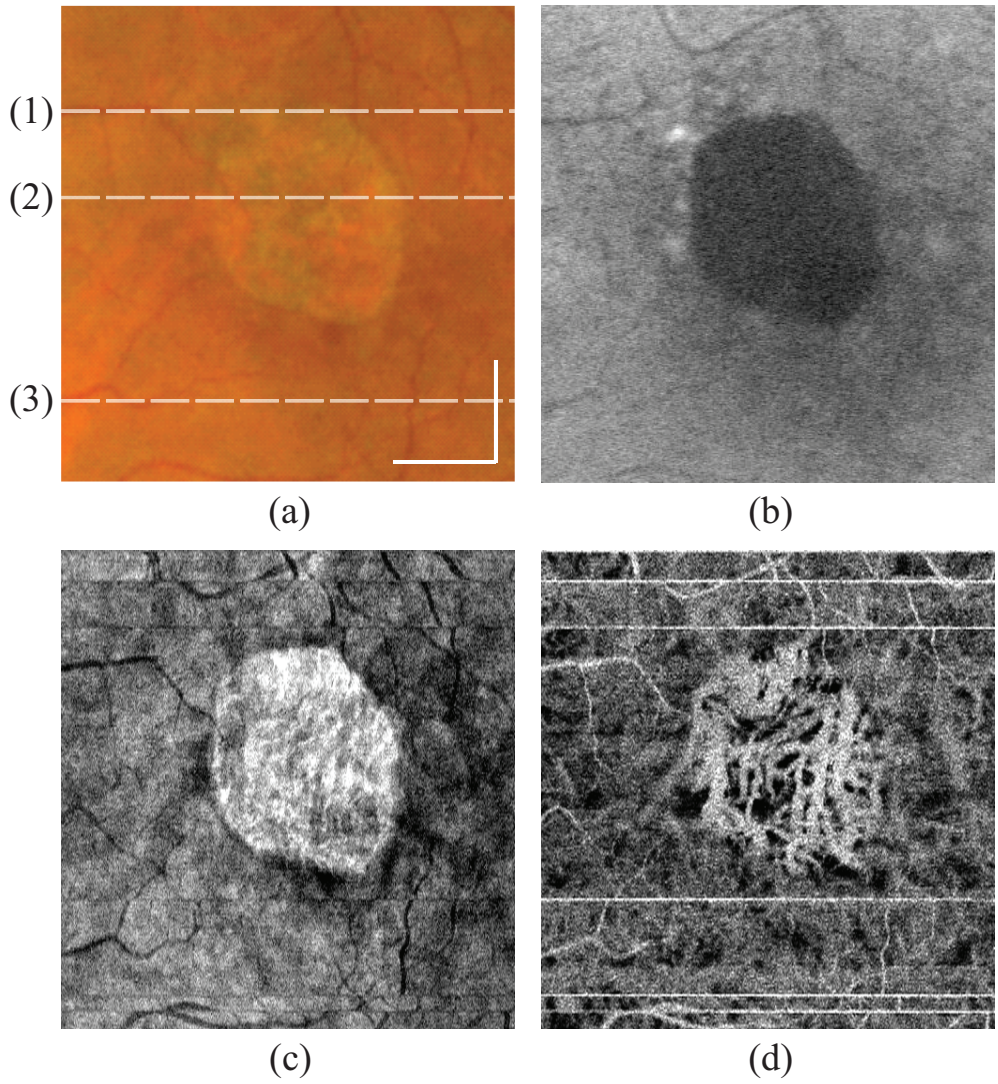

Figure 3.6: *In vivo* measurement images of a GA patient; (a) fundus photograph, (b) fundus auto-fluorescence image, *en face* projection images of (c) global-phase-corrected sensitivity-enhanced scattering intensity, and (d) Doppler shift power. The scale bar indicates 1 mm × 1 mm. (Source: **Ju *et al.*** *Advanced multi-contrast Jones matrix optical coherence tomography for Doppler and polarization sensitive imaging* [90])

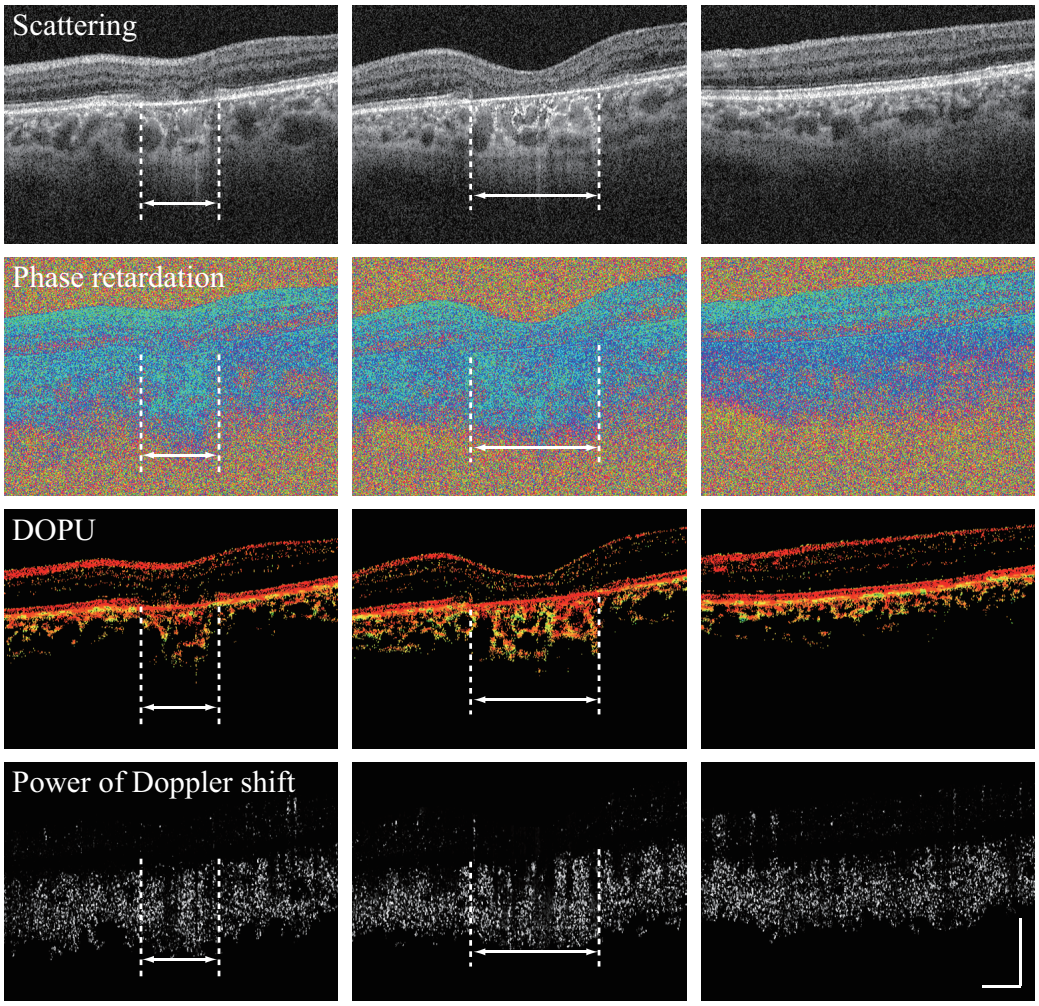

Figure 3.7: Multi-contrast Jones matrix cross-section images of geographic atrophy. The first to the fourth rows correspond to coherent composite scattering images, phase retardation images, DOPU images, and power-of-Doppler-shift images, respectively. Columns (1)–(3) were obtained at the location indicated in Fig. 3.6(a). Arrows indicate the atrophic region. The scale bar indicates 500 μm $\times$ 500 μm. (Source: **Ju *et al.*** *Advanced multi-contrast Jones matrix optical coherence tomography for Doppler and polarization sensitive imaging* [90])

Typically, a histopathologic section of GA shows the thinning or absence of RPE, closure of the choriocapillaris, and degeneration of the overlying photoreceptors [98]. For comparison between the areas with and without GA, three representative multi-contrast B-scan images are shown in Fig. 3.7. Figures 3.7(1)–3.7(3) correspond to the horizontal lines (1)–(3) in Fig. 3.6(a), which represent cross sections of the near-edge, middle, and area outside of the GA region, respectively.

As indicated by the dashed lines, the atrophic regions appear in the scattering OCT as regions without RPE. The absence of RPE is more clearly visualized by DOPU images.

It is also noteworthy that some part of the choroid shows low DOPU values. Since melanin exists in the choroid [100], this appearance would be associated with choroidal melanin concentration.

3.4 Discussion

3.4.1 Phase stability analysis

In this section, the performance of the spectral shift correction for enhancing phase stability is examined quantitatively and qualitatively. For the phase stability test, I measure a static mirror at different depths without transversal scanning and analyzed the stability of the phase difference between adjacent A-lines. At each depth, 1024 A-lines are measured.

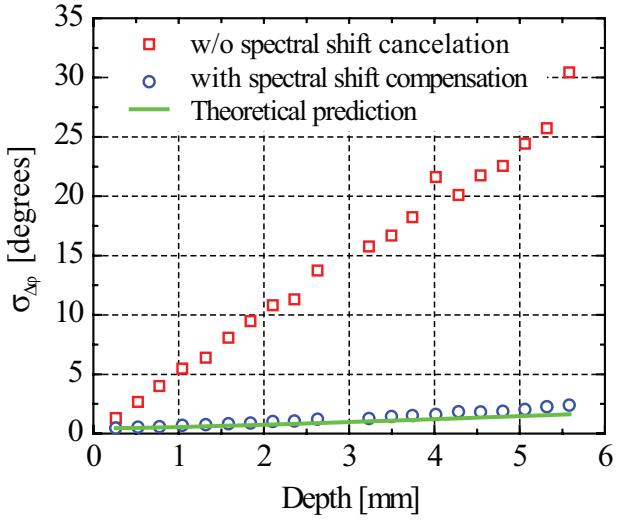

Figure 3.8: Measured phase noise with (○) and without (□) the spectral shift correction. The green line indicates the theoretical prediction. (Source: **Ju *et al.*** *Advanced multi-contrast Jones matrix optical coherence tomography for Doppler and polarization sensitive imaging* [90])

Figure 3.8 shows the standard deviation of the phase differences with and without spectral shift cancellation. The green line in Fig. 3.8 is the theoretical phase noise limit that represents the maximum phase stability (minimum phase noise) of the system and can be described by [93],

$$\sigma_{\Delta\phi} = \sqrt{\left(\frac{1}{SNR_s}\right) + \left(\frac{z_s}{z_c}\right)^2 \left(\frac{1}{SNR_c}\right)} \tag{3.27}$$

where $\sigma_{\Delta\phi}$ is the standard deviation of the phase difference, SNR_s and SNR_c are the SNRs of the sample, in this case a mirror, and the calibration signal. z_s and z_c are the depth positions of the sample and the calibration signal, respectively.

The result verifies enhancement of phase stability after applying the spectral shift correction. Here SNR_s is 42 dB, the roll-off measured at the depth range of 0.3 to 5.6 mm is -1.06 dB/mm, and SNR_c is 38 dB. For SNR_s of 42 dB, $\sigma_{\Delta\phi}$ is measured to be 0.47 degree (8.16 mrad), while its theoretical prediction is 0.46

degree (8.02 mrad). This phase stability is comparable to previously published swept-source OCT [94]. Although recognizable difference between measured phase noise of 2.38 degree (41.58 mrad) and the theoretical prediction of 1.62 degree (28.34 mrad) exists at a depth of 5.58 mm, where the SNR_s is 36 dB, it is still better than the result reported by Baumann *et al.* [45] (97 mrad at 100 kHz for the SNR_s of 35 dB).

In addition to the quantitative analysis, the impact of the spectral shift correction on the fixed-pattern noise (FPN) elimination is investigated qualitatively. The FPN consists of interference signals from undesired reflection in the interferometer from the light source and cannot be removed unless the OCT signals become stabilized in phase, and hence is a good indicator of the phase stability of the OCT.

As shown in Fig. 3.9(a), severe FPN can be seen if an FPN elimination process is not applied. When a median estimator-based FPN elimination process [101] is applied, significant FPN still exists if spectral shift cancellation is not simultaneously applied, as shown in Fig. 3.9(b). The combination of the spectral shift correction with 1/16 pixel resolution and the median estimator-based FPN elimination shows elimination of almost all of the FPN, as shown in Fig. 3.9(d).

It is noteworthy that, without the zero-padding process required for the sub-pixel correction of the spectral shift, the FPN becomes even stronger than it is without spectral shift cancellation, as shown in Fig. 3.9(c). Particularly, spectral shift correction with single-pixel resolution worsenes the phase stability. Therefore, as mentioned in Sect. 3.2.2.1, a proper amount of zero-padding is essential.

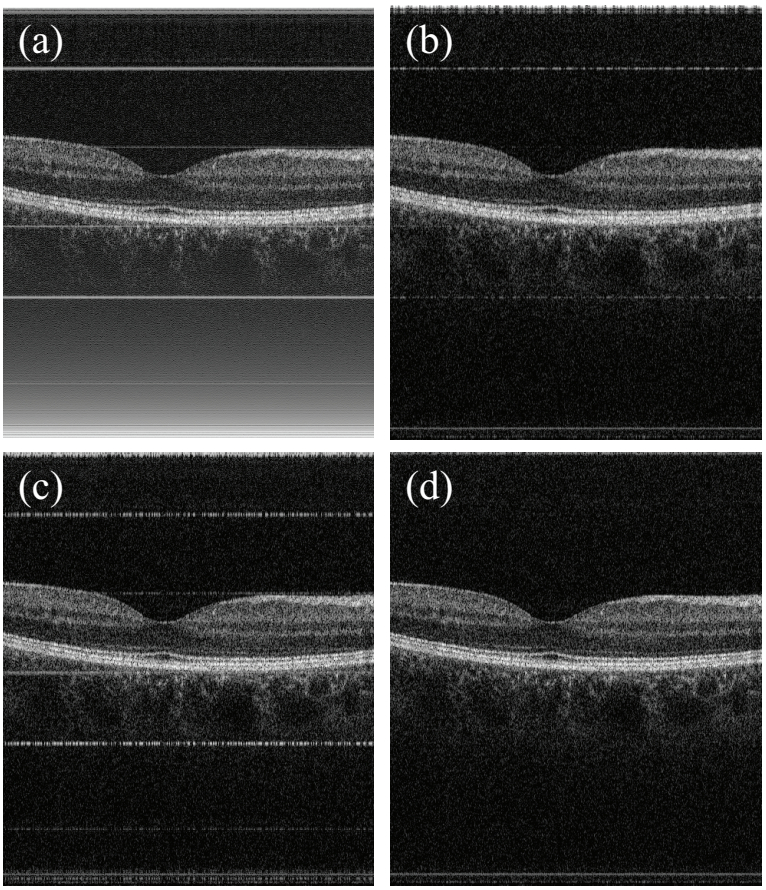

Figure 3.9: OCT images of the macular of a healthy volunteer. (a) A raw image without FPN removal, (b) FPN removal without spectral shift cancellation, (c) with spectral shift cancellation and FPN removal, but no zero-padding applied. (d) FPN removal was performed after spectral shift cancellation with 1/16 pixel resolution. (Source: **Ju *et al.*** *Advanced multi-contrast Jones matrix optical coherence tomography for Doppler and polarization sensitive imaging* [90])

3.4.2 Advantages of the phase stabilization process

The proposed phase stabilization process is based on the cross-correlation of the calibration signals that originated from general characteristics of the PBS and systematic features of the current JMT system. Because of the origin and location of the calibration signal, this method has several advantages over other methods recently reported [45, 94].

First, no specific optical component that extracts light from the interferometer, such as a coupler, is required. And hence there is no additional optical loss. This also makes the system simple and cost-efficient. Second, the calibration signal does not reduce the depth measurement range, because it appears at exactly the zero-delay point of the OCT image corresponding to the delayed polarization component. In addition, the depth location of the calibration signal does not depend on the path length of the calibration mirror arm. This further eases the optical and mechanical design of the OCT scanner, especially for applications in which the reference path length frequently alters to adjust to that of a sample arm, such as in posterior eye imaging. It should be noted that the path length difference between the 80:20 coupler to the calibration mirror and the coupler to the retina should be more than the full depth measurement range that covers the depth ranges of input state-1 and -2. Otherwise the interference signal between the light from calibration mirror and the reference appears as an FPN and overlaps with the OCT image.

In comparison to a fully numerical method [50] used in the previous JMT [88], our overall processes are simplified and the performance is stable. In the previous numerical process, OCT signal generated by a reference beam located at the region close to the zero delay was used for rough estimation of the spectral shift amount. In addition, a weighted linear iteration fitting algorithm, fully described in Sect. 2.3

of Ref. [50], was additionally applied to correct the residual spectral shift. On the other hand, our current stabilization method only requires to calculate the cross-correlation between the reference and test calibration signals.

It would be fair to declare the relatively long computational time of the phase stabilization process. The current implementation is in LabVIEW 2011 on a 64-bit Windows 7 PC with an Intel core i7 950 3.07GHz CPU, and it takes around 27 minutes for a single volume consisting of 512 $\times$ 1024 A-scans. Since the phase stabilizations of each A-line are independent to each other, the process can be highly parallelized by using a GPU or multiple CPU cores. So the possible parallel processing and/or further optimized algorithm would enable sufficiently high-speed phase stabilization.

Finally, the high accuracy and effectiveness of the proposed method, as verified in the previous sections, provides a high reliability to the system for clinical applications.

3.4.3 Global-phase-corrected and bulk-phase-corrected sensitivity-enhanced scattering OCT

The global- and bulk- phase-corrected sensitivity-enhanced scattering OCTs defined in Sect. 3.2.2.7 provide different scattering contrasts.

Figures 3.10(a) and 3.10(b) are the examples of sensitivity-enhanced B-scans of the GA eye presented in Sect. 3.3.2. Figure 3.10(a) is obtained with a global-phase correction while Fig. 3.10(b) is obtained with a bulk-phase correction. In the global-phase-corrected image, the lumens of large choroidal vessels appear with more-hyper-scattering than those in the bulk-phase-corrected image.

This difference is explained by the difference in the phase estimation meth-

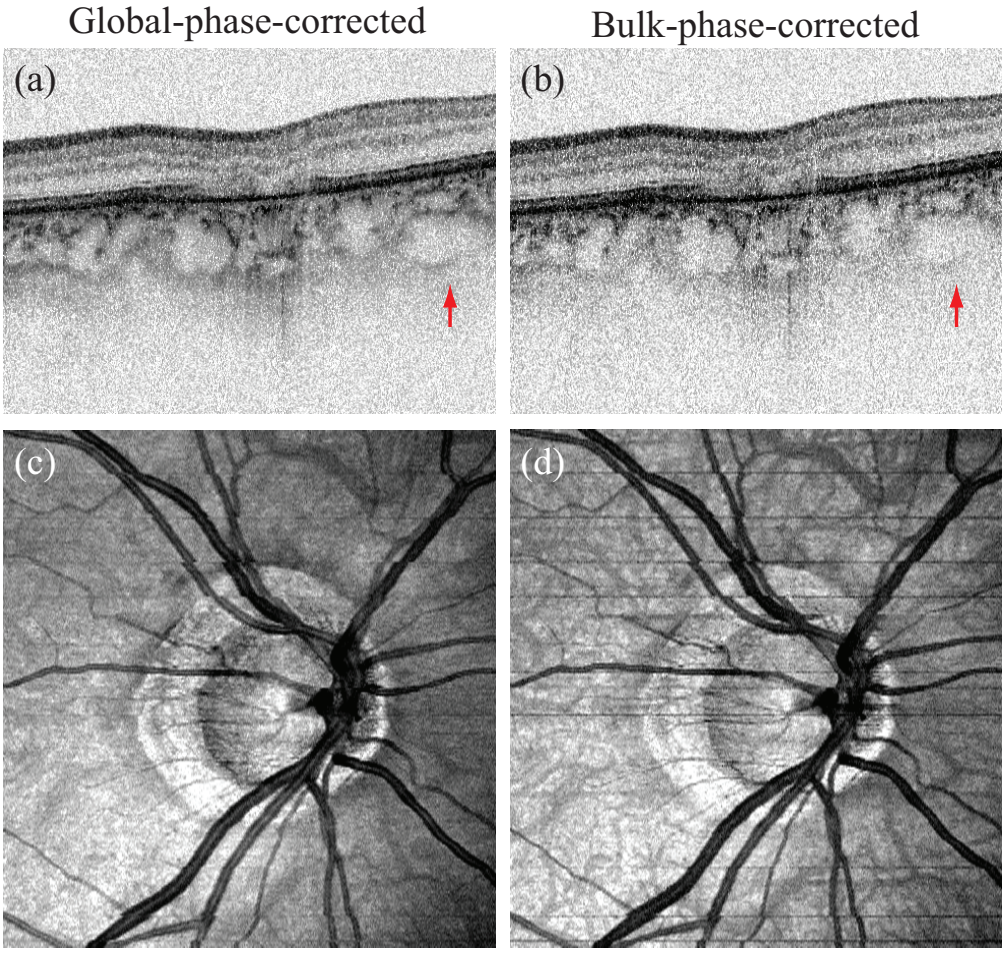

Figure 3.10: The comparison between global- and bulk- phase-corrected sensitivity-enhanced scattering OCTs. (a) and (c) are a B-scan and *en face* projection of sensitivity-enhanced OCTs with global-phase correction, and (b) and (d) are those with bulk-phase correction. (Source: **Ju *et al.*** *Advanced multi-contrast Jones matrix optical coherence tomography for Doppler and polarization sensitive imaging* [90])

ods. Namely, the global phase is estimated in point-wise, while the bulk phase is estimated in A-line-wise. Therefore the bulk-phase correction corrects a constant phase offset of each A-line, where the constant phase offset, in general, is occurred by a bulk motion of the sample and is a phase offset at the region of a static tissue. And hence, the bulk-phase correction can enhance the OCT signal at the static tissue but cannot enhance the OCT signal at regions with a localized motion, such as a region with blood flow.

On the other hand, global-phase correction corrects any phase offset including those occurred by a bulk motion and also by a localized motion. As a result, the global-phase correction enhances the OCT signals both at the static tissue and at the region with blood flow. This difference between the two phase correction methods result in the different contrasts of choroidal vessels.

Similarly, the global-phase correction also corrects phase offset occurred by shadowing of Doppler shift of the blood flow. This results in more hyper scattering signals at the region beneath large choroidal vessels in the global-phase-corrected image than the bulk-phase-corrected image as exemplified by an arrow in Figs. 3.10(a) and 3.10(b).

Because the signal degradation occurred by the blood flow is larger in the bulk-phase-corrected image, the choroidal vessels appear more clearly in the *en face* projection of bulk-phase-corrected sensitivity-enhanced scattering OCT than that of global-phase-corrected OCT. Figures 3.10(c) and 3.10(d) show an ONH of the subject presented in Sect. 3.3.1 obtained with a global-phase correction and bulk-phase correction, respectively. The bulk-phase-corrected image reveals finer details of the choroidal vessels with higher contrast than the global-phase-corrected image. On the other hand, the scattering property of the tissue would be more

easily evaluated with the global-phase-corrected image. Note that Figs. 3.10(c) and 3.10(d) are displayed with a gray-color-map while Figs. 3.10(a) and 3.10(b) are displayed with an inverted-gray-color-map.

Since the phase-offset occurred by quick eye motion reduces the signal intensity of the sensitivity-enhanced OCT, the quick eye motion creates a dark horizontal line artifact in the *en face* projection as shown in Fig. 3.10(d). As exemplified by the vessel contrast, the global-phase correction has higher ability to correct the phase-offset than the bulk-phase correction. And hence the contrast of the dark horizontal line artifacts in the *en face* image created with the global-phase correction (Fig. 3.10(c)) is significantly less than that with bulk-phase correction (Fig. 3.10(d)).

3.4.4 Effect of practical factors in JMT measurement

In this discussion, fundamental robustness of the JMT method is provided. As discussed in Sect. 2.1, the relationship between incident and output light in an ideal JMT is described by Eq. (2.3).

In a practical system, several additional factors should be considered. By accounting for these factors and by substituting $\mathbf{J}_{all}(z) = \mathbf{J}_{out}\mathbf{J}_s(z)\mathbf{J}_{in}$, Eq. (2.3) is modified to

$$\mathbf{E}_{out}(z) = \eta\, \mathbf{X}'\, \mathbf{R}\, \rho\, \mathbf{J}_{out}\, \mathbf{J}_s(z)\, \mathbf{J}_{in}\, \mathbf{X}\; f\left(\mathbf{X}\, \mathbf{E}_{in}\;\right) \tag{3.28}$$

where $\mathbf{X}$ is a matrix representing the imperfection of the PBS in the polarization delay unit. As it is used to generate the calibration signal, there is a significant amount of polarization cross-talk in the PBS. The off-diagonal entries of $\mathbf{X}$ account for the cross-talk and the diagonal entries represent the transmittance and reflectance of the horizontally and vertically polarized light. Here, $f(\,)$ is a function which represents the delay between two incident polarization states generated by the polarization

delay unit. In Eq. (3.28), $\mathbf{R}$ represents interference with the reference beams and is $\mathbf{R} = \begin{bmatrix} H^*_{ref} & 0; & 0 & V^*_{ref} \end{bmatrix}$ where H^*_{ref} and V^*_{ref} are the complex conjugates of the field amplitudes of the reference beam with horizontal and vertical polarization states. In addition, ρ is a rotation matrix representing the relative rotation between the polarization delay unit and the PD detection unit. $\mathbf{X}'$ represents the imperfection of the PBS in the PD detection unit, similar to that of the polarization delay unit $\mathbf{X}$. Finally, η represents the detection efficiency of the two BPDs in the polarization delay unit as $\eta = [\eta_A \;\; 0; \;\; 0 \;\; \eta_B]$, where η_A and η_B are the detection efficiencies of the two BPDs.

Although $\mathbf{E}_{out}(z)$ is affected, these practical factors do not affect the phase retardation measurement. In JMT, a similar matrix of $\mathbf{J}_s(z)$ is obtained by Eq. (2.6). By substituting Eq. (3.28) for Eq. (2.6), it is found that

$$\mathbf{E}_{out}(z)\mathbf{E}_{out}(z_0)^{-1} = \eta\,\mathbf{X}'\,\mathbf{R}\,\rho\,\mathbf{J}_{out}\,\mathbf{J}_s(z)\,\mathbf{J}_{out}^{-1}\,\rho^{-1}\,\mathbf{R}^{-1}\,\mathbf{X}'^{-1}\,\eta^{-1}. \tag{3.29}$$

It is evident that the right-hand side of this equation retains its similarity to $\mathbf{J}_s(z)$. Hence all the practical factors discussed in this section do not significantly affect the Jones matrix measurement.

3.5 Summary

In this chapter, an advance version of JMT system based on a passive polarization delay at 1-μm wavelength was presented. Because of the accurate spectral shift correction method based on cross-correlation of the calibration signal originated from the general characteristics of PBS, I achieved a highly phase-stabilized system.

New JMT algorithms which integrated polarization measurement, Doppler

measurement, and scattering measurement were also presented. Owing to these new algorithms and high phase stability, highly-sensitive Doppler OCT and sensitivity-enhanced scattering OCT were demonstrated.

In vivo measurements of a healthy and pathologic eye were demonstrated. The Doppler image revealed small vessels invisible in the OCT intensity image, while the phase retardation and DOPU image demonstrated tissue-selective visualization of the human retina and choroid. These results indicated the clinical utility of the JMT.

Chapter 4

Volumetric human meibomian gland investigation*

As a new clinical application of JMT, human meibomian gland imaging is performed using a conventional EOM-based JMT system. For Jones matrix analysis, the advanced JMT algorithms introduced in Chapter 3 are employed.

4.1 Introduction

Human meibomian glands (MGs) are large secretory lipid-excreting glands embedded in the tarsal plate with approximately 31 and 26 individual glands in the upper and lower eyelid, respectively [102]. Each MG is comprised of multiple acini that are circularly arranged around a common central duct and connected to it by short ductle. A single acinus that have an elongated or spherical shape of about 150 μm to

*This chapter has been mainly adopted from the following publication:
M. J. Ju, J. G. Shin, S. Hoshi, Y. Yasuno, B. H. Lee, S. Tang, and T. J. Eom, "Three-dimensional volumetric human meibomian gland investigation using polarization-sensitive optical coherence tomography," J. Biomed. Opt. **19**, 30503 (2014)

200 μm diameter is completely filled with secretory cells, termed meibocytes [103]. The meibocytes, located more toward the center of the acinus, are found to progressively accumulate lipids in the cytoplasm while it appears increasely foamy and pale in conventional histology processed after extracting lipid contents. Meibum is the oily secretory product from whole cell contents in the acinus and the main component of the superficial layer of the tear film which as important functions such as formation of a hydrophobic barrier to prevent tear overflow onto the lids [103] and stabilization of tear film by lowering surface tension [104]. Importantly, the meibum may also provide a barrier function to prevent entry of bacteria into the tear film and inhibit entry of undesirable sebum at the lid margin [103].

As increasing interest of MG functions, several imaging modalities have been developed in order to investigate and diagnose MG related diseases (e.g., meibomian gland dysfunction (MGD)) by visualizing MG structure. In recent study by William Ngo *et al.* [105], functionalities and characteristics of several MG visualization methods such as lid transillumination, video and non-contact meibography, confocal microscopy, ultrasound, and OCT were provided. Among them, OCT, which is a well-known technique for creating a cross-sectional and three-dimensional structure of biological tissue in a non-invasive way and with high-contrast [1], has been utilized to acquire volumetric MG structure with ultra-high resolution of 3 μm in axial and 10 μm in lateral [106]. By employing the ultrahigh resolution OCT system, a few ductles and acini were observed. However, because of the limited imaging range due to such high resolution, it seems to be difficult to extract the general MG structure consisting of multiple acini, and to assess MG dropout (disappearance of the glandular tissue inside the tarsal plate).

In this chapter, Jones matrix tomography (JMT) [56, 83] based on polar-

ization modulation along the wavelength scan described in Sect. 2.2 is employed for volumetric investigation of MG structure. By scanning the everted upper eyelid using the JMT, internal structure of the inner lid is obtained with scattering contrast. In addition, with the help of the polarization contrast, MG structure is exclusively visualized after segmenting out the conjunctiva layer located above the MGs. Furthermore, I show the measurement results of different age subjects, which demonstrate the utility of the system for clinical ophthalmology.

4.2 Methods

4.2.1 System

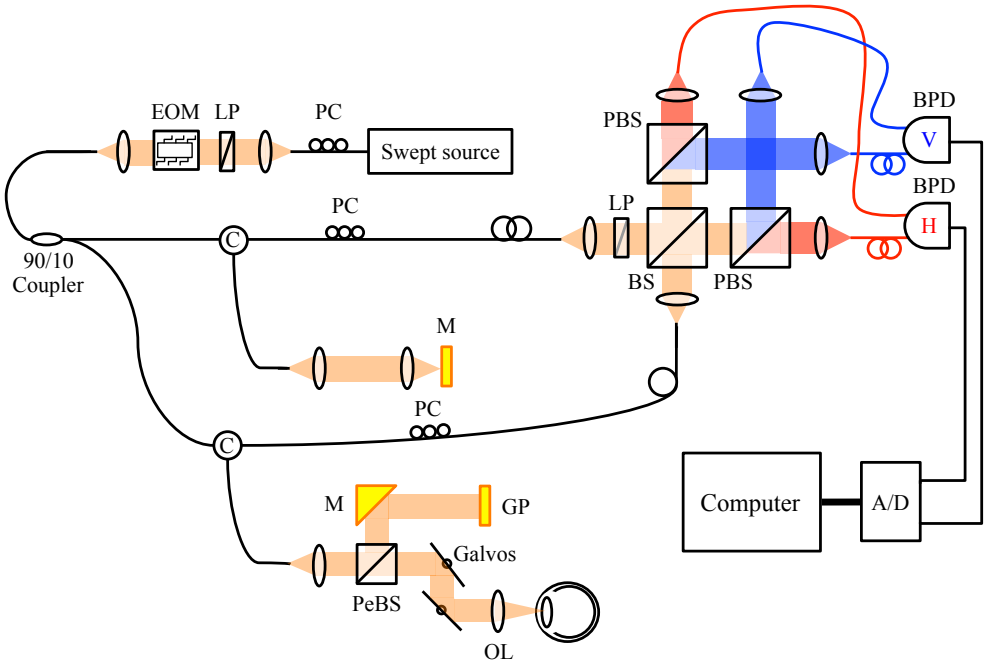

Figure 4.1: Schematic diagram of EOM-based JMT system. EOM: electro-optic modulator, LP: linear polarizer, PC: polarization controller, M: mirror, C: circulator, GP: glass plate, OL: objective lens, BS: beam splitter, PBS: polarizing beam splitter, PeBS: pellicle beam splitter, BPD: balanced photo-detector.

The system has been previously developed by Lim *et al.* [56]. Here I briefly describe the system configuration. Figure 4.1 shows the schematic of JMT based on polarization modulation along the wavelength scan, whose technical concept and detail are described in Sect. 2.2 and Refs. [56, 83], respectively. This JMT, based on a high speed wavelength sweeping laser with 30 kHz sweeping rate and a center wavelength of 1.31 μm, consists of fiber based Mach-Zehnder interferometer, electro-optic modulator for continuous polarization modulation of the light source along the wavelength sweeping, and two balanced photo-detectors used for polarization diversity (PD) detection of both vertically polarized and horizontally polarized spectral interferograms.

An EOM (PC-B3-00-SFAP-SFA-130-UL; EOspace, WA) is employed for continuous polarization modulation of the light source. After the modulation, the light source is split by a single mode fiber coupler (10202A-90-FC; Thorlabs, NJ), and then directed to a sample arm and a reference arm with a ratio of 90:10. The reference light is reflected by a mirror and directed to PD detection arm. In the sample arm, after splitting by a pellicle beam splitter (CM1-BP5; Thorlabs), 92 % of the light illuminates the sample and 8 % of the light is directed to a phase reference glass plate for stabilizing the phase of OCT signal among A-scans. More detail about the stabilization process can be found from the Ref. [83]. The back-scattered light from the sample combines with the light reflected from the reference mirror at the non-polarization beam splitter in the PD detection. Finally, vertically and horizontally polarized signals are separated by the two polarization beam splitters, and then interference fringes are detected by the two balanced photo-detectors (BPD-200; Santec Corp.).

The probing power is measured to be 2.8 mW, which is below the laser safety

limits defined by ANSI [34]. The imaging depth resolution and range are measured to be around 12.7 μm (in air) and 5.3 mm, respectively. The sensitivity of the system is measured to be 98 dB at a depth of 141 μm from the zero-delay, and the sensitivity roll-off is -1.3 dB/mm.

In this JMT system, by employing sinusoidal modulation on the incident polarization and PD detection, interference signals of two different polarization states are detected simultaneously. From the obtained interference signals, four OCT signals corresponding to the Jones matrix elements are extracted as described in the Ref. [83]. Finally, this JMT system provides the Jones matrix tomography in which each pixel represents a Jones matrix of the corresponding point of the sample. Table 4.1 shows the specification summary of EOM-based JMT system employed in this chapter.

Table 4.1: Summary of EOM-based JMT specification.

Center wavelength	**Wavelength band width**	**Wavelength sweeping speed**	**Sample probing power**
1.31 μm	100 nm	30 kHz	2.8 mW
System sensitivity	**Sensitivity roll-off**	**Measurable depth-range**	**Depth resolution (in air)**
98 dB	-1.3 dB/mm	5.3 mm	12.7 μm

4.3 Results

4.3.1 Meibomian gland segmentation

From Jones matrix measurement, phase retardation and DOPU images are simultaneously acquired as well as scattering OCT image. Among them, the retardation and DOPU derived by the methods described in Sect. 3.2.2 are utilized for investigation of polarization properties of the MG and its surrounding tissue. In our practical implementation, a kernel size of 5 pixels (horizontal) $\times$ 3 pixels (vertical) (97.6 μm $\times$ 25.8 μm) is used for both of the Jones matrix averaging and DOPU calculation.

Figure 4.2 shows the representative cross-sectional JMT images (Figs. 4.2(b)–4.2(d)] obtained within the red window in the meibography image (Fig. 4.2(a)). The meibography image is captured by IR-CCD camera and exhibits a wide range of gland morphology. From the cross-sectional scattering OCT image (Fig. 4.2(b)), the conjunctiva layer and the MGs can be roughly identified by the difference in the intensity contrast. The conjunctiva layer appearing as hyperscattering in the OCT image shows nearly a constant value in the phase retardation image (Fig. 4.2(c)) and a value close to 1 in the DOPU image (Fig. 4.2(d)). In contrast with the conjunctiva layer, nonconstant retardation and relatively lower DOPU quantities are observed from the MGs, as shown in Figs. 4.2(c) and 4.2(d).

In this study, histogram-based polarization contrast analysis is performed for acquiring the criteria to make a discrimination between the conjunctiva layer and the MGs. Based on the criteria, it can be expected to achieve more reliable volumetric MG structure investigation. The representative regions within the conjunctiva layer and the acini ($\mathbf{R}_{\mathrm{conj}}$ and $\mathbf{R}_{\mathrm{acini}}$) are first selected as shown in Figs. 4.2(c) and 4.2(d).

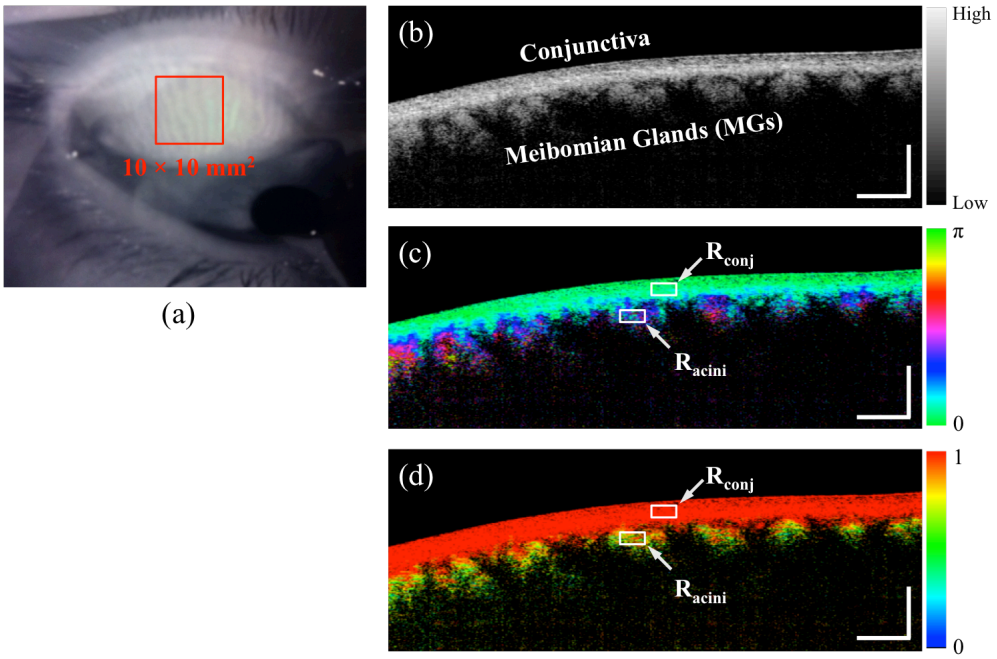

Figure 4.2: Meibography and Jones matrix tomography cross-sectional images. (a) Meibography image and (b)–(d) Jones matrix tomography cross-sectional images: (b) scattering intensity OCT image, (c) phase retardation image, and (d) DOPU image. The scale bar represents 1 mm × 1 mm. (Source: **Ju *et al.*** *Three-dimensional volumetric human meibomian gland investigation using polarization-sensitive optical coherence tomography* [107])

The histograms of the phase retardation and the DOPU quantities within the given areas are then obtained as shown in Fig. 4.3.

In the $\mathbf{R}_{\text{conj}}$, polarization-maintaining property of the layer is evident from the narrow width of the retardation histogram (Fig. 4.3(a)) with the standard deviation (SD) of 0.07 (in radian). On the contrary, in the case of the $\mathbf{R}_{\text{acini}}$ (Fig. 4.3(b)), a broad-phase retardation distribution represented by the histogram with the SD of 0.33 (in radian) is observed. Figures 4.3(c) and 4.3(d) show the DOPU histograms of the $\mathbf{R}_{\text{conj}}$ and the $\mathbf{R}_{\text{acini}}$, in which the difference between the conjunctiva layer and the MGs is more clearly identified. Most pixels within the $\mathbf{R}_{\text{conj}}$ have the DOPU quantities higher than 0.95, whereas the DOPU values from the $\mathbf{R}_{\text{acini}}$ spread out over the DOPU range below the value of 0.95. This implies that the spatial uniformity of polarization within the conjunctiva layer is very high as compared with the one in the acini. As a result, the DOPU value of 0.95 is empirically set as the threshold for MG structure extraction.

In order to extract MG structure from the scattering OCT image, pixels with DOPU value over 0.95 are segmented as the conjunctiva layer from the DOPU image and then the segmented layer is applied onto the OCT intensity image as a binary mask. Figure 4.4(a) shows a representative *en face* OCT intensity image selected from the volume measurement result. In the *en face* image, the conjunctiva layer is revealed by a hyper-scattering band while MGs composed of several granular-shaped acini appear with relatively lower intensity. Figures 4.4(b) and 4.4(c) show the segmented conjunctiva layer from the DOPU image and the extracted MG structure from the intensity image after applying the binary mask corresponding to the conjunctiva layer.

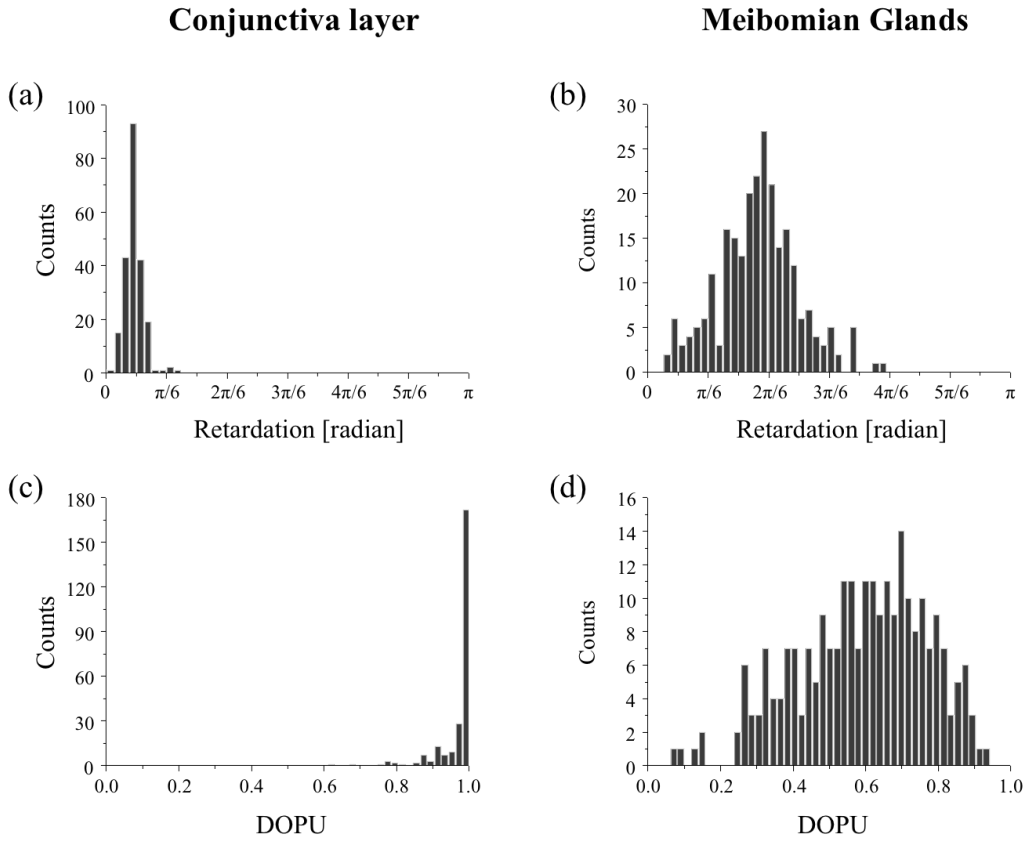

Figure 4.3: Histograms of retardation and degree of polarization uniformity (DOPU). (a, c) Data from $\mathbf{R}_{\text{conj}}$ and (b, d) data from $\mathbf{R}_{\text{acini}}$ in Figs. 4.2(c) and 4.2(d). (Source: **Ju *et al.*** *Three-dimensional volumetric human meibomian gland investigation using polarization-sensitive optical coherence tomography* [107])

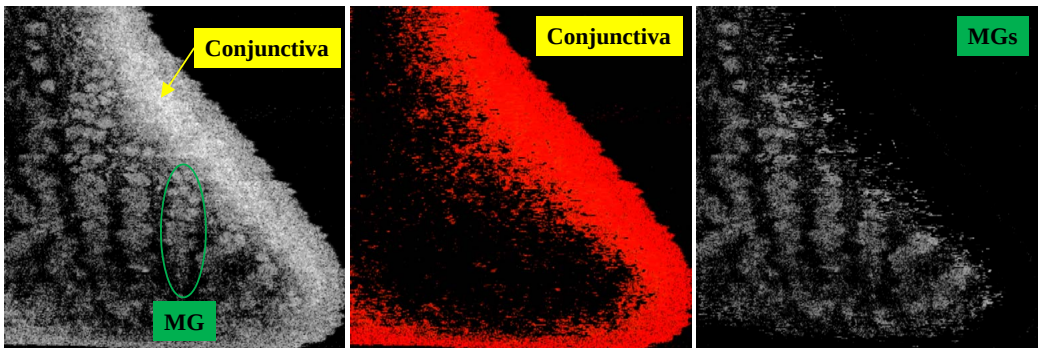

Figure 4.4: *En face* sliced MG segmentation result. (a) scattering intensity OCT image, (b) segmented conjunctiva layer from DOPU image, and (c) extracted MGs image from (a)

4.3.2 3-D volumetric MG visualization

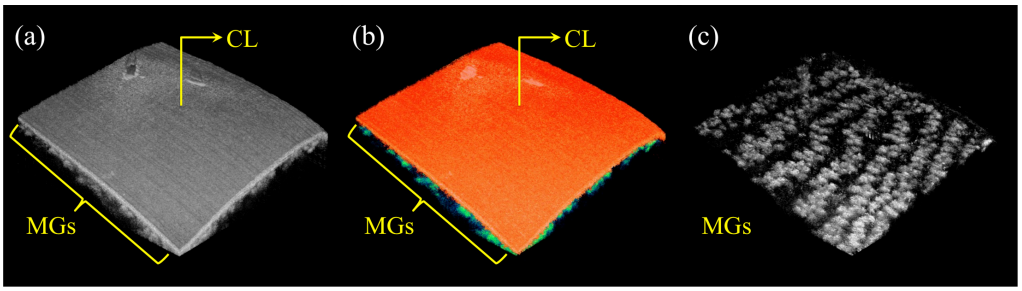

Figure 4.5: 3D volume MG segmentation result. (a) original scattering intensity image, (b) classification-processed volume image, and (c) extracted MG volume image. In the processed volume image (b), red and green color regions represent the conjunctiva layer (CL) and the meibomian glands (MGs), respectively. (Source: **Ju *et al.*** *Three-dimensional volumetric human meibomian gland investigation using polarization-sensitive optical coherence tomography* [107])

Figure 4.5 illustrates the overall processing steps proposed in this research. In the 3-D volumetric OCT intensity image shown in Fig. 4.5(a), the conjunctiva layer and MGs appear with different intensities. On the other hand, the conjunctiva layer and MGs are displayed by red and green colors in Fig. 4.5(b), respectively. Here, red and green represent the regions over and below the DOPU threshold, respectively.

After differentiating each region based on the threshold, the conjunctiva layer is segmented and applied to the OCT image as a binary mask. As a result, exclusive visualization of MG structure is achieved as shown in Fig. 4.5(c).

4.3.3 Acinar atrophy with advancing age

To demonstrate the clinical potential of the proposed method, age-dependent MG alteration is investigated as one of the clinical applications. For this purpose, six upper eyelids without dry eye disease and MGD disorder from six subjects of different ages are involved in this study. This *in vivo* measurements were approved by the Institutional Review Board of the University of Tsukuba and conformed to the Declaration of Helsinki.

According to the several reports [108–110], MGs may undergo a degenerative atrophic process with progressive destruction of the tissue inside the lid. In addition to increasing intraglandular pressure due to stasis of continuously produced meibum, advancing age is also able to affect such atrophic degeneration as in other organs of the human. [110, 111] A decreasing number of active glands indicated by gland dropout is considered as one of the evidence of a natural aging process occurred on the lid. Recently, high age-dependent dropout rate of MGs between the age of 20 and 80 years was observed using the meibography technique. Obata *et al.* [110] who described acinar atrophy without distinct dilatation as one of the pathological finding in MGs, suggest that acinar atrophy may lead to a decrease in the MG secretion with aging. Unlike normal round-shaped acini, atrophic acini tend to show small and irregular shape.

Figure 4.6 shows the extracted 3-D volumetric MG structures obtained from the subjects: (a) 28 years, (b) 32 years, (c) 56 years, (d) 63 years, (e) 72 years, and

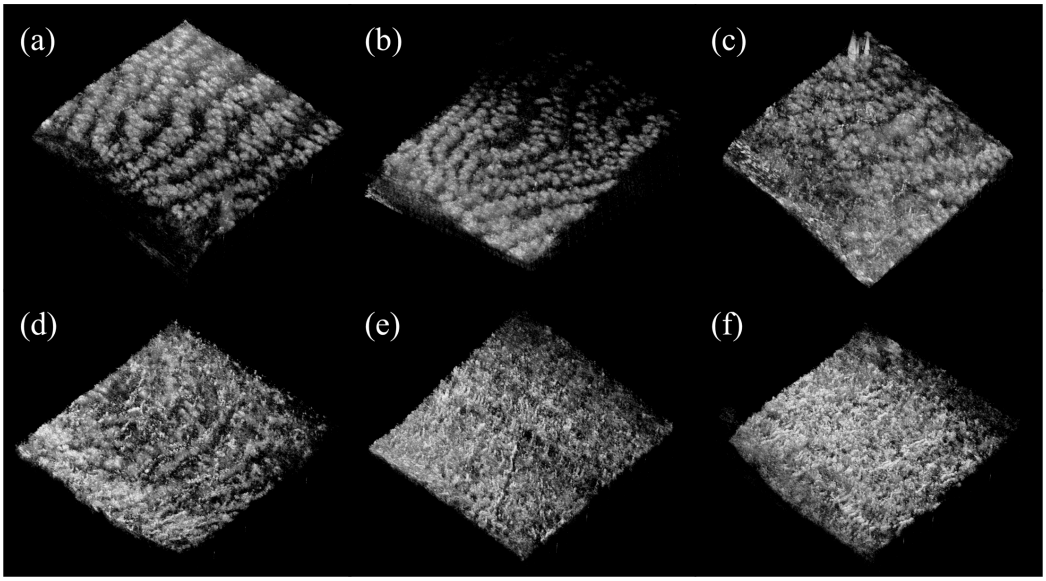

Figure 4.6: Extracted MG volume structure images from the subjects with different ages. (a) 28 years, (b) 32 years, (c) 56 years, (d) 63 years, (e) 72 years, and (f) 82 years old. (Source: **Ju *et al.*** *Three-dimensional volumetric human meibomian gland investigation using polarization-sensitive optical coherence tomography* [107])

(f) 82 years old. In Figs. 4.6(a) and 4.6(b), round-shaped and well-arranged multiple acini are clearly observed. However, in Fig. 4.6(c), noticeable gland dropout process starts to appear at the bottom of the image, even though several MG branchs still remain intact at the top. This decreasing number of active glands is considered as one of the evidences of a natural aging process on the lid. In addition, the MG structure with small and irregular shape is also found in Fig. 4.6(d). Unlike the other cases, most of the acini are not recognizable anymore in Figs. 4.6(e) and 4.6(f), instead randomly distributed thread-shaped structures are observed.

4.4 Discussion

Up to now, various imaging modalities have been developed and employed for grading the scale of MG dropout that can be used as a parameter for diagnosis of

MG-related diseases. Although there are several studies using different grading methods [111–116], there are no agreed and established standards to grade MG dropout. JMT has been developed as one of the prototypes of polarization sensitive OCT (PS-OCT) systems. Currently, PS-OCT is not commercially available. However several prototypes of PS-OCT including JMT have been implemented and employed to demonstrate its clinical application on posterior [57, 117] and anterior eye segments [56,118]. Once commercial PS-OCT is released because of its potential clinical applications, it can be expected to be utilized as clinical routine like conventional ophthalmic OCT. In the future, with advanced quantitative analysis method, 3-D volumetric MG visualization presented in this study will be possible to establish standard criteria for grading MG dropout, and to be used as a routine measurement for monitoring MG alteration and for diagnosis of MG-related diseases.

4.5 Summary

In summary, distinctive polarization features of the conjunctiva layer and the MGs were investigated by using JMT system. Especially, from the DOPU contrast, the discrimination criteria were empirically determined as the DOPU threshold. Using the threshold, segmentation of the conjunctiva layer and exclusive visualization of the MG structure were successfully achieved. In addition, age-dependent MG structure variation was also observed through *in vivo* measurements of several subjects with different ages, which demonstrated the clinical utility of the system for monitoring MG alteration and diagnosis of MG-related dry eye disease.

Chapter 5

Corneal collagen cross-linking investigation*

In this chapter, JMT is utilized for observing morphological change followed by CXL treatment and evaluating cross-linking effect on cornea. For corneal imaging, the JMT system in Chapter 3 is slightly modified with a single objective lens and simplified polarization delay unit.

5.1 Introduction

Corneal collagen cross-linking (CXL), a nearly non-invasive treatment method, has been developed to slow down or halt the progression of keratoconus [119]. The procedure of CXL is based on application of combined ultraviolet-A (UV-A) light and riboflavin (vitamin B2). Riboflavin injection followed by UV-A irradiation causes photochemical reaction (photosensitized oxidation) [120] that gives rise to

*This chapter has been mainly adopted from the following publication:
M. J. Ju, and S. Tang, "Usage of polarization-sensitive optical coherence tomography for investigation of collagen cross-linking," J. Biomed. Opt. **20**, 046001 (2015)

cross-linking by forming intra- and inter- fibrillar covalent bond between collagen fibrils in the corneal stroma [121]. As a result, mechanical stiffness of the cornea and its biochemical resistance to enzymatic digestion are increased [122, 123], which impedes the progression of keratoconus. Owing to its safety, positive clinical outcomes, and simple protocol, CXL treatment has become very common, [119], and its clinical sustaining effects have been demonstrated [124]. Since then, detection and measurement of the treatment results have been getting a lot of attention.

To date, several optical imaging techniques have been applied to investigate the morphological changes and to identify the treatment effect on cornea after the CXL treatment. Mazzotta *et al.* [125] investigated the side-effects of CXL treatment such as stromal edema, rarefaction, and stromal keratocyte reappearance with time using confocal laser scanning microscopy (CLSM) that enabled the observation and evaluation of corneal layers and nerves at the sub-cellular level [126–129]. With immunofluorescence confocal imaging system, Bottós *et al.* [130] directly visualized ultrastructural stromal modification in porcine cornea after CXL procedure and quantitatively assessed the CXL treatment effect. However, staining with specific fluorescent dye and/or contrast agent for targeting cellular components requires additional sample preparation and can be toxic to tissues. Bueno *et al.* [131] identified morphological changes in corneal stroma after CXL treatment in bovine and porcine eyes using nonlinear microscopy which provides two-photon excitation fluorescence (TPEF) and second harmonic generation (SHG) corneal images without any staining process [132–135]. Although those microscopic imaging modalities can achieve subcellular spatial resolution, their imaging speed, penetration depth, and field of view are limited. As an alternative imaging method, Doors *et al.* [136] used anterior segment optical coherence tomography (AS-OCT) to report short-term CXL treat-

ment result and its relationship with morphological characteristics appearing after the treatment. Although this method has high imaging speed, deep penetration depth and large field of view, it is only capable of providing scattering property without other functional tissue properties such as birefringence.

In human eye imaging, PS-OCT has been demonstrated to distinguish structures with birefringent, polarization preserving, and depolarizing properties [58, 62, 71, 74, 83, 137, 138]. Due to the fact that cornea consists of highly organized collagen fibrils in the stroma, it is known to have birefringence, and abnormalities in the cornea such as keratoconus causing the disruption in the organization of the collagen fibrils appear with alternation of the birefringence [139].

As one of the sub-types of PS-OCT, JMT has been also utilized to investigate the birefringence property of keratoconus [118, 139]. Recently, Alonso-Canerio *et al.* [140] reported promising potential of JMT for identifying the changes occurred after chemical agent (glutaraldehyde)-based CXL treatment on porcine cornea.

The aim of this pilot study presented in this chapter is to assess the utility of JMT to image and discriminate the morphological variation caused by more clinically relevant riboflavin/UV-A induced collagen cross-linking treatment on cornea. The riboflavin instillation followed by UV-A irradiation is applied on freshly enucleated bovine eyes in order to stimulate cross-linking. Using JMT, the cross-linking effect is observed in cross-sectional structure with standard scattering OCT image, and polarization contrast images such as phase retardation and degree of polarization uniformity (DOPU) [74]. With graph theory-based cornea segmentation algorithm [141], the thickness variation caused by CXL is also quantitatively analyzed. In particular, a global threshold is set from averaged DOPU depth-profile and applied for estimating the effective cross-linking depth. Furthermore, both

standard and accelerated CXL protocols are applied on the bovine cornea, and the cross-linking effectiveness following the different protocols are compared.

5.2 Materials & methods

5.2.1 System

Figure 5.1 shows the schematic and photograph of the JMT system modified for corneal imaging from the system presented in Fig. 3.1 . The system design and processing principle are very similar to the system described in Sect. 3.2.1. The system is based on a MEMS-based swept-source (Axsun Technology Inc., MA) with 100-kHz sweeping rate, a center wavelength of 1060 nm, and a spectral range around 110 nm. These properties of the light source determine the depth resolution of the system, which is measured to be 8.1 μm in air. The light source is directed to a 90:10 fiber coupler after passing through a fiber isolator that is inserted for protection of the light source from back-reflected light; 90% and 10% of the light is coupled to a passive polarization delay unit and a reference arm, respectively.

The polarization delay unit composed of a linear polarizer, a polarization beam splitter (PBS), and two mirror-based retroreflectors is employed for multiplexing two polarization states of the light source by splitting the beam into two orthogonal linear polarization states, delaying one to the other by adjusting one of the retroreflectors, and recombining them. The light from the polarization delay unit is then directed to a 50:50 fiber coupler. The two ports of the fiber coupler are connected to a sample arm and a phase stabilization unit, respectively. From the phase stabilization unit that consists of a fiber collimator, lens and mirror, phase calibration signal is generated and utilized for stabilizing the phase of OCT signal

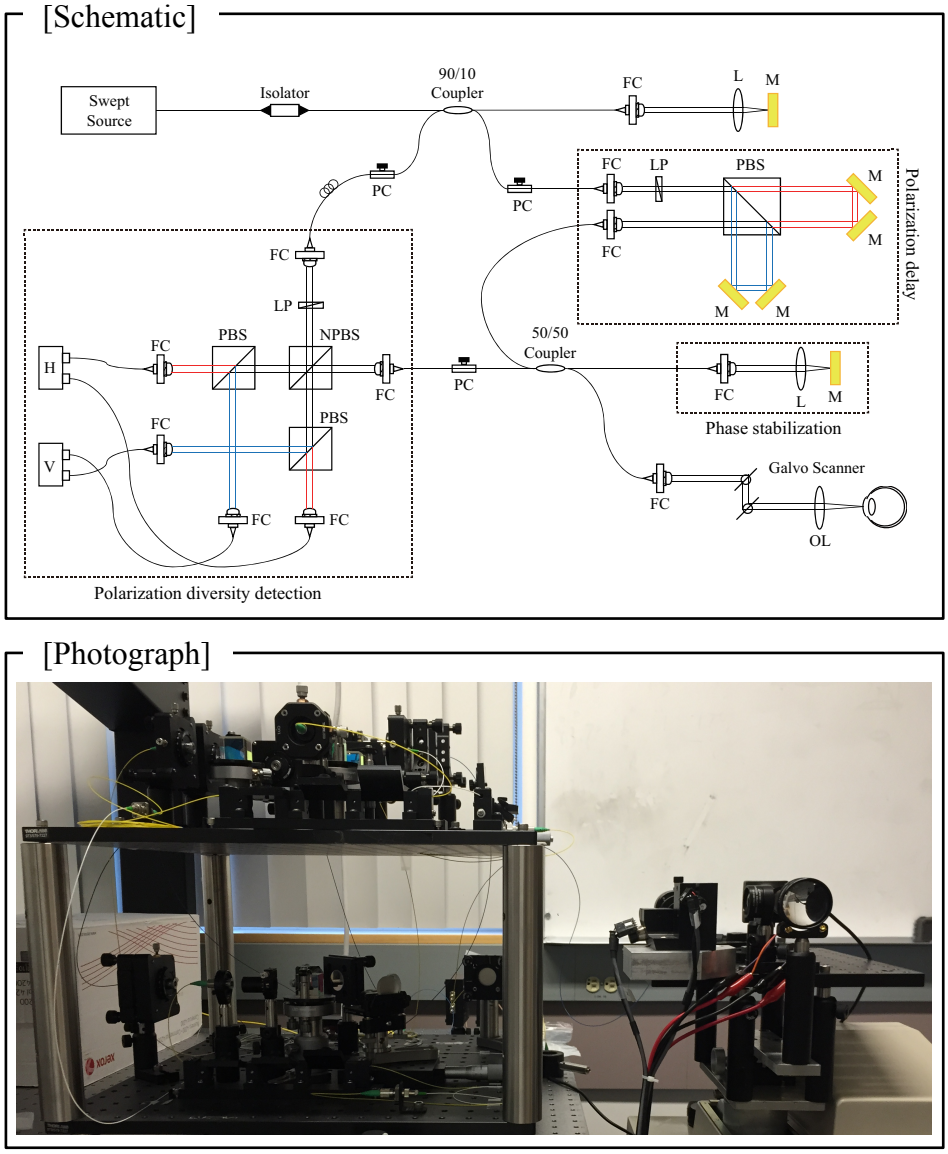

Figure 5.1: Schematic and photograph of JMT system for cornea imaging. LP: linear polarizer, PC: polarization controller, FC: fiber collimator, M: mirror, PBS: polarizing beam splitter, NPBS: non-polarizing beam splitter, H and V: horizontal and vertical balanced photo-detectors. (Source: **Ju *et al.*** *Usage of polarization-sensitive optical coherence tomography for investigation of collagen cross-linking* [142])

among A-scans. The detailed description of the unit and data processing is precisely illustrated in Sect. 3.2.2.

The sample beam passes through a collimator (F280 APC-C, Thorlabs Inc., NJ), a two-axis galvanometer scanner, and an objective lens (AC254-060-C-ML, Thorlabs Inc., NJ) and finally illuminates the eye. The reference beam, reflected by a mirror and recoupled to the 90:10 coupler, is aligned to the linear polarization state of 45-degree angle by a linear polarizer in the polarization diversity (PD) detection unit that also consists of a non-polarization beam splitter (NPBS), two PBSs, and two balanced photodetectors (BPDs, PDB430C, Thorlabs Inc.). In the PD detection unit, the reference light combines with the back-scattered sample light from the eye at the NPBS. The combined light is then split into horizontal and vertical polarization components by the PBSs, and finally interference signal is detected by the BPDs.

In the sample arm, a collimated light with diameter of 3.4 mm is introduced into the objective lens with a focal length of 60 mm. The lateral resolution is estimated to be around 14 μm. The measurable imaging depth range is determined to be around 2.95 mm with the polarization delay displacement of about 3 mm that is set by the polarization delay unit. With an optical probing power of 1.5 mW which is below the laser safety limit defined by ANSI [34], the sensitivity and signal roll-off are measured to be 93.5 dB and -0.64 dB/mm, respectively. Table 5.1 shows the specification summary of the JMT system used in this chapter.

Table 5.1: Summary of the specifications of the JMT for cornea imaging.

Center wavelength	**Wavelength band width**	**Wavelength sweeping speed**	**Sample probing power**
1.06 μm	111 nm	100 kHz	1.5 mW
System sensitivity	**Sensitivity roll-off**	**Measurable depth-range**	**Depth resolution (in air)**
93.5 dB	-0.64 dB/mm	2.95 mm	8.1 μm

5.2.2 Specimen preparation

To investigate cross-linking effect on corneal stroma in detail after CXL procedure, several bovine corneas with different preparation processes are measured *ex vivo*. Fresh bovine ocular globes (30 specimens) are obtained from a local abattoir (Pitt Meadows Meats Ltd., Canada). All eyes are from less than 8 months old animals, enucleated and transported within two hours post-mortem. During the transportation, the samples are submerged in physiologic saline medium (0.9 % sodium chloride irrigation, Baxter Corp.) and kept in a cool box. Without staining or fixation, the eyes are submerged under BSS sterile irrigation solution (Alcon Canada Inc., Canada) in a container with the anterior side facing the probe beam, and imaged within 24 hours post-mortem. The bovine eyes are divided into 4 groups according to the different preparation processes.

For the CXL group (10 eyes), conventional CXL procedure is performed as following the standard protocol (Wollensak *et al.* [119]). In order to allow the photosensitizer solution to diffuse into the stroma, after removing corneal epithelium using a scalpel, riboflavin solution (10 mg riboflavin-5-phosphaste 0.1 % in 10 mg

dextran-T-500 20 % solution, Macdonald's prescriptions laboratory, Canada) is administrated every 5 minutes for 30 minutes. Next, UV-A light irradiance with 365 nm wavelength and 3 mW/cm^2 power is applied for 30 minutes (Energy dose of 5.4 J/cm^2). During the UV-A exposure time, instillation of riboflavin solution is continued every 5 minutes.

For the accelerated CXL (ACXL) group (10 eyes), similar protocol as CXL procedure except with a higher UV-A irradiation power of 9 mW/cm^2 but a shorter exposure time of 10 minutes is applied where the same energy dose of 5.4 J/cm^2 is used.

Two control groups are designed. In control A (5 eyes), only mechanical epithelial debridement are performed. In control B (5 eyes), instillation of riboflavin solution at every 5 minutes is applied for 30 minutes additionally. No UV-A irradiation is applied to either control group.

5.2.3 Measurement and post-processing protocol

Jones matrix images are acquired from the center of the cornea. A transversal area of 4.5 mm is scanned with 512 A-lines to form a B-scan image and 10 B-scans are successively taken at the same location. With the multiple B-scans, global-phase-corrected sensitivity-enhanced scattering OCT image is created. For phase retardation image, adaptive Jones matrix averaging with a kernel size of 3 $\times$ 5 pixels (axial $\times$ lateral) is applied for improving the image quality of phase retardation. Finally, DOPU image is also produced from the averaged Jones matrix image. Here, since accuracy of the polarization-dependent measurements can be drastically affected by the signal-to-noise ratio (SNR) [86], data points whose effective SNR is lower than 10 dB are discarded in the computation of the phase retardation and DOPU images.

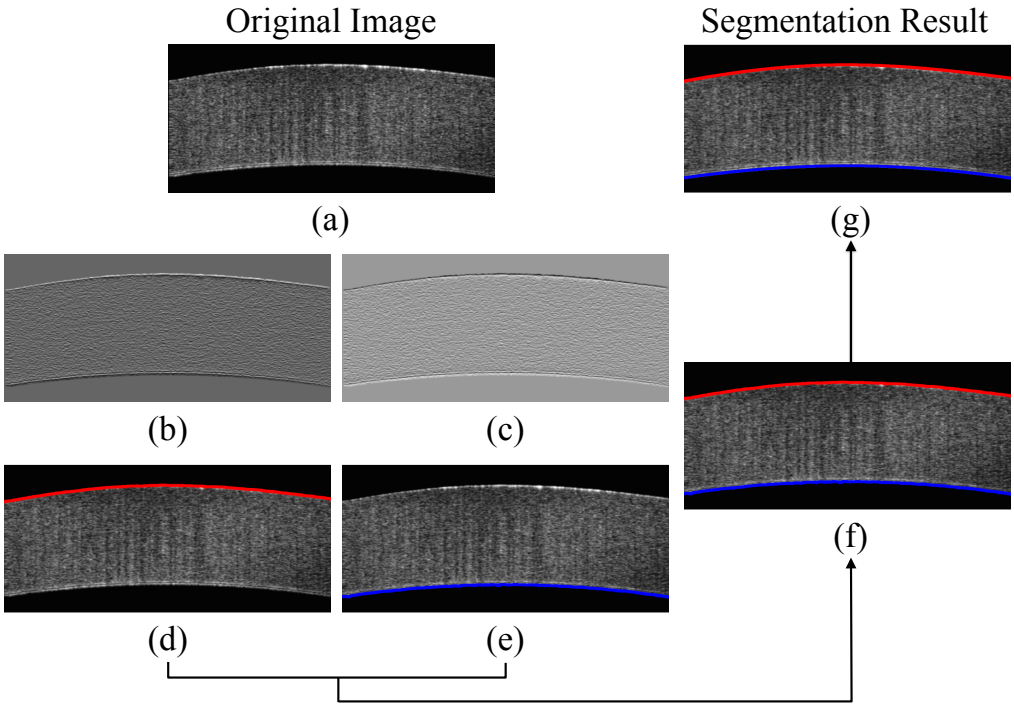

Figure 5.2: Graph theory-based cornea segmentation procedure. Original OCT intensity image (a), positive and negative gradient images ((b) and (c)), top and bottom cornea boundaries ((d) and (e)) obtained from the gradient images, segmented cornea layer (f), and final segmentation result with 2^{nd} order polynomial fitting process (g). (Source: **Ju *et al.*** *Usage of polarization-sensitive optical coherence tomography for investigation of collagen cross-linking* [142])

In order to identify the time-dependent morphological variation caused by the CXL procedure, each eye sample is imaged every 10 minutes over a period of 2 hours.

5.2.4 Corneal thickness calculation

In order to measure the corneal thickness, a simplified version of the graph theory-based cornea segmentation algorithm [141] is applied in this study. The segmentation process is illustrated with one eye of the control A group as shown in Fig. 5.2.

First, positive gradient (Fig. 5.2(b)) and negative gradient (Fig. 5.2(c)) im-

ages are obtained from the scattering OCT image (Fig. 5.2(a)). Second, from the gradient images, the surface (Fig. 5.2(d)) and the bottom (Fig. 5.2(e)) boundaries corresponding to Bowman's membrane and corneal endothelium layers, are determined and then overlapped with the original OCT image (Fig. 5.2(f)). Finally, the segmented layers are fitted by second order polynomial fitting process and delineated as shown in Fig. 5.2(g).

With these fitted boundary information, the mean and standard deviation (SD) of the overall corneal thickness are calculated and used for quantitative analysis of the time-dependent thickness variation described in Sect. 5.3.2. Here, a refractive index of bovine stroma (n = 1.376) [143] is used in this study for calculating the corneal thickness because the dominant corneal layer component within the measurement range is stroma after removing the epithelium layer.

5.3 Results

5.3.1 Cross-linking effect on cornea

Figure 5.3 shows the representative JMT measurement results of the control A (upper row; taken immediately after removing the corneal epithelium) and CXL group (bottom row; taken right after completing CXL procedure). In Fig. 5.3, each column represents scattering OCT ((a) and (d)), phase retardation ((b) and (e)), and DOPU images ((c) and (f)), respectively.

In the case of control A, within the stromal layer, homogeneous intensity distribution and random phase retardation are observed in the scattering OCT image (Fig. 5.3(a)) and the phase retardation image (Fig. 5.3(b)), respectively. In addition, as shown in Fig. 5.3(c), no remarkable feature is identified with the DOPU contrast.

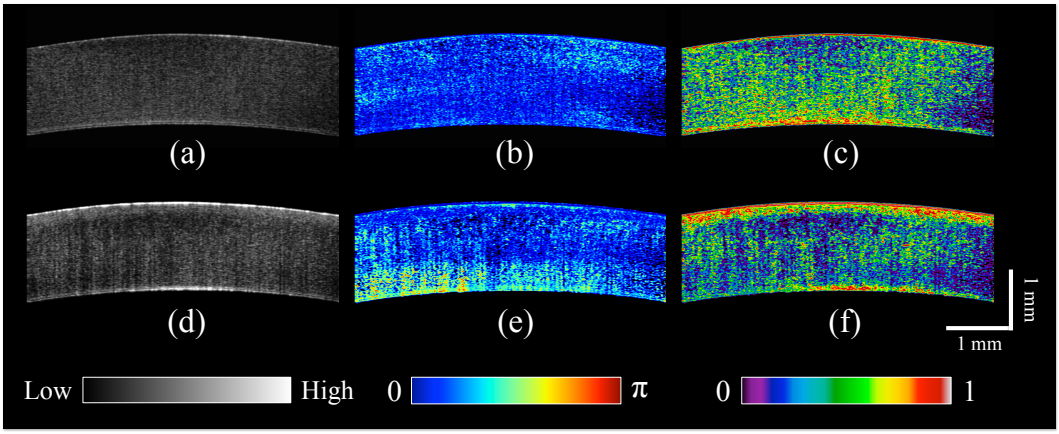

Figure 5.3: Representative B-scan images of the bovine cornea. Upper and bottom rows represent control A and CXL group, respectively. Scattering OCT images ((a) and (d)), phase retardation images ((b) and (e)), and DOPU images ((c) and (f)) are shown. scale bars show 1 mm. (Source: **Ju *et al.*** *Usage of polarization-sensitive optical coherence tomography for investigation of collagen cross-linking* [142])

In the CXL group, on the other hand, the anterior part of the stroma appears with a slightly higher contrast in the scattering OCT image (Fig. 5.3(d)). Unlike the control case, a depth-oriented slow increase is observed in the phase retardation image (Fig. 5.3(e)). Particularly, a distinctive zone is clearly identified at the anterior stroma in the DOPU image (Fig. 5.3(f)) as exhibiting an increased DOPU contrast. In this study, this distinctive region observed within the anterior stroma after CXL procedure is defined as an effective cross-linking region, which is more specifically described in Sect. 5.4.

The histograms of the phase retardation are further shown in Fig. 5.4. Because of the depth-oriented phase retardation increase within the effective cross-linking area, asymmetrical shape known as right-skewed distribution pattern is observed in the histogram of the CXL group (blue bars), while a pattern very close to normal distribution is found from the histogram of control A (red bars).

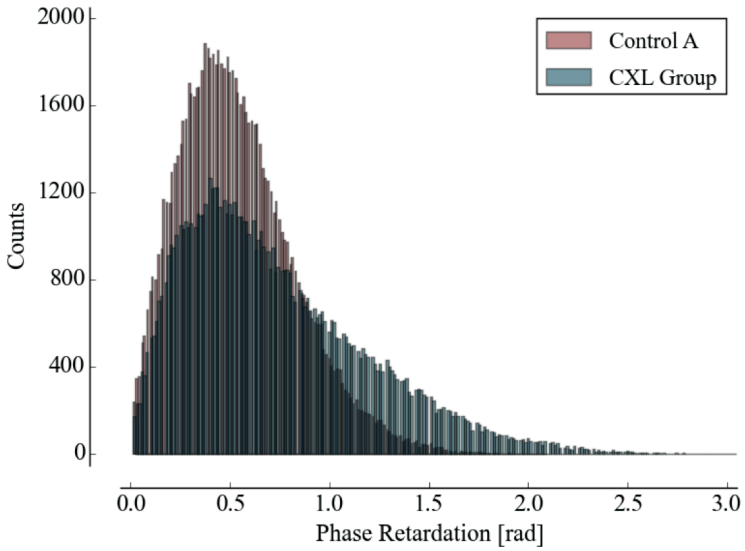

Figure 5.4: Histograms of the phase retardation of control A (red bars) and CXL group (blue bars). (Source: **Ju *et al.*** *Usage of polarization-sensitive optical coherence tomography for investigation of collagen cross-linking* [142])

5.3.2 Corneal thickness change

During the time-series measurement, it is noticed that the CXL procedure causes corneal thinning. In order to identify the main factor of the corneal thinning, measurement results of three different groups with time intervals of 1 hour are compared as shown in Fig. 5.5: control A (without riboflavin instillation and UV-A irradiation, upper row ((a)–(c))), control B (with riboflavin instillation but without UV-A irradiation, middle row ((d)–(f))), and CXL group (with riboflavin instillation and UV-A irradiation, bottom row ((g)–(i))). Each time-series measurement starts after the corneal epithelium abrasion (control A), riboflavin administration for 30 minutes (control B), and UV-A illumination for 30 minutes (CXL group), respectively.

As shown in Fig. 5.5, the corneal thickness reduction could be observed from all of the three groups listed above, even though the eyes are immersed in irrigating

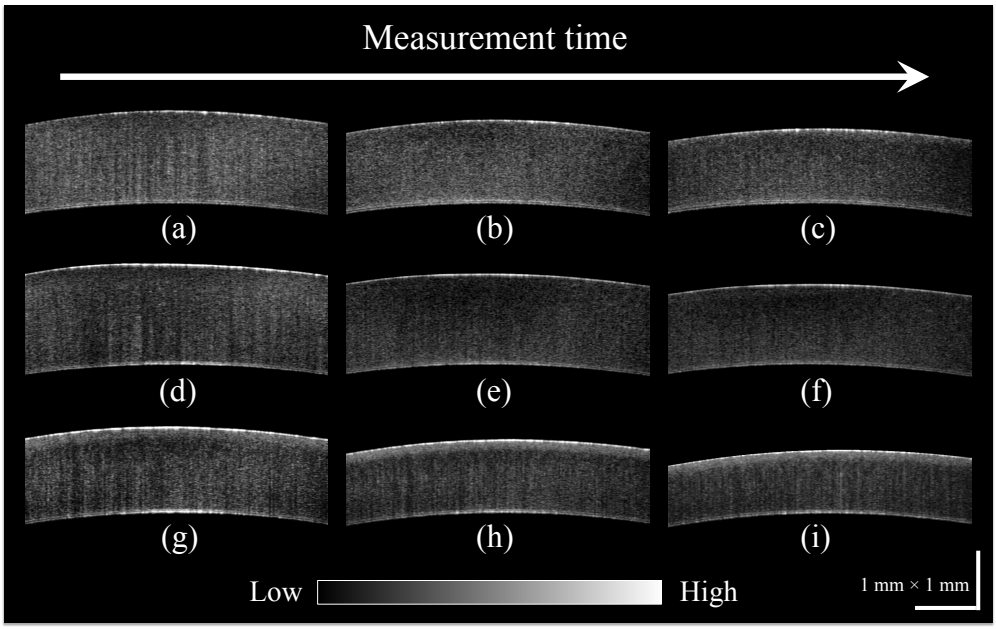

Figure 5.5: Representative OCT intensity B-scan time-series images of control A (upper row), control B (middle row), and CXL group (bottom row) with time intervals of 1 hour. (Source: **Ju *et al.*** *Usage of polarization-sensitive optical coherence tomography for investigation of collagen cross-linking* [142])

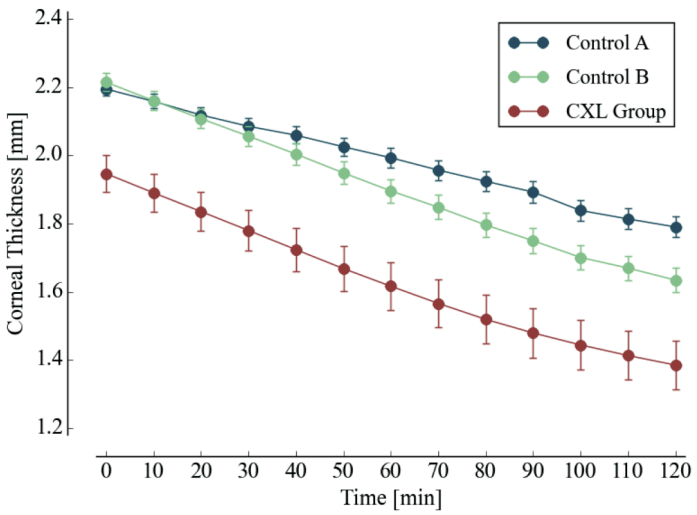

Figure 5.6: Corneal thickness change with time of three different measurement groups. Control A (blue), Control B (green), and CXL Group (red) are plotted. (Source: **Ju *et al.*** *Usage of polarization-sensitive optical coherence tomography for investigation of collagen cross-linking* [142])

solution to avoid dehydration effect. Nevertheless, more rapid progression of corneal thinning is found from both the control B and CXL group.

Using the corneal thickness calculation method described in Sect. 5.2.4, the mean corneal thickness of each group and its variation over 2 hours with time intervals of 10 minutes are measured and plotted in Fig. 5.6. From control A, dehydration effect on the corneal thickness given by the experiment condition is confirmed by its mean thickness change rate of -3.33 μm/min (thickness from 2.19 $\pm$ 0.02 mm to 1.79 $\pm$ 0.03 mm). From CXL group, the mean thickness decrease rate of -4.75 μm/min (thickness from 1.95 $\pm$ 0.05 mm to 1.38 $\pm$ 0.07 mm) is found, which demonstrates the corneal thinning followed by CXL procedure as showing more steep decrease in corneal thickness as comparing with control A. In addition, comparable corneal thickness change rate of -4.83 μm/min (thickness from 2.21 $\pm$ 0.03 mm to 1.63 $\pm$ 0.04 mm) is also observed in control B. While dehydration in the *ex vivo* cornea is

unavoidable under the current experimental condition, the faster thinning rate in the control B and CXL group indicates that additional corneal thinning happens due to the riboflavin instillation that is the common process of these two groups (not in the control A). Accordingly, it seems that the main factor for the CXL-induced corneal thinning is the dehydration effect from the riboflavin solution instead of the UV-A irradiation.

Here, it should be noted that the refractive index change caused by the dehydration effect is not considered in this cornea thickness calculation with the constant refractive index of 1.376 (Sect. 5.2.4).

5.3.3 Time-series investigation of CXL effect

After completing CXL procedure, dynamical morphology change with time occurs and is observed in scattering OCT, phase retardation, and DOPU images. Figure 5.7 presents a series of tomographic Jones matrix images ((a)–(i)) of the cornea after CXL procedure and the averaged depth-profiles of each contrast image ((j)–(l)).

From the scattering OCT images (Figs. 5.7(a), (d) and (g)), it can be found that the effective cross-linking region defined in Sect. 5.3.1 becomes more and more hyper-scattering as time passes. From the phase retardation images (Figs. 5.7(b), (e) and (h)), the effective region starts to appear with slow phase retardation increase in depth, and exhibits a higher value of phase retardation increase as time progresses (shown more clearly in the averaged depth-profile of phase retardation (Fig. 5.7(k))). In the DOPU contrast images (Figs. 5.7(c), (f) and (i)), pixels with high DOPU values are observed within the effective cross-linking region, in which the density of the high DOPU value pixels increases as time progresses.

Figures 5.7(j), (k) and (l) show the averaged depth-profiles of each contrast

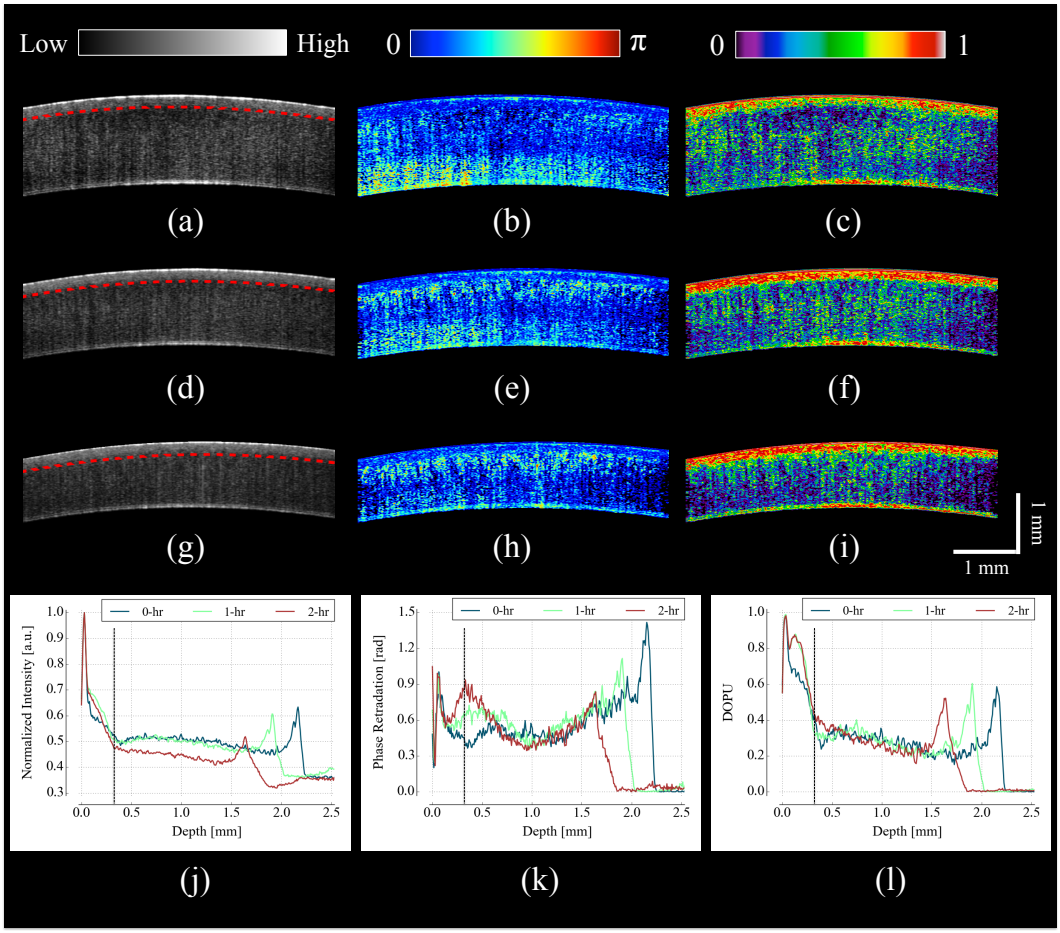

Figure 5.7: Time-series measurement result of CXL Group. Jones matrix tomography images in the first, second, and third rows were taken immediately, 1 hour, and 2 hours after CXL procedure, respectively. Scattering OCT images ((a), (d) and (g)), phase retardation images ((b), (e) and (h)), and DOPU images ((c), (f) and (i)) are shown. scale bars show 1 mm. Bottom row represents depth-profile analysis of Jones matrix time-series measurement. Averaged depth-profiles of normalized intensity (j), phase retardation (k), and DOPU (l) are shown. The effective cross-linking depth (2 hours after CXL procedure), determined by a DOPU threshold of 0.4, is marked by the black dotted-lines. The estimated effective cross-linking depths for 0, 1 and 2 hours are displayed by red dashed-lines in the scattering OCT images ((a), (d) and (g)), respectively. (Source: **Ju *et al.*** *Usage of polarization-sensitive optical coherence tomography for investigation of collagen cross-linking* [142])

image obtained by averaging the A-lines along the B-scan direction (after image flattening with cornea layer segmentation (Sect. 5.2.4)). In this study, from the averaged DOPU depth-profile (Fig. 5.7(l)), the DOPU quantity of 0.4 is empirically determined as a global threshold for estimating the effective cross-linking depth that represents the transition between the cross-linking affected and non-affected regions in the cornea. As an example, the effective cross-linking depth corresponding to 2 hours after CXL are estimated as the depth of intersection with the DOPU threshold, and its result is marked by black dotted-line in Figs. 5.7(j)–(l). At the estimated effective cross-linking depth, local minimum intensity and phase retardation increase are observed in the averaged depth-profile of normalized intensity (Fig. 5.7(j)) and phase retardation (Fig. 5.7(k)), respectively. From the scattering OCT images (Figs. 5.7(a), (d) and (g)) where the effective cross-linking depth is delineated by red dashed-line, it can be found that the estimation result closely matches with the boundary of the effective cross-linking region.

5.3.4 Time-series investigation of ACXL effect

In the standard CXL procedure, it involves 30 minutes of UV-A irradiation at an intended irradiance of 3 mW/cm^2 with total surface energy dose of 5.4 J/cm^2 (Dresden protocol [119]). Although the conventional CXL treatment has been demonstrated for its safety and long-term treatment effectiveness in different clinical trials [144–148], its long procedure time lasting from 40 minutes to 1 hour may lead to patient discomfort.

According to the photochemical law of reciprocity (Bunsen-Roscoe law) [149], it is believed that the photochemical process behind cross-linking depends on the absorbed UV-A energy and its following biological effect is proportional to the total

energy dose delivered to the biological tissue. Based on this physical theory, for accelerating the cross-linking procedure so called accelerated corneal cross-linking (ACXL) [150, 151], it is possible in principle to achieve identical biological effect by delivering the same amount of energy dose with reduced illumination time but increased irradiation UV-A intensity. In this study, ACXL procedure (10 minutes UV-A illumination at 9 mW/cm^2), with the same energy dose as standard 3 mW/cm^2 for 30 minutes, is carried out and its time-series effect is investigated.

Figure 5.8 presents a series of tomographic Jones matrix images ((a)–(i)) of the cornea after ACXL procedure and the averaged depth-profiles of each contrast image ((j)–(l)). Similarly to the standard CXL case, in the scattering OCT images (Figs. 5.8(a), (d) and (g)), the effective cross-linking area appears as hyper-scattering immediately after the ACXL procedure, and its intensity tends to increase as time progresses. Within the effective cross-linking region, increase of phase retardation with depth is observed in the phase retardation images (Figs. 5.8(b), (e) and (h)), and distinctive feature in comparison to the rest of the cornea is more clearly provided from DOPU images (Figs. 5.8(c), (f) and (i)).

Figures 5.8(j), (k) and (l) show the time-dependent change in the averaged depth-profiles of the normalized intensity, phase retardation, and DOPU images, respectively. Same as the standard CXL case, DOPU value of 0.4 in its depth-profile (Fig. 5.8(l)) is set as the threshold for estimating the effective cross-linking depth. The black dotted-line in the averaged depth-profile of Jones matrix images (Figs. 5.8(j), (k) and (l)) represents the effective cross-linking depth 2 hours after the ACXL procedure. In the scattering OCT images (Figs. 5.8(a), (d) and (g)), the effective cross-linking depth at 0, 1 and 2 hours, respectively, determined by the DOPU threshold is also marked by red dashed-line.

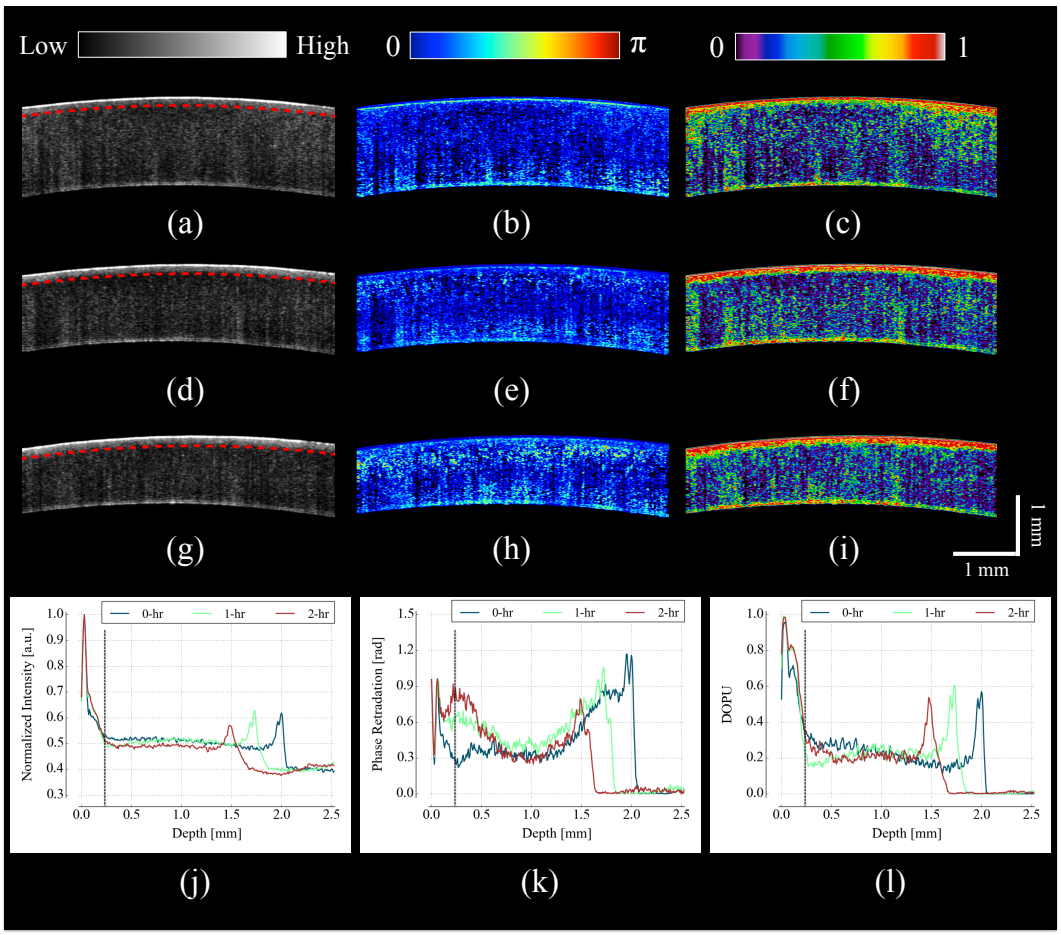

Figure 5.8: Time-series measurement result of ACXL Group. Jones matrix tomography images in the first, second, and third rows were taken immediately, 1 hour, and 2 hours after ACXL procedure, respectively. Scattering OCT images ((a), (d) and (g)), phase retardation images ((b), (e) and (h)), and DOPU images ((c), (f) and (i)) are shown. scale bars show 1 mm. Bottom row represents depth-profile analysis of Jones matrix time-series measurement. Averaged depth-profiles of normalized intensity (j), phase retardation (k), and DOPU (l) are shown. The effective cross-linking depth (2 hours after CXL procedure), determined by a DOPU threshold of 0.4, is marked by the black dotted-lines. The estimated effective cross-linking depths for 0, 1 and 2 hours are displayed by red dashed-lines in the scattering OCT images ((a), (d) and (g)), respectively. (Source: **Ju *et al.*** *Usage of polarization-sensitive optical coherence tomography for investigation of collagen cross-linking* [142])

5.3.5 Standard CXL vs. accelerated CXL (ACXL)

According to the *equal-dose* principle, the same cross-linking effect is expected from the two different CXL procedures applied in this study: CXL (30 minutes UV-A illumination at 3 mW/cm^2) and ACXL (10 minutes UV-A illumination at 9 mW/cm^2).

Although very similar morphological variation aspects are found in both CXL and ACXL procedure results as shown in Sect. 5.3.3 and Sect. 5.3.4, there is also perceptible difference in terms of the cross-linking effectiveness between the two CXL procedures. In this study, in order to evaluate the effectiveness, comparison of the effective cross-linking depth is firstly performed, and its result is shown in Fig. 5.9(a). As mentioned in Sect. 5.3.3 and Sect. 5.3.4, the effective cross-linking depth is estimated from the DOPU depth-profile by setting the DOPU threshold of 0.4. With the standard CXL procedure, the cross-linking depth is 261.51 $\pm$ 20.76 μm immediately after the procedure, and moderately increases to 313.52 $\pm$ 10.11 μm after 2 hours. In the case of the ACXL protocol, the effective cross-linking depth is firstly observed at 197.93 $\pm$ 11.74 μm, and reaches to 235.50 $\pm$ 7.36 μm 2 hours after the ACXL procedure.

In addition to the effective cross-linking depth, cross-linking effects followed by the two protocols are also examined with respect to the averaged mean DOPU value within the cross-linking region as shown in Fig. 5.9(b). From the ACXL group, as compared with the CXL group, higher mean DOPU values are observed at the initial and final staged of the time-series measurement. Meanwhile, the CXL group (from 0.54 $\pm$ 0.03 to 0.71 $\pm$ 0.01) shows more progressive incline aspect than the ACXL group (from 0.63 $\pm$ 0.02 to 0.74 $\pm$ 0.01).

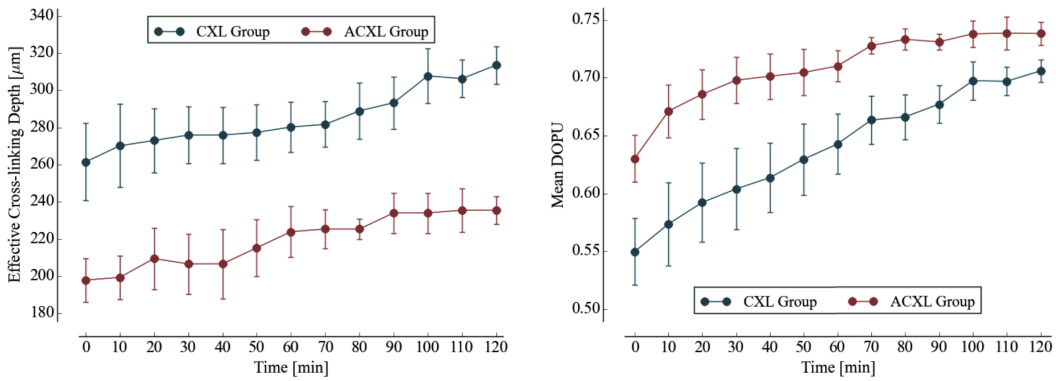

Figure 5.9: Comparison of collagen cross-linking effect of CXL and ACXL procedures. Effective cross-linking depth (a) and mean DOPU value (b) variations with time. (Source: **Ju *et al.*** *Usage of polarization-sensitive optical coherence tomography for investigation of collagen cross-linking* [142])

5.4 Discussion

In this project, the bovine cornea are measured *ex vivo* using JMT system in order to investigate the CXL treatment effects on the cornea.

Firstly, cornea thickness reduction followed by the treatment is observed and cross-examined with two different control groups. From the examination, it is found that the dehydration of the riboflavin solution is the main cause of the cornea thinning followed by the CXL treatment. Although the bovine cornea is used in this study based on its similar biochemical property with a human cornea [152], it still remains to be demonstrated that the results shown here extend to the human cornea. Especially, in the case of *in vivo* human cornea measurement, the thickness reduction may be compensated by the human body functions such as tears and a watery fluid inside of the anterior chamber.

The effective cross-linking region is also differentiated by JMT. It appears as

showing hyper-scattering, slow phase retardation change in depth, and high DOPU value. The effective cross-linking depth can be determined by empirical DOPU threshold. This depth matches well with the stromal demarcation line reported in the literatures [125, 136, 153–155].

Currently, it is believed that the stromal demarcation line observed after the CXL treatment represents the activation of keratocyte followed by the keratocyte repopulation and new collagen synthesis [156]. Based on this hypothesis, in general, the stromal demarcation line is regarded as the transition zone between cross-linked anterior corneal stroma and untreated posterior corneal stroma after CXL treatment. With slit-lamp examination, the stromal demarcation line could be detectable at a depth of about 300 μm as early as 2 weeks after the CXL procedure [153,154]. Using confocal microscopy and AS-OCT, the depth of cross-linking was also detected at a depth of 270 to 330 μm [125, 136, 155]. In this chapter, in the case of the standard CXL protocol, the effective cross-linking depth appears at 313.52 ± 10.11 μm, which corresponds well to the depth of the stromal demarcation line reported previously.

Recently, by using confocal microscopy, Dhaliwal *et al.* [157] observed hyper-reflective spherical structures with diameter of 4–10 μm in the anterior of the human cornea immediately after the CXL treatment for up to a depth of 300 μm. They also identified keratocyte damage (cell shrinking and apoptosis) by histology within the depth in which the spherical structures were visible. The authors stated that the spherical structures might represent damaged cells or cellular fragments. The hyper-scattering observed in our scattering OCT image could be regarded as affected by the hyper-reflective spherical structures.

In addition, Bottós *et al.* [130] directly visualized the cross-linking effect using confocal fluorescence imaging. After the CXL procedure, well organized and densely

packed collagen fiber distribution was pronouncedly observed within the limited anterior stroma that was regarded as cross-linked zone. The change in the phase retardation and DOPU contrasts observed in this study could be explained based on the above reported morphological evidence appearing after the CXL treatment. After the CXL procedure, the organization pattern of the collagen fibers in the anterior stroma changes to more dense and compact, which gives rise to moderate increase in the cumulative phase retardation image and high uniformity in the DOPU image within the cross-linked region.

In the presented experiments, different cross-linking progress aspects from two different CXL procedures are observed. The effective cross-linking depth is significantly deeper after after a 30 minutes CXL treatment than after a 10 minutes ACXL procedure. The conventional CXL procedure provides more progressive cross-linking effect on the cornea than the ACXL procedure, which is implied by more rapid and lasting rise of mean DOPU value with time. Based on these results, it would be possible to infer that photochemical reaction established by the Bunsen-Roscoe law cannot be directly corresponded to photo-biological effect on complex biological systems.

In this study, instead of the intensity threshold based method that is more straightforward approach in general, empirical DOPU threshold quantity is used for determining the effective cross-linking depth because DOPU is less affected by SNR and provides high consistency among the samples. In the future, more robust automatic segmentation and quantification of the cross-linking progress with polarization related parameters such as local birefringence should be devised in order to find optimal condition for maximizing cross-linking effect with minimized procedure time.

5.5 Summary

In this chapter, I introduced JMT as a reliable imaging modality in terms of evaluating the outcome of CXL treatment. Using JMT imaging, effective cross-linking depth and cross-linking progression as a function of time could be determined, which would be able to provide a direct clinical sign to detect effectiveness of CXL treatment. To date, specific criteria and/or guideline for achieving maximum cross-linking effect ensuring a long lasting outcome is still unknown. However, I believe it would be possible to find the optimal condition through mid-long term clinical study with the proposed method using JMT system.

Chapter 6

Conclusion & future directions

OCT is an interferometric based tomography technique for non-invasive measurement of biological tissue. Among the various clinical fields, in which OCT has been utilized, ophthalmology is regarded as one of the most successful applications of OCT technique. Recent developments in FD-OCT have dramatically improved the imaging speed and sensitivity, which make OCT become a standard tomography modality in ophthalmology.

In addition, functional extensions of OCT have been developed to acquire various physiological information for more comprehensive investigation. Most widely utilized functional extensions of OCT are Doppler OCT and PS-OCT. Doppler OCT has been utilized for retinal blood flow measurement, or for retinal and choroidal vasculature visualization. PS-OCT, capable of measuring the depth-resolved birefringence, has been developed for identification of ocular tissue properties, and for examination of ocular diseases.

Jones matrix tomography (JMT), developed as one of PS-OCT schemes, determines the polarization properties of ocular tissues. Conventional swept-source

based JMT employed EOM or AOM for modulating the incident polarization state. Usage of these active modulation devices causes extra expense in system configuration, instability in system performance, and complexity in data acquisition and processing.

In this dissertation, I have developed an advanced version of JMT and new JMT algorithms, which integrated sensitivity-enhanced scattering, Doppler phase shift, and polarization measurements. Using the JMT system, I successfully achieved multi-contrast ophthalmic imaging with high stability and sensitivity. In addition, several applications of JMT in ophthalmology are also demonstrated.

6.1 Development of advanced Jones matrix tomography system and retinal imaging

The advanced JMT system was developed by employing passive polarization delay scheme. Based on the inherent property of the delay unit, novel phase stabilization method was devised, which increased the overall system stability. Furthermore, advanced Jones matrix analysis algorithms have been developed, which enabled the system to perform multi-contrast Jones matrix imaging.

In vivo measurements of a healthy and pathologic posterior eyes were performed using the JMT in order to demonstrate its stability and functionality. Clear morphological features of macular and ONH were revealed with enhanced sensitivity after compensating the inherent sensitivity loss occurred in conventional JMT through processing of the coherent composition of matrix entry. Polarization property imaging such as phase retardation and DOPU provided additional tissue properties of retina structure which was not revealed from scattering contrast. In addition,

detailed vasculature of retina (macular and optic nerve head) which was invisible in the conventional scattering OCT were resolved by Doppler contrast.

6.2 Human meibomian gland imaging

As a promising clinical application of JMT, *in vivo* upper eyelid imaging was performed in order to visualizing meibomian gland (MG) located within a tarsal plate in the eyelid. From the Jones matrix measurement, distinctive features of the conjunctiva layer and the MGs were identified. Particularly, the discrimination criteria was empirically set from histogram-based DOPU contrast analysis. With the DOPU threshold, exclusive visualization of MG structure was achieved after segmenting the conjunctiva layer. Furthermore, *in vivo* measurements of several subjects with different ages were performed for investigation of acinar atrophy with advancing age. These results demonstrated the clinical utility of JMT system in ophthalmology.

6.3 Corneal imaging

I also demonstrated the utilization of JMT for investigating the morphological variations followed by corneal collagen cross-linking (CXL) treatment and for determining the effectiveness of the cross-linking. For this purpose, *ex vivo* bovine cornea imaging was performed after applying the CXL treatment. From the comparative study of cross-linking effect with two different control groups, the main factor for the corneal thickness reduction caused by CXL was identified. The effective cross-linking region was differentiated from different contrast images created by JMT, and its boundary was also determined from averaged DOPU depth-profile. In addition, accelerated version of CXL procedure, which needed shorter procedure time with higher UV-A

irradiation power, was also performed, and its outcomes were compared with those of the standard CXL procedure in terms of the effectiveness and progression of cross-linking. Based on these results, JMT would be useful for finding optimal condition for maximizing cross-linking effect with minimized procedure time.

6.4 Future directions

In this dissertation, I introduced a newly developed JMT system with improved stability and expanded functionality, and also demonstrated various clinical utilizations of JMT system. Some future developments and investigations can be carried out to further improve the system capability and applications.

Recently, optical coherence elastography (OCE), capable of determining biomechanical properties of tissues such as strain and elasticity, was utilized for quantifying local spatial variations in corneal tissue properties induced by CXL treatment [158]. Because of the high phase sensitivity of JMT, it is possible to adopt OCE technique into the current JMT system. With the combination of JMT and OCE, it can be expected to perform more comprehensive analysis of CXL induced mechanical and polarization property changes in cornea as well as its morphological variation.

Omodaka *et al.* [159] reported volumetric evaluation of the lamina cribrosa (LC) using SS-OCT. LC is the primary site of axonal damage in glaucoma that is the second most common cause of blindness [160]. For the purpose of glaucoma diagnosis, the authors developed LC segmentation algorithm and measured the average thickness of LC from healthy, early, and late stage glaucoma subjects. From the measurement results, they found significant correlation between glaucoma severity and LC thickness. For measuring LC thickness, the upper and lower borders of the LC and the flank of the LC were all identified only based on scattering contrast. As

a result, their segmentation algorithm tended to overestimate the LC thickness, especially when measuring tilted optic head disc. As shown in Fig. 3.4, JMT provides additional contrast to the LC. Since LC has strong birefringence property, LC can be clearly visualized with rapid change of phase retardation as shown in Fig. 3.4(b). Therefore, based on various contrast mechanisms provided by JMT, it is possible to quantify the LC thickness more precisely and robustly. Furthermore, through extensive pathological subject study using JMT, a clearer correlation between the LC thickness and status of the glaucoma can be found.

Novel clinical investigation of JMT is very important for expanding its feasibility in ophthalmology. However, as mentioned in Sect. 1.3, measurement speed is also important for *in vivo* ophthalmic imaging because of involuntary eye motion and its related artifacts. Therefore, improving of Jones matrix acquisition speed is quite natural and also necessary. In any swept-source based OCT, the sweeping rate of the source is key for determining measurement speed. Choi *et al.* [161] used 1050 nm vertical-cavity surface-emitting laser (VCSEL) source with 400 kHz wavelength sweeping rate for phase-sensitive Doppler OCT. Employing the VCSEL source into the current JMT system will be a robust, straightforward, and computationally efficient way to achieve high speed Jones matrix measurement. However, 1050 nm VCSEL source with over 400 kHz is not commercially available yet, and it will be very expensive to customize the VCSEL source for JMT system. As a result, this approach is not practical and not cost-efficient. As an alternative approach, optical switch based buffering technique [162] could be adopted into the current JMT system for reducing measurement time. With this strategy, the current 100 kHz sweeping rate with 50 % duty cycle could be doubled by maximizing the duty cycle of swept-laser close to 100 %. Although this method could not provide compara-

ble measurement speed as the VCSEL swept-source, it can be implemented with the current swept-source, and also can provide better performance in measurement speed.

With continuous improvement in JMT, this technique can find more and more applications in ophthalmology and other clinical fields.

Bibliography

[1] D. Huang, E. A. Swanson, C. P. Lin, J. S.Schuman, W. G. Stinson, W. Chang, M. R. Hee, T. Flotte, K. Gregory, C. A. Puliafito, and J. G. Fujimoto, Optical coherence tomography, Science **254**, 1178–1181 (1991).

[2] A. Rollins, S. Yazdanfar, M. Kulkarni, R. Ung-Arunyawee, and J. A. Izatt, In vivo video rate optical coherence tomography, Opt. Express **3**, 219–229 (1998).

[3] B. Potsaid, B. Baumann, D. Huang, S. Barry, A. E. Cable, J. S. Schuman, J. S. Duker, and J. G. Fujimoto, Ultrahigh speed 1050 nm swept source / Fourier domain OCT retinal and anterior segment imaging at 100,000 to 400,000 axial scans per second, Opt. Express **18**, 20029–20048 (2010).

[4] T. Klein, W. Wieser, L. Reznicek, A. Neubauer, A. Kampik, and R. Huber, Multi-MHz retinal OCT, Biomed. Opt. Express **4**, 1890–1980 (2013).

[5] S. Alam, R. J. Zawadzki, S. Choi, C. Gerth, S. S. Park, L. Morse, and J. S. Werner, Clinical application of rapid serial fourier-domain optical coherence tomography for macular imaging, Ophthalmology **113**, 1425–1431 (2006).

[6] V. J. Srinivasan, M. Wojtkowski, A. J. Witkin, J. S. Duker, T. H. Ko, M. Carvalho, J. S. Schuman, A. Kowalczyk, and J. G. Fujimoto, High-definition

and 3-dimensional imaging of macular pathologies with high-speed ultrahigh-resolution optical coherence tomography, Ophthalmology **113**, 2054.e1–2054.14 (2006).

[7] M. Hangai, Y. Ojima, N. Gotoh, R. Inoue, Y. Yasuno, S. Makita, M. Yamanari, T. Yatagai, M. Kita, and N. Yoshimura, Three-dimensional imaging of macular holes with high-speed optical coherence tomography, Ophthalmology **114**, 763–773 (2007).

[8] T. C. Chen, Spectral domain optical coherence tomography in glaucoma: Qualitative and quantitative analysis of the optic nerve head and retinal nerve fiber layer (An AOS thesis), Trans. Am. Ophthalmol. Soc. **107**, 254–281 (2009).

[9] J. A. Izatt, M. R. Hee, E. A. Swanson, C. P. Lin, D. Huang, J. S. Schuman, C. A. Puliafito, and J. G. Fujimoto, Micrometer-scale resolution imaging of the anterior eye in vivo with optical coherence tomography, Arch. Ophthalmol. **112**, 1584–1589 (1994).

[10] A. R. S. Radhakrishnan, Real-time optical coherence tomography of the anterior segment at 1310 nm, Arch. Ophthalmol. **119**, 1179–1185 (2001).

[11] J. Welzel, E. Lankenau, R. Birngruber, and R. Engelhardt, "Optical coherence tomography of the human skin," J. Am. Acad. Dermatol. **37**, 958–963 (1997).

[12] Y. Pan and D. L. Farkas, Noninvasive imaging of living human skin with dual-wavelength optical coherence tomography in two and three dimensions, J. Biomed. Opt **3**, 446–455 (1998).

[13] P. J. Tadrous, Methods for imaging the structure and function of living tissues and cells: 1. optical coherence tomography, J. Pathol. **191**, 115119 (2000).

[14] J. Welzel, Optical coherence tomography in dermatology: a review, Skin Res. Technol. **7**, 19 (2001).

[15] T. Gambichler, G. Moussa, M. Sand, D. Sand, P. Altmeyer, and K. Hoffmann, Applications of optical coherence tomography in dermatology, J. Dermatol. Sci. **40**, 85–94 (2005).

[16] T. Gambichler, R. Matip, G. Moussa, P. Altmeyer, and K. Hoffmann, In vivo data of epidermal thickness evaluated by optical coherence tomography: Effects of age, gender, skin type, and anatomic site, J. Dermatol. Sci. **44**, 145–152 (2006).

[17] V. R. Korde, G. T. Bonnema, W. Xu, C. Krishnamurthy, J. Ranger-Moore, K. Saboda, L. D. Slayton, S. J. Salasche, J. A. Warneke, D. S. Alberts, and J. K. Barton, Using optical coherence tomography to evaluate skin sun damage and precancer, Lasers Surg. Med. **39**, 687695 (2007).

[18] J. Lademann, N. Otberg, H. Richter, L. Meyer, H. Audring, A. Teichmann, S. Thomas, A. Knttel, and W. Sterry, Application of optical non-invasive methods in skin physiology: a comparison of laser scanning microscopy and optical coherent tomography with histological analysis, Skin Res. Technol **13**, 119132 (2007).

[19] B. Colston, U. Sathyam, L. DaSilva, M. Everett, P. Stroeve, and L. Otis, Dental OCT, Opt. Express **3**, 230–238 (1998).

[20] F. Feldchtein, V. Gelikonov, R. Iksanov, G. Gelikonov, R. Kuranov, A. Sergeev, N. Gladkova, M. Ourutina, D. Reitze, and J. Warren, In vivo OCT imaging of hard and soft tissue of the oral cavity, Opt. Express **3**, 239–250 (1998).

[21] B. T. Amaechi, S. M. Higham, A. G. Podoleanu, J. A. Rogers, and D. A. Jackson, Use of optical coherence tomography for assessment of dental caries: quantitative procedure, J. Oral Rehabil. **28**, 10921093 (2001).

[22] R. Brandenburg, B. Haller, and C. Hauger, Real-time in vivo imaging of dental tissue by means of optical coherence tomography (OCT), Opt. Commun. **227**, 203–211 (2003).

[23] J. Izatt, M. Kulkarni, H.-W. Wang, K. Kobayashi, and J. Sivak, M.V., Optical coherence tomography and microscopy in gastrointestinal tissues, IEEE Journal of Selected Topics in Quantum Electronics **2**, 1017 –1028 (1996).

[24] K. Kobayashi, J. A. Izatt, M. D. Kulkarni, J. Willis, and M. V. Sivak Jr., High-resolution cross-sectional imaging of the gastrointestinal tract using optical coherence tomography: preliminary results, Gastrointest. Endosc. **47**, 515–523 (1998).

[25] B. E. Bouma, G. J. Tearney, C. C. Compton, and N. S. Nishioka, High-resolution imaging of the human esophagus and stomach in vivo using optical coherence tomography, Gastrointest. Endosc. **51**, 467–474 (2000).

[26] S. Brand, J. M. Poneros, B. E. Bouma, G. J. Tearney, C. C. Compton, and N. S. Nishioka, Optical coherence tomography in the gastrointestinal tract, Endoscopy **32**, 796–803 (2000).

[27] B. Shen, G. Zuccaro Jr, T. L. Gramlich, N. Gladkova, P. Trolli, M. Kareta, C. P. Delaney, J. T. Connor, B. A. Lashner, C. L. Bevins, F. Feldchtein, F. H. Remzi, M. L. Bambrick, and V. W. Fazio, In vivo colonoscopic optical coherence

tomography for transmural inflammation in inflammatory bowel disease, Clin. Gastroenterol. Hepatol. **2**, 1080–1087 (2004).

[28] I.-K. Jang, G. J. Tearney, B. MacNeill, M. Takano, F. Moselewski, N. Iftima, M. Shishkov, S. Houser, H. T. Aretz, E. F. Halpern, and B. E. Bouma, In vivo characterization of coronary atherosclerotic plaque by use of optical coherence tomography, Circulation **111**, 1551–1555 (2005).

[29] N. Gonzalo, P. W. Serruys, T. Okamura, Z. J. Shen, Y. Onuma, H. M. Garcia-Garcia, G. Sarno, C. Schultz, R. J. v. Geuns, J. Ligthart, and E. Regar, Optical coherence tomography assessment of the acute effects of stent implantation on the vessel wall: a systematic quantitative approach, Heart **95**, 1913–1919 (2009).

[30] F. Prati, E. Regar, G. S. Mintz, E. Arbustini, C. D. Mario, I.-K. Jang, T. Akasaka, M. Costa, G. Guagliumi, E. Grube, Y. Ozaki, F. Pinto, and P. W. J. Serruys, Expert review document on methodology, terminology, and clinical applications of optical coherence tomography: physical principles, methodology of image acquisition, and clinical application for assessment of coronary arteries and atherosclerosis, Eur. Heart J. **31**, 401–415 (2010).

[31] T. Yonetsu, T. Kakuta, T. Lee, K. Takayama, K. Kakita, T. Iwamoto, N. Kawaguchi, K. Takahashi, G. Yamamoto, Y. Iesaka, H. Fujiwara, and M. Isobe, Assessment of acute injuries and chronic intimal thickening of the radial artery after transradial coronary intervention by optical coherence tomography, Eur. Heart J. **31**, 1608–1615 (2010).

[32] T. Kubo, C. Xu, Z. Wang, N. S. v. Ditzhuijzen, and H. G. Bezerra, Plaque and thrombus evaluation by optical coherence tomography, Int. J. Cardiovasc. Imaging **27**, 289–298 (2011).

[33] Y. Ozaki, H. Kitabata, H. Tsujioka, S. Hosokawa, M. Kashiwagi, K. Ishibashi, K. Komukai, T. Tanimoto, Y. Ino, S. Takarada, T. Kubo, K. Kimura, A. Tanaka, K. Hirata, M. Mizukoshi, T. Imanishi, and T. Akasaka, Comparison of contrast media and low-molecular-weight dextran for frequency-domain optical coherence tomography, Circ. J. **76**, 922–927 (2012).

[34] American National Standard Institute, *American National Standard for the Safe Use of Lasers ANSIZ 136.1 2014* (American National Standards Institute, 2014).

[35] CH/172/6, *Ophthalmic Instruments. Fundamental Requirements and Test Methods. General Requirements Applicable to All Ophthalmic Instruments, BS EN ISO 15004-1:2009* (International Organization for Standardization, 2009).

[36] R. A. Leitgeb, C. K. Hitzenberger, and A. F. Fercher, Performance of fourier domain vs. time domain optical coherence tomography, Opt. Express **11**, 889–894 (2003).

[37] J. F. de Boer, B. Cense, B. H. Park, M. C. Pierce, G. J. Tearney, and B. E. Bouma, Improved signal-to-noise ratio in spectral-domain compared with time-domain optical coherence tomography, Opt. Lett. **28**, 2067–2069 (2003).

[38] M. Choma, M. V. Sarunic, C. Yang, and J. A. Izatt, Sensitivity advantage of swept source and Fourier domain optical coherence tomography, Opt. Express **11**, 2183–2189 (2003).

[39] G. M. Hale and M. R. Querry, Optical Constants of Water in the 200-nm to 200-μm Wavelength Region, Appl. Opt. **12**, 555–563 (1973).

[40] W. Wieser, B. R. Biedermann, T. Klein, C. M. Eigenwilling, and R. Huber, Multi-Megahertz OCT: High quality 3D imaging at 20 million A-scans and 4.5 GVoxels per second, Opt. Express **18**, 14685–14704 (2010).

[41] T. Klein, W. Wieser, C. M. Eigenwilling, B. R. Biedermann, and R. Huber Megahertz OCT for ultrawide-field retinal imaging with a 1050 nm Fourier domain mode-lock laser, Opt. Express **19**, 3044–3062 (2011).

[42] B. R. White, M. C. Pierce, N. Nassif, B. Cense, B. H. Park, G. J. Tearney, B. E. Bouma, T. C. Chen, and J. F. de Boer, *In vivo* dynamic human retinal blood flow imaging using ultra-high-speed spectral domain optical coherence tomography, Opt. Express **11**, 3490–3497 (2003).

[43] R. A. Leitgeb, L. Schmetterer, C. K. Hitzenberger, A. F. Fercher, F. Berisha, M. Wojtkowski, and T. Bajraszewski, Real-time measurement of in vitro flow by fourier-domain color doppler optical coherence tomography, Opt. Lett. **29**, 171–173 (2004).

[44] R. A. Leitgeb, L. Schmetterer, W. Drexler, A. F. Fercher, R. J. Zawadzki, and T. Bajraszewski, Real-time assessment of retinal blood flow with ultrafast acquisition by color doppler fourier domain optical coherence tomography, Opt. Express **11**, 3116–3121 (2003).

[45] B. Baumann, B. Potsaid, M. F. Kraus, J. J. Liu, D. Huang, J. Hornegger, A. E. Cable, J. S. Duker, and J. G. Fujimoto, Total retinal blood flow measurement

with ultrahigh speed swept source/Fourier domain OCT, Biomed. Opt. Express **2**, 1539–1552 (2011).

[46] X. J. Wang, T. E. Milner, and J. S. Nelson, Characterization of fluid flow velocity by optical doppler tomography, Opt. Lett. **20**, 1337–1339 (1995).

[47] Z. Chen, T. E. Milner, D. Dave, and J. S. Nelson, Optical doppler tomographic imaging of fluid flow velocity in highly scattering media, Opt. Lett. **22**, 64–66 (1997).

[48] I. Grulkowski, I. Gorczynska, M. Szkulmowski, D. Szlag, A. Szkulmowska, R. A. Leitgeb, A. Kowalczyk, and M. Wojtkowski, Scanning protocols dedicated to smart velocity ranging in spectral OCT, Opt. Express **17**, 23736–23754 (2009).

[49] L. An, T. T. Shen, and R. K. Wang, Using ultrahigh sensitive optical microangiography to achieve comprehensive depth resolved microvasculature mapping for human retina, J. Biomed. Opt. **16**, 1060131060139 (2011).

[50] Y.-J. Hong, S. Makita, F. Jaillon, M. J. Ju, E. J. Min, B. H. Lee, M. Itoh, M. Miura, and Y. Yasuno, High-penetration swept source doppler optical coherence angiography by fully numerical phase stabilization, Opt. Express **20**, 2740–2760 (2012).

[51] B. Braaf, K. V. Vienola, C. K. Sheehy, Q. Yang, K. A. Vermeer, P. Tiruveedhula, D. W. Arathorn, A. Roorda, and J. F. de Boer, Real-time eye motion correction in phase-resolved OCT angiography with tracking SLO, Biomed. Opt. Express **4**, 51–65 (2013).

[52] S. Makita, F. Jaillon, M. Yamanari, and Y. Yasuno, Dual-beam-scan doppler optical coherence angiography for birefringence-artifact-free vasculature imaging, Opt. Express **20**, 2681–2692 (2012).

[53] S. Zotter, M. Pircher, T. Torzicky, M. Bonesi, E. Götzinger, R. A. Leitgeb, and C. K. Hitzenberger, Visualization of microvasculature by dual-beam phase-resolved doppler optical coherence tomography, Opt. Express **19**, 1217–1227 (2012).

[54] S. Makita, Y. Hong, M. Yamanari, T. Yatagai, and Y. Yasuno, Optical coherence angiography, Opt. Express **14**, 7821–7840 (2006).

[55] E. Götzinger, M. Pircher, M. Sticker, A. F. Fercher, and C. K. Hitzenberger, Measurement and imaging of birefringent properties of the human cornea with phase-resolved, polarization-sensitive optical coherence tomography, J. Biomed. Opt. **9**, 94–102 (2004).

[56] Y. Lim, M. Yamanari, S. Fukuda, Y. Kaji, T. Kiuchi, M. Miura, T. Oshika, and Y. Yasuno, Birefringence measurement of cornea and anterior segment by office-based polarization-sensitive optical coherence tomography, Biomed. Opt. Express **2**, 2392–2402 (2011).

[57] M. Pircher, E. Götzinger, O. Findl, S. Michels, W. Geitzenauer, C. Leydolt, U. Schmidt-Erfurth, and C. K. Hitzenberger, Human macula investigated in vivo with polarization-sensitive optical coherence tomography, Invest. Ophthalmol. Vis. Sci. **47**, 5487–5494 (2006).

[58] M. Miura, M. Yamanari, T. Iwasaki, A. E. Elsner, S. Makita, T. Yatagai, and Y. Yasuno, Imaging polarimetry in age-related macular degeneration, Invest. Ophthalmol. Vis. Sci. **49**, 2661–2667 (2008).

[59] M. Pircher, C. K. Hitzenberger, and U. Schmidt-Erfurth, Polarization sensitive optical coherence tomography in the human eye, Prog. Retin. Eye Res. **30**, 431–451 (2011).

[60] Y. Yasuno, M. Yamanari, K. Kawana, T. Oshika, and M. Miura, Investigation of post-glaucoma-surgery structures by three-dimensional and polarization sensitive anterior eye segment optical coherence tomography, Opt. Express **17**, 3980–3996 (2009).

[61] B. Cense, T. C. Chen, B. H. Park, M. C. Pierce, and J. F. de Boer, Invivo depth-resolved birefringence measurements of the human retinal nerve fiber layer by polarization-sensitive optical coherence tomography, Opt. Lett. **27**, 1610–1612 (2002).

[62] B. Cense, T. C. Chen, B. H. Park, M. C. Pierce, and J. F. de Boer, Thickness and birefringence of healthy retinal nerve fiber layer tissue measured with polarization-sensitive optical coherence tomography, Invest. Ophthalmol. Vis. Sci. **45**, 2606–2612 (2004).

[63] B. Cense, M. Mujat, T. C. Chen, B. H. Park, and J. F. de Boer, Polarization-sensitive spectral-domain optical coherence tomography using a single line scan camera, Opt. Express **15**, 2421–2431 (2007).

[64] M. Mujat, B. H. Park, B. Cense, T. C. Chen, and J. F. de Boer, Autocalibration of spectral-domain optical coherence tomography spectrometers for in vivo

quantitative retinal nerve fiber layer birefringence determination, J. Biomed. Opt. **12**, 041205 (2007).

[65] M. Yamanari, M. Miura, S. Makita, T. Yatagai, and Y. Yasuno, Phase retardation measurement of retinal nerve fiber layer by polarization-sensitive spectral-domain optical coherence tomography and scanning laser polarimetry, J. Biomed. Opt. **13**, 014013 (2008).

[66] E. Götzinger, M. Pircher, B. Baumann, C. Hirn, C. Vass, and C. K. Hitzenberger, Analysis of the origin of atypical scanning laser polarimetry patterns by polarization-sensitive optical coherence tomography, Invest. Ophthalmol. Vis. Sci. **49**, 5366–5372 (2008).

[67] E. Götzinger, M. Pircher, B. Baumann, C. Hirn, C. Vass, and C. K. Hitzenberger, Retinal nerve fiber layer birefringence evaluated with polarization sensitive spectral domain OCT and scanning laser polarimetry: A comparison, J. Biophoton. **1**, 129–139 (2008).

[68] B. Cense, M. Mujat, T. C. Chen, B. H. Park, and J. F. de Boer, Polarization-sensitive spectral-domain optical coherence tomography using a single line scan camera, Opt. Express **15**, 2421–2431 (2007).

[69] L. Duan, M. Yamanari, and Y. Yasuno, Automated phase retardation oriented segmentation of chorio-scleral interface by polarization sensitive optical coherence tomography, Opt. Express **20**, 3353–3366 (2012).

[70] T. Torzicky, M. Pircher, S. Zotter, M. Bonesi, E. Götzinger, and C. K. Hitzenberger, Automated measurement of choroidal thickness in the human eye by

polarization sensitive optical coherence tomography, Opt. Express **20**, 7564 (2012).

[71] M. Pircher, E. Götzinger, R. A. Leitgeb, H. Sattmann, O. Findl, and C. Hitzenberger, Imaging of polarization properties of human retina in vivo with phase resolved transversal PS-OCT, Opt. Express **12**, 5940–5951 (2004).

[72] E. Götzinger, M. Pircher, and C. K. Hitzenberger, High speed spectral domain polarization sensitive optical coherence tomography of the human retina, Opt. Express **13**, 10217–10229 (2005).

[73] E. Götzinger, M. Pircher, B. Baumann, C. Ahlers, W. Geitzenauer, U. Schmidt-Erfurth, and C. K. Hitzenberger, Three-dimensional polarization sensitive OCT imaging and interactive display of the human retina, Opt. Express **17**, 4151–4165 (2009).

[74] E. Götzinger, M. Pircher, W. Geitzenauer, C. Ahlers, B. Baumann, S. Michels, U. Schmidt-Erfurth, and C. K. Hitzenberger, Retinal pigment epithelium segmentation by polarization sensitive optical coherencetomography, Opt. Express **16**, 16410–16422 (2008).

[75] M. R. Hee, D. Huang, E. A. Swanson, and J. G. Fujimoto, Polarization-sensitive low-coherence reflectometer for birefringence characterization and ranging, J. Opt. Soc. Am. B **9**, 903–908 (1992).

[76] J. F. de Boer, T. E. Milner, and J. S. Nelson, Determination of the depth-resolved Stokes parameters of light backscattered from turbid media by use of polarization-sensitive optical coherence tomography, Opt. Lett.**24**, 300–302 (1999).

[77] C. E. Saxer, J. F. de Boer, B. H. Park, Y. Zhao, Z. Chen, and J. S. Nelson, High-speed fiber based polarization-sensitive optical coherence tomography of in vivo human skin, Opt. Lett. **25**, 1355–1357 (2000).

[78] B. Park, M. C. Pierce, B. Cense, S. H. Yun, M. Mujat, G. Tearney, B. Bouma, and J. F. de Boer, Real-time fiber-based multi-functional spectral-domain optical coherence tomography at 1.3 m, Opt. Express **13**, 3931–3944 (2005).

[79] G. Yao and L. V. Wang, Two-dimensional depth-resolved Mueller matrix characterization of biological tissue by optical coherence tomography, Opt. Lett. **24**, 537–539 (1999).

[80] Y. Yasuno, S. Makita, Y. Sutoh, M. Itoh, and T. Yatagai, Birefringence imaging of human skin by polarization-sensitive spectral interferometric optical coherence tomography, Opt. Lett. **27**, 1803–1805 (2002).

[81] S. Jiao, G. Yao, and L. V. Wang, Depth-Resolved Two-Dimensional Stokes Vectors of Backscattered Light and Mueller Matrices of Biological Tissue Measured With Optical Coherence Tomography, Appl. Opt. **39**, 6318–6324 (2000).

[82] M. Yamanari, S. Makita, V. D. Madjarova, T. Yatagai, and Y. Yasuno, Fiber-based polarization-sensitive fourier domain optical coherence tomography using b-scan-oriented polarization modulation method, Opt. Express **14**, 6502–6515 (2006).

[83] M. Yamanari, S. Makita, and Y. Yasuno, Polarization-sensitive swept-source optical coherence tomography with continuous source polarization modulation, Opt. Express **16**, 5892–5906 (2008).

[84] S. Jiao, W. Yu, G. Stoica, and L. Wang, Optical-fiber-based mueller optical coherence tomography, Opt. Lett. **28**, 1206–1208 (2003).

[85] B. H. Park, M. C. Pierce, B. Cense, and J. F. de Boer, Jones matrix analysis for a polarization-sensitive optical coherence tomography system using fiber-optic components, Opt. Lett. **29**, 2512–2514 (2004).

[86] S. Makita, M. Yamanari, and Y. Yasuno, Generalized jones matrix optical coherence tomography: performance and local birefringence imaging, Opt. Express **18**, 854–876 (2010).

[87] K. H. Kim, B. H. Park, Y. Tu, T. Hasan, B. Lee, J. Li, and J. F. de Boer,Polarization-sensitive optical frequency domain imaging based on unpolarized light, Opt. Express **19**, 552–561 (20ll).

[88] Y. Lim, Y.-J. Hong, L. Duan, M. Yamanari, and Y. Yasuno, Passive component based multifunctional jones matrix swept source optical coherence tomography for doppler and polarization imaging, Opt. Lett. **37**, 1958–1960 (2012).

[89] B. Baumann, W. Choi, B. Potsaid, D. Huang, J. S. Duker, and J. G. Fujimoto, Swept source / fourier domain polarization sensitive optical coherence tomography with a passive polarization delay unit, Opt. Express**20**, 10229–10241 (2012).

[90] M. J. Ju, Y.-J. Hong, S. Makita, Y. Lim, K. Kurokawa, L. Duan, M. Miura, S. Tang, and Y. Yasuno, Advanced multi-contrast Jones matrix optical coherence tomography for Doppler and polarization sensitive imaging, Opt. Express **21**, 19412-19436 (2013).

[91] Y. Yasuno, V. D. Madjarova, S. Makita, M. Akiba, A. Morosawa, C. Chong, T. Sakai, K.-P. Chan, M. Itoh, and T. Yatagai, Three-dimensional and high-speed swept-source optical coherence tomography for in vivo investigation of human anterior eye segments, Opt. Express **13**, 10652–10664 (2005).

[92] Y. Yasuno, Y. Hong, S. Makita, M. Yamanari, M. Akiba, M. Miura, and T. Yatagai, In vivo high-contrast imaging of deep posterior eye by 1-μm swept source optical coherence tomography and scattering optical coherence angiography, Opt. Express **15**, 6121–6139 (2007).

[93] B. Vakoc, S. Yun, J. de Boer, G. Tearney, and B. Bouma, Phase-resolved optical frequency domain imaging, Opt. Express **13**, 5483–5493 (2005).

[94] B. Braaf, K. A. Vermeer, V. A. D. Sicam, E. van Zeeburg, J. C. van Meurs, and J. F. de Boer, Phase-stabilized optical frequency domain imaging at 1-μm for the measurement of blood flow in the human choroid, Opt. Express **19**, 20886–20903 (2011).

[95] M. Yamanari, S. Makita, Y. Lim, and Y. Yasuno, Full-range polarization-sensitive swept-source optical coherence tomography by simultaneous transversal and spectral modulation, Opt. Express **18**, 13964–13980 (2010).

[96] B. J. Vakoc, R. M. Lanning, J. A. Tyrrell, T. P. Padera, L. A. Bartlett, T. Stylianopoulos, L. L. Munn, G. J. Tearney, D. Fukumura, R. K. Jain, and B. E. Bouma, Three-dimensional microscopy of the tumor microenvironment in vivo using optical frequency domain imaging, Nat. Med **15**, 1219–1223 (2009).

[97] K. Kurokawa, K. Sasaki, S. Makita, Y.-J. Hong, and Y. Yasuno, Three-dimensional retinal and choroidal capillary imaging by power doppler opti-

cal coherence angiography with adaptive optics, Opt. Express**20**, 22796–22812 (2012).

[98] J. P. Sarks, S. H. Sarks, and M. C. Killingsworth, Evolution of geographic atrophy of the retinal pigment epithelium, Eye **2**, 552–577 (1988).

[99] R. Klein, M. D. Davis, Y. L. Magli, P. Segal, B. E. Klein, and L. Hubbard, The wisconsin age-related maculopathy grading system, Ophthalmology **98**, 1128–1134 (1991).

[100] J. J. Weiter, F. C. Delori, G. L. Wing, and K. A. Fitch, Retinal pigment epithelial lipofuscin and melanin and choroidal melanin in human eye, Invest. Ophthalmol. Vis. Sci. **27**, 145–152 (1986).

[101] S. Moon, S.-W. Lee, and Z. Chen, Reference spectrum extraction and fixed-pattern noise removal in optical coherence tomography, Opt. Express **18**, 24395–24404 (2010).

[102] J. V. Greiner, T. Glonek, D. R. Korb, A. C. Whalen, E. Hebert, S. L. Hearn, J. E. Esway, and C. D. Leahy, Volume of the human and rabbit meibomian gland system, Adv. Exp. Med. Biol. **438**, 339–343 (1998).

[103] N. Nicolaides, J. K. Kaitaranta, T. N. Rawdah, J. I. Macy, F. M. Boswell, and R. E. Smith, Meibomian gland studies: comparison of steer and human lipids, Invest. Ophthalmol. Vis. Sci. **20**, 522–536 (1981).

[104] A. J. Bron, J. M. Tiffany, S. M. Gouveia, N. Yokoi, L. W. Voon, Functional aspects of the tear film lipid layer, Exp. Eye Res. **78**, 347–360 (2004).

[105] W. Ngo, S. Srinivasan, and L. Jones, Historical overview of imaging the meibomian glands, J. Optom. **6**, 1–8 (2013).

[106] K. Bizheva, P. Lee, L. Sorbara, N. Hutchings, and T. Simpson, In vivo volumetric imaging of the human upper eyelid with ultrahigh-resolution optical coherence tomography, J. Biomed. Opt. **15**, 040508–040508–3 (2010).

[107] M. J. Ju, J. G. Shin, S. Hoshi, Y. Yasuno, B. H. Lee, S. Tang, and T. J. Eom, Three-dimensional volumetric human meibomian gland investigation using polarization-sensitive optical coherence tomography, J. Biomed. Opt. **19**, 030503 (2014).

[108] A. S. Henriquez, and D. R. Korb, Meibomian glands and contact lens wear, Br. J. Ophthalmol. **65**, 108–111 (1981).

[109] V. J. Gutgesell, G. A. Stern, and C. I. Hood, Histopathology of meibomian gland dysfunction, Am. J. Ophthalmol. **94**, 383–387 (1982).

[110] H. Obata, Anatomy and histopathology of human meibomian gland, Cornea **21**, S70–74 (2002).

[111] R. Arita, K. Itoh, K. Inoue, and S. Amano, Noncontact infrared meibography to document age-related changes of the meibomian glands in a normal population, Ophthalmology **115**, 911–915 (2008).

[112] J. Shimazaki, E. Goto, M. Ono, S. Shimmura, and K. Tsubota, Meibomian gland dysfunction in patients with Sjögren syndrome, Ophthalmology **105**, 1485–1488 (1998).

[113] E. Goto, Y. Monden, Y. Takano, A. Mori, S. Shimmura, J. Shimazaki, and K. Tsubota, Treatment of non-inflamed obstructive meibomian gland dysfunction by an infrared warm compression device, Br. J. Ophthalmol. **86**, 1403–1407 (2002).

[114] S. Den, K. Shimizu, T. Ikeda, K. Tsubota, S. Shimmura, and J. Shimazaki, Association between meibomian gland changes and aging, sex, or tear function, Cornea **25**, 651–655 (2006).

[115] W. D. Mathers, W. J. Shields, M. S. Sachdev, W. M. Petroll, and J. V. Jester, Meibomian gland morphology and tear osmolarity: changes with Accutane therapy, Cornea **10**, 286–290 (1991).

[116] J. P. McCulley, W. E. Shine, J. Aronowicz, D. Oral, and J. Vargas, Presumed hyposecretory/hyperevaporative KCS: tear characteristics, Trans. Am. Ophthalmol. Soc. **101**, 141–154 (2003).

[117] F. G. Schlanitz, B. Baumann, T. Spalek, C. Schütze, C. Ahlers, M. Pircher, E. Götzinger, C. K. Hitzenberger, and U. Schmidt-Erfurth, Performance of automated drusen detection by polarization-sensitive optical coherence tomography, Invest. Ophthalmol. Vis. Sci. **52**, 4571–4579 (2011).

[118] S. Fukuda, M. Yamanari, Y. Lim, S. Hoshi,S. Beheregaray, T. Oshika and Y. Yasuno, Keratoconus diagnosis using anterior segment polarization-sensitive optical coherence tomography, Invest. Ophthalmol. Vis. Sci. **54**, 1384–1391 (2013).

[119] G. Wollensak, E. Spoerl and T. Seiler, Riboflavin/ultraviolet-a-induced collagen crosslinking for the treatment of keratoconus, Am. J. Ophthalmol. **135**, 620–627 (2003).

[120] M. Kohlhaas, E. Spoerl,T. Schilde, G. Unger, C. Wittig, L. E. Pillunat, Biomechanical evidence of the distribution of cross-links in corneas treated with riboflavin and ultraviolet A light, J. Cataract Refract. Surg. **32**, 279–283 (2006).

[121] A. S. McCall, S. Kraft, H. F. Edelhauser, G. W. Kidder, R. R. Lundquist, H. E. Bradshaw, Z. Dedeic, M. J. C. Dionne, E. M. Clement and G. W. Conrad, Mechanisms of corneal tissue cross-linking in response to treatment with topical riboflavin and long-wavelength ultraviolet radiation (UVA), Invest. Ophthalmol. Vis. Sci. **51**, 129–138 (2010).

[122] E. Spoerl, M. Huhle and T. Seiler, Induction of cross-links in corneal tissue, Exp. Eye Res. **66**, 97–103 (1998).

[123] G. Wollensak, E. Spoerl and T. Seiler, Stress-strain measurements of human and porcine corneas after riboflavin-ultraviolet-A-induced cross-linking, J. Cataract Refract. Surg. **29**, 1780–1785 (2003).

[124] G. Wollensak, Crosslinking treatment of progressive keratoconus: new hope, Curr. Opin. Ophthalmol. **17**, 356–360 (2006).

[125] C. Mazzotta, A. Balestrazzi, C. Traversi, S. Baiocchi, T. Caporossi, C. Tommasi and A. Caporossi, Treatment of progressive keratoconus by riboflavin-UVA-induced cross-linking of corneal collagen: ultrastructural analysis by Heidelberg Retinal Tomograph II in vivo confocal microscopy in humans, Cornea **26**, 390–397 (2007).

[126] J. C. Erie, Corneal wound healing after photorefractive keratectomy: a 3-year confocal microscopy study, Trans. Am. Ophthalmol. Soc. **101**, 293–333 (2003).

[127] I. Perez-Gomez and N. Efron, Change to corneal morphology after refractive surgery (myopic laser in situ keratomileusis) as viewed with a confocal microscope, Optom. Vis. Sci. **80**, 690–697 (2003).

[128] R. L. Niederer, D. Perumal, T. Sherwin and C. N. J. McGhee, Age-related differences in the normal human cornea: a laser scanning in vivo confocal microscopy study, Br. J. Ophthalmol. **91**, 1165–1169 (2007).

[129] O. Stachs, A. Zhivov, R. Kraak, M. Hovakimyan, A. Wree and R. Guthoff, Structural-functional correlations of corneal innervation after LASIK and penetrating keratoplasty, J. Refract. Surg. **26**, 159–167 (2010).

[130] K. M. Bottós, J. L. Dreyfuss, C. V. S. Regatieri, A. A. S. Lima-filho, P. Schor, H. B. Nader and W. Chamon, Immunofluorescence Confocal Microscopy of Porcine Corneas Following Collagen Cross-linking Treatment With Riboflavin and Ultraviolet A, J. Refract. Surg. **24**, 715–719 (2008).

[131] J. M. Bueno, E. J. Gualda, A. Giakoumaki, P. Pérez-Merino, S. Marcos and P. Artal, Multiphoton microscopy of ex vivo corneas after collagen cross-linking, Invest. Ophthalmol. Vis. Sci. **52**, 5325–5331 (2011).

[132] D. W. Piston, B. R. Masters and W. W. Webb, Three-dimensionally resolved NAD(P)H cellular metabolic redox imaging of the in situ cornea with two-photon excitation laser scanning microscopy, J. Microsc. **178**, 20–27 (1995).

[133] A. T. Yeh, N. Nassif, A. Zoumi and B. J. Tromberg, Selective corneal imaging using combined second-harmonic generation and two-photon excited fluorescence, Opt. Lett. **27**, 2082–2084 (2002).

[134] N. Morishige and N. Teruo Second Harmonic Generation for Visualizing 3-Dimensional Structure of Corneal Collagen Lamellae, Cornea **28**, S46–S53 (2009).

[135] F. Aptel, N. Olivier, A. Deniset-Besseau, J.-M. Legeais, K. Plamann, M.-C. Schanne-Klein and E. Beaurepaire, Multimodal Nonlinear Imaging of the Human Cornea, Invest. Ophthalmol. Vis. Sci. **51**, 2459–2465 (2010).

[136] M. Doors, N. G. Tahzib, F. A. Eggink, T. T. Berendschot, C. A. Webers and R. M. Nuijts, Use of anterior segment optical coherence tomography to study corneal changes after collagen cross-linking, Am. J. Ophthalmol. **148**, 844–851 (2009).

[137] M. Pircher, E. Göetzinger, R. A. Leitgeb and C. K. Hitzenberger, Transversal phase resolved polarization sensitive optical coherence tomography, Phys. Med. Biol. **49**, 1257–1263 (2004).

[138] M. Pircher, C. K. Hitzenberger and U. Schmidt-Erfurth, Polarization sensitive optical coherence tomography in the human eye, Prog. Retin. Eye Res. **30**, 431–451 (2011).

[139] E. Götzinger, M. Pircher, I. Dejaco-Ruhswurm, S. Kaminski, C. Skorpik and C. K. Hitzenberger, Imaging of birefringent properties of keratoconus corneas by polarization-sensitive optical coherence tomography, Invest. Ophthalmol. Vis. Sci. **48**, 3551–3558 (2007).

[140] D. Alonso-Caneiro, M. Yamanari, S. Fukuda, S. Hoshi, S. Nagase, T. Oshika, Y. Yasuno and M. Collins, Non-invasive assessment of corneal crosslinking changes using polarization sensitive optical coherence tomography, in Ophthalmic Technologies XXIII, Proc. SPIE **8567**, 85670F–85670F–7 (2013).

[141] F. LaRocca, S. J. Chiu, R. P. McNabb, A. N. Kuo, J. A. Izatt and S. Farsiu, Robust automatic segmentation of corneal layer boundaries in SDOCT images

using graph theory and dynamic programming, Biomed. Opt. Express **2**, 1524–1538 (2011).

[142] M. J. Ju, and S. Tang, Usage of polarization-sensitive optical coherence tomography for investigation of collagen cross-linking, J. Biomed. Opt. **20**, 046001 (2015).

[143] T. Lai and S. Tang, Cornea characterization using a combined multiphoton microscopy and optical coherence tomography system, Biomed. Opt. Express **5**, 1494–1511 (2014).

[144] F. Raiskup-Wolf, A. Hoyer, E. Spoerl and L. E. Pillunat, Collagen crosslinking with riboflavin and ultraviolet-A light in keratoconus: long-term results, J. Cataract Refract. Surg. **34**, 796–801 (2008).

[145] A. Caporossi, C. Mazzotta, S. Baiocchi and T. Caporossi, Long-term results of riboflavin ultraviolet a corneal collagen cross-linking for keratoconus in Italy: the Siena eye cross study, Am. J. Ophthalmol. **149**, 585–593 (2010).

[146] C. Wittig-Silva, M. Whiting, E. Lamoureux, R. G. Lindsay, L. J. Sullivan and G. R. Snibson, A randomized controlled trial of corneal collagen cross-linking in progressive keratoconus: preliminary results, J. Refract. Surg. **24**, S720–725 (2008).

[147] A. Caporossi, C. Mazzotta, S. Baiocchi, T. Caporossi and R. Denaro, Age-Related Long-Term Functional Results after Riboflavin UV A Corneal Cross-Linking, J. Ophthalmol. **2011**, 608041 (2011).

[148] A. Caporossi, C. Mazzotta, S. Baiocchi, T. Caporossi, R. Denaro and A. Balestrazzi, Riboflavin-UVA-induced corneal collagen cross-linking in pediatric patients, Cornea **31**, 227–231 (2012).

[149] G. S. Brindley, The Bunsen-Roscoe law for the human eye at very short durations, J. Physiol. (Lond.) **118**, 135–139 (1952).

[150] J. Wernli, S. Schumacher, E. Spoerl and M. Mrochen, The efficacy of corneal cross-linking shows a sudden decrease with very high intensity UV light and short treatment time, Invest. Ophthalmol. Vis. Sci. **54**, 1176–1180 (2013).

[151] H. U. Celik, N. Alagöz, Y. Yildirim, A. Agca, J. Marshall, A. Demirok and O. F. Yilmaz, Accelerated corneal crosslinking concurrent with laser in situ keratomileusis, J. Cataract Refract. Surg. **38**, 1424–1431 (2012).

[152] D. A. Hoeltzel, P. Altman, K. Buzard, and K. Choe, Strip extensiometry for comparison of the mechanical response of bovine, rabbit, and human corneas, J. Biomech. Eng. **114**, 202–215 (1992).

[153] T. Seiler and F. Hafezi, Corneal cross-linking-induced stromal demarcation line, Cornea **25**, 1057–1059 (2006).

[154] G. Wollensak, E. Spoerl, M. Wilsch and T. Seiler, Keratocyte apoptosis after corneal collagen cross-linking using riboflavin/UVA treatment, Cornea **23**, 43–49 (2004).

[155] J. C. Yam, C. W. Chan and A. C. Cheng, Corneal Collagen Cross-linking Demarcation Line Depth Assessed by Visante OCT After CXL for Keratoconus and Corneal Ectasia, J. Refract. Surg. **28**, 475–481 (2012).

[156] G. Wollensak, E. Iomdina, D.-D. Dittert and H. Herbst, Wound healing in the rabbit cornea after corneal collagen cross-linking with riboflavin and UVA, Cornea **26**, 600–605 (2007).

[157] J. S. Dhaliwal, and S. C. Kaufman, Corneal Collagen Cross-Linking: A Confocal, Electron, and Light Microscopy Study of Eye Bank Corneas, Cornea **28**, 62–67 (2009).

[158] M. D. Twa, J. Li, S. Vantipalli, M. Singh, S. Aglyamov, S. Emelianov, and K. V. Larin, Spatial characterization of corneal biomechanical properties with optical coherence elastography after UV cross-linking, Biomed. Opt. Express **5**, 1419–1427 (2014).

[159] K. Omodaka, T. Horii, S. Takahashi, T. Kikawa, A. Matsumoto, Y. Shiga, K. Maruyama, T. Yuasa, M. Akiba, T. Nakazawa, 3D Evaluation of the Lamina Cribrosa with Swept-Source Optical Coherence Tomography in Normal Tension Glaucoma, PLoS ONE **10**, e0122347 (2015).

[160] H. A. Quigley, Number of people with glaucoma worldwide, Br. J. Ophthalmol **80**, 389–393 (1996).

[161] W. Choi, B. Potsaid, V. Jayaraman, B. Baumann1, I. Grulkowski1, J. J. Liu, C. D. Lu, A. E. Cable, D. Huang, J. S. Duker, and J. G. Fujimoto, Phase-sensitive swept-source optical coherence tomography imaging of the human retina with a vertical cavity surface-emitting laser light source, Opt. Lett. **38**, 338–340 (2013).

[162] A. H. Dhalla, K. Shia, and J. A. Izatt, Efficient sweep buffering in swept source optical coherence tomography using a fast optical switch, Biomed. Opt. Express **3**, 3054–3066 (2012).